

## **ABSTRACT**

BROWN, JUDITH ALICE. The Modeling of Coupled Electromagnetic-Thermo-Mechanical Laser Interactions and Microstructural Behavior of Energetic Aggregates. (Under the direction of Dr. Mohammed Zikry).

The coupled electromagnetic-thermo-mechanical response of RDX (cyclotrimethylene trinitramine)-polymer energetic aggregates under laser irradiation and high strain rate loads has been investigated to identify laser-induced hot spot formation and failure mechanisms at different physical scales. A computational approach was developed to investigate the coupled phenomena of high frequency electromagnetic (EM) wave propagation, laser heat absorption, thermal conduction, and inelastic dynamic thermo-mechanical deformation in heterogeneous energetic materials. The approach couples Maxwell's equations with a dislocation density-based crystal plasticity formulation with a nonlinear finite-element approach to predict and understand thermo-mechanical response due to the interrelated effects of dielectric heating, adiabatic heating, thermal decomposition, and heat conduction. The effects of heterogeneous microstructural characteristics, such as void distribution and spacing, grain morphologies and orientations, crystal-binder interactions, and dislocation densities were analyzed to determine their influence on hot spot formation and EM and mechanical energy localization.

The effects of beam intensity, incident wavelength, material electromagnetic absorption coefficient, and the heterogeneous microstructure on spatial and temporal behavior and mechanisms of laser-induced hot spot formation were characterized and related to the thermo-mechanical response. Different mechanisms for hot spot initiation under dynamic laser and pressure loads were identified, which are a function of shear strain localization and laser heat absorption. The predictions indicate that hot spot formation was

Report Documentation Page		Form Approved OMB No. 0704-0188
Public reporting burden for the collection of information is estimated to average 1 hour per response, including the time for reviewing instructions, searching existing data sources, gathering and maintaining the data needed, and completing and reviewing the collection of information. Send comments regarding this burden estimate or any other aspect of this collection of information, including suggestions for reducing this burden, to Washington Headquarters Services, Directorate for Information Operations and Reports, 1215 Jefferson Davis Highway, Suite 1204, Arlington VA 22202-4302. Respondents should be aware that notwithstanding any other provision of law, no person shall be subject to a penalty for failing to comply with a collection of information if it does not display a currently valid OMB control number.		
1. REPORT DATE <b>14 JUL 2014</b>	2. REPORT TYPE <b>Final</b>	3. DATES COVERED <b>1 Aug 2010 - 31 Dec 2016</b>
4. TITLE AND SUBTITLE <b>The Modeling of Coupled Electromagnetic-Thermo-Mechanical Laser Interactions and Microstructural Behavior of Energetic Aggregates / PhD Dissertation</b>		5a. CONTRACT NUMBER <b>N/A</b>
		5b. GRANT NUMBER <b>N00014-10-1-0958</b>
		5c. PROGRAM ELEMENT NUMBER <b>N/A</b>
6. AUTHOR(S) <b>Judith A. Brown Mechanical Engineering North Carolina State University</b>		5d. PROJECT NUMBER <b>N/A</b>
		5e. TASK NUMBER <b>N/A</b>
		5f. WORK UNIT NUMBER <b>N/A</b>
7. PERFORMING ORGANIZATION NAME(S) AND ADDRESS(ES) <b>North Carolina State University Electrical &amp; Computer Engineering 890 Oval Dr., 3114 Engineering Building II Raleigh, NC 27695</b>		8. PERFORMING ORGANIZATION REPORT NUMBER <b>57</b>
9. SPONSORING/MONITORING AGENCY NAME(S) AND ADDRESS(ES) <b>Office of Naval Research (ONR) 875 North Randolph Street - Suite 1425 Code 03R Arlington, VA 22203-1995</b>		10. SPONSOR/MONITOR'S ACRONYM(S) <b>ONR</b>
		11. SPONSOR/MONITOR'S REPORT NUMBER(S) <b>N/A</b>
12. DISTRIBUTION/AVAILABILITY STATEMENT <b>Approved for public release, distribution unlimited</b>		
13. SUPPLEMENTARY NOTES <b>N/A, The original document contains color images.</b>		

#### 14. ABSTRACT

The coupled electromagnetic-thermo-mechanical response of RDX (cyclotrimethylene trinitramine)-polymer energetic aggregates under laser irradiation and high strain rate loads has been investigated to identify laser-induced hot spot formation and failure mechanisms at different physical scales. A computational approach was developed to investigate the coupled phenomena of high frequency electromagnetic (EM) wave propagation, laser heat absorption, thermal conduction, and inelastic dynamic thermomechanical deformation in heterogeneous energetic materials. The approach couples Maxwell's equations with a dislocation density-based crystal plasticity formulation with a nonlinear finite-element approach to predict and understand thermo-mechanical response due to the interrelated effects of dielectric heating, adiabatic heating, thermal decomposition, and heat conduction. The effects of heterogeneous microstructural characteristics, such as void distribution and spacing, grain morphologies and orientations, crystal-binder interactions, and dislocation densities were analyzed to determine their influence on hot spot formation and EM and mechanical energy localization. The effects of beam intensity, incident wavelength, material electromagnetic absorption coefficient, and the heterogeneous microstructure on spatial and temporal behavior and mechanisms of laser-induced hot spot formation were characterized and related to the thermo-mechanical response. Different mechanisms for hot spot initiation under dynamic laser and pressure loads were identified, which are a function of shear strain localization and laser heat absorption. The predictions indicate that hot spot formation was accelerated by higher absorption coefficients and by localized plastic deformations that occurred in areas of significant laser heating. RDX crystalline interfaces and orientations, polymer binder, inelastic strains, dislocation-density evolution, and voids significantly affected the coupled EM-thermo-mechanical response. EM and thermo-mechanical mismatches at interfaces between RDX crystals, binder, and voids resulted in localized regions with high electric field and laser heat generation rates, which subsequently led to hot spot formation. The incident laser intensity and shear strain localization were the dominant mechanisms that led to hot spot formation. The coupled electromagnetic-thermo-mechanical response of RDX-estane energetic aggregates under laser irradiation and high strain rate loads was also investigated. Temperatures induced by laser heating were above the glass transition temperature of estane, and therefore a finite viscoelastic constitutive relation was used to represent binder behavior. Local behavior mismatches at the crystal-binder interfaces resulted in geometrical scattering of the EM wave, electric field and laser heating localization, high stress gradients, dislocation density and crystalline shear slip accumulation. Viscous sliding in the binder was another energy dissipation mechanism that reduced stresses in aggregates with thicker binder ligaments and larger binder volume fractions. Energetic aggregates with binders that had embedded crystals with a broad range of size distributions were investigated to account for physically representative energetic microstructures. The presence of embedded crystals in the binder ligaments restricted viscous sliding, and resulted in global hardening of the aggregate, which led to large stress gradients, localized plasticity, and dislocation density accumulation. The smaller crystals also increased scattering of the EM wave within the binder ligaments and increased the localization of EM energy and laser heat generation. Geometrically necessary dislocation densities (GNDs) were calculated to characterize how hardening at the binder interfaces can lead to strengthening or defect nucleation. This investigation indicates how the interrelated interactions between EM waves, material microstructure, and mechanical behavior in RDX-polymer aggregates underscores the need for a coupled approach for accurate predictions of high strain rate deformation and laser irradiation of heterogeneous materials. The predictions indicate that the response is governed by laser EM energy and shear strain localization, and that controlling the aggregate microstructure and laser characteristics, such as beam intensity, material absorption coefficient, crystal size distributions, and porosity, will enable the prediction of hot spot formation, the enhancement of laser-based ignition and laser-based detection of energetic materials.

#### 15. SUBJECT TERMS

16. SECURITY CLASSIFICATION OF:			17. LIMITATION OF ABSTRACT <b>SAR</b>	18. NUMBER OF PAGES <b>150</b>	19a. NAME OF RESPONSIBLE PERSON
a. REPORT <b>unclassified</b>	b. ABSTRACT <b>unclassified</b>	c. THIS PAGE <b>unclassified</b>			

accelerated by higher absorption coefficients and by localized plastic deformations that occurred in areas of significant laser heating. RDX crystalline interfaces and orientations, polymer binder, inelastic strains, dislocation-density evolution, and voids significantly affected the coupled EM-thermo-mechanical response. EM and thermo-mechanical mismatches at interfaces between RDX crystals, binder, and voids resulted in localized regions with high electric field and laser heat generation rates, which subsequently led to hot spot formation. The incident laser intensity and shear strain localization were the dominant mechanisms that led to hot spot formation.

The coupled electromagnetic-thermo-mechanical response of RDX-estane energetic aggregates under laser irradiation and high strain rate loads was also investigated. Temperatures induced by laser heating were above the glass transition temperature of estane, and therefore a finite viscoelastic constitutive relation was used to represent binder behavior. Local behavior mismatches at the crystal-binder interfaces resulted in geometrical scattering of the EM wave, electric field and laser heating localization, high stress gradients, dislocation density and crystalline shear slip accumulation. Viscous sliding in the binder was another energy dissipation mechanism that reduced stresses in aggregates with thicker binder ligaments and larger binder volume fractions.

Energetic aggregates with binders that had embedded crystals with a broad range of size distributions were investigated to account for physically representative energetic microstructures. The presence of embedded crystals in the binder ligaments restricted viscous sliding, and resulted in global hardening of the aggregate, which led to large stress gradients, localized plasticity, and dislocation density accumulation. The smaller crystals also increased scattering of the EM wave within the binder ligaments and increased the

localization of EM energy and laser heat generation. Geometrically necessary dislocation densities (GNDs) were calculated to characterize how hardening at the binder interfaces can lead to strengthening or defect nucleation.

This investigation indicates how the interrelated interactions between EM waves, material microstructure, and mechanical behavior in RDX-polymer aggregates underscores the need for a coupled approach for accurate predictions of high strain rate deformation and laser irradiation of heterogeneous materials. The predictions indicate that the response is governed by laser EM energy and shear strain localization, and that controlling the aggregate microstructure and laser characteristics, such as beam intensity, material absorption coefficient, crystal size distributions, and porosity, will enable the prediction of hot spot formation, the enhancement of laser-based ignition and laser-based detection of energetic materials.

© Copyright 2015 Judith Alice Brown

All Rights Reserved

The Modeling of Coupled Electromagnetic-Thermo-Mechanical Laser Interactions and  
Microstructural Behavior of Energetic Aggregates

by  
Judith Alice Brown

A dissertation submitted to the Graduate Faculty of  
North Carolina State University  
in partial fulfillment of the  
requirements for the degree of  
Doctor of Philosophy

Mechanical Engineering

Raleigh, North Carolina

2015

APPROVED BY:

---

Mohammed Zikry  
Committee Chair

---

Larry Silverberg

---

Ronald Scattergood

---

Michael Steer



## **DEDICATION**

I dedicate this dissertation to my beloved grandparents, Barton Crouse Brown, M.S. Ch.E. and Dorothy Ballard Brown. Thank you for all the years of love, support, and prayers throughout my endeavors in engineering and life. It has meant the world to me and I am so happy to share this accomplishment with you.

## BIOGRAPHY

Judith Alice Brown was born in Sylva, NC on May 22, 1987. She grew up in Franklin, NC and graduated from Franklin High School in June 2004. She attended Asbury University in Wilmore, KY and transferred to North Carolina State University in 2006 to pursue an engineering career. Judith was an undergraduate intern at Kennedy Space Center in 2007 through the NASA Undergraduate Student Research Program and participated in the NSF International Research and Education in Engineering Program at The University of Tokyo in 2008. She graduated summa cum laude with a Bachelor of Science degree in Aerospace Engineering in May 2009.

Judith continued her graduate studies at North Carolina State University, earning her Master of Science degree in Mechanical Engineering in August 2012. While pursuing her graduate degrees, she taught several sections of undergraduate Dynamics and Controls Laboratory, Aerospace Engineering Summer Camps, and maintained an active role in promoting mechanical and aerospace engineering education. Her doctoral research focused on the modeling of laser interaction with energetic materials using a coupled finite element and crystalline plasticity approach under the direction of Dr. Mohammed Zikry. The research relating to this dissertation has generated the following journal publications:

**J.A. Brown**, D.A. LaBarbera, M.A. Zikry, “Laser Interaction Effects of Electromagnetic Absorption and Microstructural Defects on Hot Spot Formation in RDX-PCTFE Energetic Aggregates”, *Modeling and Simulation in Materials Science and Engineering*, 22, (2014), 055013.

**J.A. Brown** and M.A. Zikry, “Coupled Infrared Laser-Thermo-Mechanical Response of RDX-PCTFE Energetic Aggregates,” Submitted.

**J.A. Brown** and M.A. Zikry, “Effect of Microstructure on the Coupled Electromagnetic-Thermo-Mechanical Response of Cyclotrimethylenetrinitramine-Estane Energetic Aggregates to Infrared Laser Radiation,” Submitted.

**J.A. Brown**, Qifeng Wu, and M.A. Zikry, “Heterogeneous Crystal Size Distribution, Crystalline-Crystalline, and Crystalline-Amorphous Interfaces in RDX-Estane Energetic Aggregates”, Submitted.

Upon completion of the Doctor of Philosophy degree in Mechanical Engineering, she will begin work as a postdoctoral researcher in the Computational Solid Mechanics group at Sandia National Laboratories.

## ACKNOWLEDGMENTS

I would like to acknowledge all my family, friends, and colleagues who have supported me throughout my educational endeavors and helped me to achieve this goal. Thanks to my parents and grandparents for believing in me and providing encouragement, support and advice all these years and for being there when I needed it. Thanks to my sister for all of our long phone conversations, goofy adventures, and sharing stories to make me laugh. It has meant so much to share these experiences with all of you.

A special thanks goes to Dr. Mohammed Zikry for his insightful guidance and support throughout my research. I would also like to thank my committee members, Dr. Larry Silverberg, Dr. Ronald Scattergood, and Dr. Michael Steer for their valuable comments and feedback. Additionally, acknowledgement to my co-workers Dr. Siqi Xu, Dr. Letisha McLaughlin-Lam, Dr. Prasenjit Khanikar, Dr. Darrell LaBarbera, Dr. Qifeng Wu, Shoayb Ziaei, Matt Bond, Tamir Hasan, Michael Rosenberg, Ismail Mohamed, Russ Mailen, and Jim Fitch for making the lab a great place to work with great people. Many thanks to Dr. Darrell LaBarbera for his invaluable help with all of my Crystal2D questions and our many productive discussions regarding our joint research. Also thanks to Dr. Gary Howell for all his help with troubleshooting on the HPC and the never-ending upkeep of COMSOL.

Finally I would like to thank the U.S. Office of Naval Research for funding this research project as a Multi-Disciplinary University Research Initiative on Sound and Electromagnetic Interacting Waves (SEMI-Wave) under grant number N00014-10-1-0958.

## TABLE OF CONTENTS

LIST OF TABLES .....	viii
LIST OF FIGURES .....	ix
CHAPTER 1: Introduction.....	1
1.1 Overview .....	1
1.2 General Research Objectives and Approach .....	5
1.3 Dissertation Organization .....	6
CHAPTER 2: Material Constitutive Formulations and Electromagnetic-Thermo-Mechanical Coupling.....	8
2.1 Multiple Slip, Dislocation Density-Based Crystalline Plasticity Formulation .....	8
2.1.1 Crystalline Plasticity Kinematics .....	8
2.1.2 Dislocation Density Evolution .....	10
2.2 Constitutive Formulations for Polymer Binders.....	13
2.2.1 Finite Viscoelastic Formulation .....	13
2.3 Electromagnetic Formulation for Laser Wave Propagation .....	15
2.4 Coupling of Electromagnetic and Thermo-Mechanical Behavior.....	16
CHAPTER 3: Numerical Methods.....	19
3.1 Framework for Coupling EM and Thermo-Mechanical Domains.....	19
3.1.1 Mapping Methods Between EM and Thermo-Mechanical Domains .....	22
3.2 Numerical Methods in Thermo-Mechanical Domain .....	23
3.2.1 Determination of the Total Velocity Gradient .....	23
3.2.2 Determination of the Plastic Velocity Gradient .....	24
3.2.3 Finite Element Representation of Thermal Conduction.....	26
CHAPTER 4: Laser Interaction Effects of EM Absorption and Microstructural Defects on Hot-Spot Formation in RDX-PCTFE Energetic Aggregates.....	28
4.1 Introduction.....	28
4.2 Results .....	28
4.2.1 Low RDX Absorption Coefficient ( $\alpha = 10 \text{ cm}^{-1}$ ) and Random Void Distribution .....	32
4.2.2 Intermediate RDX Absorption ( $\alpha = 100 \text{ cm}^{-1}$ ) and Random Void Distribution .....	37
4.2.3 High RDX Absorption ( $\alpha = 1000 \text{ cm}^{-1}$ ) and Random Void Distribution.....	42
4.2.4 Periodic Void Distributions and Intermediate RDX Absorption ( $\alpha = 100 \text{ cm}^{-1}$ ) .....	45
4.2.5 Comparison of Hot Spot Generation Mechanisms.....	49
4.3 Summary.....	51
CHAPTER 5: Coupled Infrared Laser-Thermo-Mechanical Response of RDX-PCTFE Energetic Aggregates .....	55
5.1 Introduction.....	55
5.2 Results .....	55
5.2.1 Low-intensity ( $I_0 = 1 \times 10^5 \text{ W/cm}^2$ ) laser-induced heat generation in various microstructures.....	59
5.2.2 Low-intensity ( $I_0 = 1 \times 10^5 \text{ W/cm}^2$ ) coupled electromagnetic-thermo-mechanical response .....	62
5.2.3 High-intensity ( $I_0 = 1 \times 10^6 \text{ W/cm}^2$ ) coupled electromagnetic-thermo-mechanical response .....	66
5.2.4 Hot Spot Generation Mechanisms .....	71

5.3 Summary .....	73
<b>CHAPTER 6: The Effect of Microstructure on the Coupled EM-Thermo-Mechanical Response of RDX-Estane Aggregates to Infrared Laser Radiation.....</b>	<b>75</b>
6.1 Introduction.....	75
6.2 Results .....	75
6.2.1 Aggregate with 16 grains and 10% volume fraction binder .....	78
6.2.2 Aggregate with 49 grains and 10% volume fraction binder .....	84
6.2.3 Aggregate with 49 RDX grains and 30% volume fraction binder .....	90
6.2.4 Binder Volume Fraction and Grain Size Effects.....	95
6.3 Summary .....	97
<b>CHAPTER 7: Heterogeneous Crystal Size Distribution, Crystalline-Crystalline, and Crystalline-Amorphous Interfaces in RDX-Estane Energetic Aggregates.....</b>	<b>100</b>
7.1 Introduction.....	100
7.2 Results .....	101
7.2.1 Quasi-Static Response of Aggregate with Small Crystals in Binder .....	104
7.2.2 High Strain Rate Coupled EM-Thermo-Mechanical Response of Aggregate with Small Crystals in the Binder .....	111
7.2.3 High Strain Rate Coupled EM-Thermo-Mechanical Response of Aggregate Without Small Crystals in the Binder .....	117
7.2.4 Comparison of Global Response With and Without Small Crystals .....	122
7.3 Summary .....	123
<b>SUMMARY and RECOMMENDATIONS FOR FUTURE RESEARCH.....</b>	<b>126</b>
<b>REFERENCES.....</b>	<b>129</b>

## LIST OF TABLES

Table 1.1: Crystallographic Parameters and Slip Systems for RDX, HMX, and PETN. ....	2
Table 2.1: Summary of g-Coefficients for Dislocation Density Evolution Equations .....	12
Table 4.1: Material Properties of RDX and PCTFE Binder .....	29
Table 5.1: Mechanical, Thermal, and Electrical Properties of RDX and PCTFE Binder .....	56
Table 6.1: Mechanical, Thermal, and Electrical Properties of RDX Crystals and Estane Binder .....	76
Table 7.1: Material Properties of RDX Crystals and Estane Binder Materials. ....	102

## LIST OF FIGURES

Figure 3.1: Computational algorithm for coupled electromagnetic-thermo-mechanical model. ....	20
Figure 3.2: Mapping method for transfer of laser heat generation rate from EM domain to thermo-mechanical domain. (a) Zoomed-in view of model with EM and thermo-mechanical meshes superimposed, (b) Enlarged view from circled region of (a), (c) Element of thermo-mechanical mesh with average laser heat generation rate calculated from (b) applied as a constant value. ....	22
Figure 4.1: The RDX-polymer aggregate with boundary conditions and loading from (a) Compressive pressure load, and (b) Incident laser intensity. The loading conditions are shown separately for clarity, but were applied to the model simultaneously. ....	30
Figure 4.2: Temperature components for random void distribution and RDX absorption coefficient $\alpha = 10 \text{ cm}^{-1}$ , normalized by the initial temperature of 293 K and shown at $0.632 \text{ } \mu\text{s}$ . (a) Total temperature increase including effects from conduction, laser-heating, decomposition, and plastic work heating, (b) Laser-induced temperature increase, (c) Plastic work induced temperature increase, (d) Temperature increase due to thermal decomposition of RDX. ....	33
Figure 4.3: (a) Normal stress (normalized by static yield stress), (b) Accumulated plastic shear strain, (c) Immobile and (d) Mobile dislocation densities from the most active slip system (010)[001] (normalized by the initial value) for random void distribution and low RDX absorption coefficient $\alpha = 10 \text{ cm}^{-1}$ at a time of $0.632 \text{ } \mu\text{s}$ . ....	35
Figure 4.4: (a) Predicted temperature, 1-D analytical solution for laser-generated temperature (Equation (4.3)), and plastic shear strain along the vertical line taken from (b) for RDX absorption coefficient $\alpha = 10 \text{ cm}^{-1}$ with random void distribution. All temperatures are normalized by the initial temperature of 293 K. ....	36
Figure 4.5: Temperature components for random void distribution and RDX absorption coefficient $\alpha = 100 \text{ cm}^{-1}$ , normalized by the initial temperature of 293 K and shown at a time of $0.416 \text{ } \mu\text{s}$ . (a) Total temperature increase including effects from conduction, laser-heating, decomposition, and plastic work heating, (b) Laser-induced temperature increase, (c) Plastic work induced temperature increase, (d) Temperature increase due to thermal decomposition of RDX. ....	38
Figure 4.6: (a) Normal stress (normalized by static yield stress), (b) Accumulated plastic shear strain, (c) Immobile and (d) Mobile dislocation densities from the most active slip system (010)[001] (normalized by the initial value) for random	



void distribution and RDX absorption coefficient $\alpha = 100 \text{ cm}^{-1}$ at a time of 0.416 $\mu\text{s}$ .....	40
Figure 4.7: (a) Plastic shear strain distribution at time 0.416 $\mu\text{s}$ for low RDX absorption coefficient $\alpha = 10 \text{ cm}^{-1}$ and random voids, (b) Plastic shear strain distribution at time 0.416 $\mu\text{s}$ for intermediate RDX absorption coefficient $\alpha = 100 \text{ cm}^{-1}$ and random voids, (c) Normalized temperature-time history for an element within the circled region, (d) Plastic shear strain-time history for an element within the circled region. The same element is used for both low and intermediate absorption cases. ....	41
Figure 4.8: Temperature components for random void distribution and RDX absorption coefficient $\alpha = 1,000 \text{ cm}^{-1}$ , normalized by the initial temperature of 293 K and shown at a time of 0.096 $\mu\text{s}$ . (a) Total temperature increase including effects from conduction, laser-heating, decomposition, and plastic work heating, (b) Laser-induced temperature increase, (c) Plastic work induced temperature increase, (d) Temperature increase due to thermal decomposition of RDX.....	43
Figure 4.9: (a) Normal stress (normalized by static yield stress), (b) Accumulated plastic shear strain, (c) Immobile and (d) Mobile dislocation densities from the most active slip system (010)[001] (normalized by the initial value) for random void distribution and RDX absorption coefficient $\alpha = 1,000 \text{ cm}^{-1}$ at a time of 0.096 $\mu\text{s}$ .....	45
Figure 4.10: Temperature components for periodic void distribution and RDX absorption coefficient $\alpha = 100 \text{ cm}^{-1}$ , normalized by the initial temperature of 293 K and shown at a time of 0.488 $\mu\text{s}$ . (a) Total temperature increase including effects from conduction, laser-heating, decomposition, and plastic work heating, (b) Laser-induced temperature increase, (c) Plastic work induced temperature increase, (d) Temperature increase due to thermal decomposition of RDX.....	46
Figure 4.11: (a) Normal stress (normalized by static yield stress), (b) Accumulated plastic shear strain, (c) Immobile and (d) Mobile dislocation densities from the most active slip system (010)[001] (normalized by the initial value) for periodic void distribution and RDX absorption coefficient $\alpha = 100 \text{ cm}^{-1}$ at a time of 0.488 $\mu\text{s}$ .....	47
Figure 4.12: Temperature-time history normalized by the initial temperature for locations where a hot spot develops.....	49
Figure 5.1: The RDX-PCTFE aggregate with boundary conditions and loading conditions applied in the thermo-mechanical domain (left) and EM domain (right). Quantities transferred between the domains are also shown. ....	58
Figure 5.2: Electric field magnitude (V/m) obtained from EM finite element solution for various energetic aggregate microstructures before deformation. Arrows indicate the location with maximum electric field in each case. (a) Pure RDX,	

(b) RDX/Binder with no voids, (c) RDX/Binder with 3 % random porosity, (d) RDX/Binder with 3 % periodic porosity.....	59
Figure 5.3: Maximum electric field value (MV/m) for the different energetic microstructures. ....	60
Figure 5.4: Volumetric laser heat generation rate ( $\text{W/m}^3$ ) obtained from EM finite element solution for various energetic aggregate microstructures before deformation. Arrows indicate localized areas with high laser heat generation. (a) Pure RDX, (b) RDX/Binder with no porosity, (c) RDX/Binder with 3 % random porosity, (d) RDX/Binder with 3 % periodic porosity. ....	61
Figure 5.5: Mechanical response of RDX/binder aggregate with random void distribution compressed to 8.4 % nominal strain with incident laser intensity of $I_0 = 1 \times 10^5 \text{ cm}^{-1}$ . (a) Normal stress (normalized by static yield stress), (b) Accumulated plastic shear strain, (c) Immobile and (d) Mobile dislocation densities from the most active slip system normalized by the initial dislocation density.....	63
Figure 5.6: Temperature components normalized by the initial temperature of 293 K for RDX/binder aggregate with random void distribution compressed to 8.4 % nominal strain with incident laser intensity of $I_0 = 1 \times 10^5 \text{ cm}^{-1}$ . (a) Total temperature increase including effects from conduction, laser heating, decomposition, and plastic work heating. Areas with unbounded temperature increase are highlighted by arrows. (b) Temperature increase due to thermal decomposition of RDX, (c) Laser-induced temperature increase, (d) Plastic work induced temperature increase. ....	64
Figure 5.7: Mechanical response of RDX/binder aggregate with random void distribution compressed to 8.4 % nominal strain with incident laser intensity of $I_0 = 1 \times 10^6 \text{ cm}^{-1}$ . (a) Normal stress (normalized by static yield stress), (b) Accumulated plastic shear strain, (c) Immobile and (d) Mobile dislocation densities from the most active slip system normalized by the initial dislocation density.....	67
Figure 5.8: Temperature components normalized by the initial temperature of 293 K for RDX/binder aggregate with random void distribution compressed to 8.4 % nominal strain with incident laser intensity of $I_0 = 1 \times 10^6 \text{ cm}^{-1}$ . (a) Total temperature increase including effects from conduction, laser heating, decomposition, and plastic work heating. Areas with unbounded temperature increase are highlighted by arrows. (b) Temperature increase due to thermal decomposition of RDX, (c) Laser-induced temperature increase, (d) Plastic work induced temperature increase. ....	68
Figure 5.9: Total temperature evolution over time with laser intensity of $I_0 = 1 \times 10^6 \text{ cm}^{-1}$ at times of (a) 1 $\mu\text{s}$ , (b) 3 $\mu\text{s}$ , (c) 5 $\mu\text{s}$ , and (d) 7 $\mu\text{s}$ . All temperatures are normalized by the initial temperature of 293 K.....	70
Figure 5.10: Temperature-time history for locations where the first hot spot developed. All temperatures are normalized by the initial temperature of 293 K. ....	71

- Figure 6.1: The RDX-estane aggregate with boundary conditions and loading conditions applied in the thermo-mechanical domain (left) and electromagnetic domain (right). Quantities transferred between the domains are also shown. .... 77
- Figure 6.2: Electric field magnitude (normalized by the applied electric field  $E_0$ ) and laser heat generation rate for 16-grain 10 % binder aggregate after 10  $\mu$ s. (a) Normalized electric field, (b) Volumetric laser heat generation rate, (c) Normalized electric field magnitude as a function of depth below the top surface at  $x = 0.5$  mm, (d) Volumetric laser heat generation rate as a function of depth below the top surface at  $x = 0.5$  mm. .... 79
- Figure 6.3: Response of 16-grain, 10% binder aggregate after 10  $\mu$ s. (a) Normal stress (normalized by RDX yield stress), (b) Energy dissipated by viscous sliding in binder, (c) Accumulated crystalline plastic shear strain, (d) Immobile dislocation density on the most active slip system (021) [100]. .... 81
- Figure 6.4: Temperature accumulation (normalized by initial temperature) in 16-grain, 10% binder aggregate after 10  $\mu$ s. (a) Total temperature increase, (b) Temperature increase due to laser heating, (c) Temperature increase due to plastic work, (d) Temperature increase due to viscous sliding. .... 83
- Figure 6.5: Electric field magnitude (normalized by the applied electric field  $E_0$ ) and laser heat generation rate for 49-grain, 10 % binder aggregate after 10  $\mu$ s. (a) Normalized electric field, (b) Volumetric laser heat generation rate, (c) Normalized electric field magnitude as a function of depth below the top surface at  $x = 0.5$ mm, (d) Volumetric laser heat generation rate as a function of depth below the top surface at  $x = 0.5$ mm. .... 84
- Figure 6.6: Response of 49-grain, 10% binder aggregate after 10  $\mu$ s. (a) Normal stress (normalized by RDX yield stress), (b) Energy dissipated by viscous sliding in binder, (c) Accumulated crystalline plastic shear strain, (d) Immobile dislocation density on the most active slip system (021) [100]. .... 86
- Figure 6.7: (a) Immobile dislocation density build-up on slip system (021) [100] after 5 $\mu$ s, (b) Zoomed-in view of normal stress distribution in boxed region at 5 $\mu$ s, (c) Normal stress–time history for circled regions, (d) Immobile dislocation density–time history on slip system (021) [100] for circled regions. All quantities are normalized by their initial values. .... 88
- Figure 6.8: Temperature accumulation (normalized by initial temperature) in 16-grain, 10% binder aggregate after 10  $\mu$ s. (a) Total temperature increase, (b) Temperature increase due to laser heating, (c) Temperature increase due to plastic work, (d) Temperature increase due to viscous sliding. .... 89
- Figure 6.9: Electric field magnitude (normalized by the applied electric field  $E_0$ ) and laser heat generation rate for 49-grain, 30 % binder aggregate after 10  $\mu$ s. (a) Normalized electric field, (b) Volumetric laser heat generation rate, (c) Normalized electric field magnitude as a function of depth below the top

surface at $x = 0.5\text{mm}$ , (d) Volumetric laser heat generation rate as a function of depth below the top surface at $x = 0.5\text{mm}$ . ....	91
Figure 6.10: Response of 49-grain, 30% binder aggregate after $10\ \mu\text{s}$ . (a) Normal stress (normalized by RDX yield stress), (b) Energy dissipated by viscous sliding in binder, (c) Accumulated plastic shear strain, (d) Immobile dislocation density on the most active slip system (021) [100]. ....	93
Figure 6.11: Temperature accumulation (normalized by initial temperature) in 49-grain, 30% binder aggregate after $10\ \mu\text{s}$ . (a) Total temperature increase, (b) Temperature increase due to laser heating, (c) Temperature increase due to plastic work, (d) Temperature increase due to viscous sliding. ....	94
Figure 6.12: Comparison of laser-induced temperature increase vs. depth from top surface at $x = 0.5\ \text{mm}$ in various aggregates. The full spatial laser-induced temperature distributions are shown on the right. All temperatures are normalized by the initial temperature and shown after time of $10\ \mu\text{s}$ . ....	95
Figure 6.13: Nominal stress-strain curves for various aggregates. All stresses are normalized by the RDX yield stress. ....	97
Figure 7.1: The RDX-estane aggregate with boundary conditions and loading conditions for (a) Quasi-static loading without laser, (b) Dynamic high strain rate load with laser irradiation. ....	103
Figure 7.2: Stress distribution at 8 % nominal strain for quasi-static compression. (a) Lateral stress, (b) Normal stress, (c) Shear stress, (d) Hydrostatic pressure. ....	104
Figure 7.3: Stress distribution along horizontal line at $y=0.6\text{mm}$ for (a) Aggregate with small crystals embedded in the binder, (b) Aggregate without any small crystals. ....	106
Figure 7.4: Inelastic response at 8% nominal strain for quasi-static compression. (a) Accumulated crystalline plastic shear strain, (b) Energy dissipated by viscous sliding in binder, (c) Gradient of accumulated plastic shear strain, $\partial\gamma/\partial x$ , along the dashed line in (4a). Dashed lines indicate the location of the large grain edges. ....	107
Figure 7.5: Dislocation density activity on the most active slip system (010) [001] normalized by the initial immobile dislocation density of $1 \times 10^{12}\ \text{m}^{-2}$ . (a) SSD Immobile dislocation density, (b) SSD Mobile dislocation density, (c) Edge GND, (d) Screw GND. ....	109
Figure 7.6: (a) Spatial location of horizontal lineplots for (b-d) across binder ligament at $y = 0.6\text{mm}$ , (b) GND accumulation as a function of $x$ -coordinate, (c) Normal stress as a function of $x$ -coordinate, (d) Normal stress gradient in $x$ -direction as a function of $x$ -coordinate. Dashed lines indicate the location of the large grain edges. ....	110

Figure 7.7: EM response of aggregate with small crystals after 2.5 $\mu\text{s}$ for dynamic compression at strain rate of $10^3 \text{ s}^{-1}$ . (a) Electric field magnitude normalized by the applied electric field, (b) Volumetric laser heat generation rate.....	112
Figure 7.8: Response of aggregate with small crystals after 2.5 $\mu\text{s}$ for dynamic compression at strain rate of $10^3 \text{ s}^{-1}$ . (a) Normal stress, (b) Hydrostatic pressure, (c) Accumulated plastic shear strain, (d) viscous dissipated energy..	113
Figure 7.9: Response of aggregate with small crystals after 3.5 $\mu\text{s}$ for dynamic compression at strain rate of $10^3 \text{ s}^{-1}$ . (a) Normal stress, (b) Hydrostatic pressure, (c) Accumulated plastic shear strain, (d) viscous dissipated energy..	114
Figure 7.10: Temperature accumulation (normalized by initial temperature of 293 K) in aggregate with small crystals after 3.5 $\mu\text{s}$ for dynamic compression at strain rate of $10^3 \text{ s}^{-1}$ . (a) Total temperature increase, (b) Temperature increase due to laser heating, (c) Temperature increase due to plastic work, (d) Temperature increase due to viscous sliding. ....	116
Figure 7.11: EM response of aggregate without small crystals after 6 $\mu\text{s}$ for dynamic compression a strain rate of $10^3 \text{ s}^{-1}$ . (a) Electric field magnitude normalized by the applied electric field, (b) Volumetric laser heat generation rate.....	117
Figure 7.12: Response of aggregate without small crystals after 6 $\mu\text{s}$ for dynamic compression at strain rate of $10^3 \text{ s}^{-1}$ . (a) Normal stress, (b) Hydrostatic pressure, (c) Accumulated plastic shear strain, (d) viscous dissipated energy..	118
Figure 7.13: Response of aggregate without small crystals after 7 $\mu\text{s}$ for dynamic compression at strain rate of $10^3 \text{ s}^{-1}$ . (a) Normal stress, (b) Hydrostatic pressure, (c) Accumulated plastic shear strain, (d) Viscous dissipated energy.	120
Figure 7.14: Temperature accumulation (normalized by initial temperature of 293 K) in aggregate without small crystals after 7 $\mu\text{s}$ for dynamic compression at strain rate of $10^3 \text{ s}^{-1}$ . (a) Total temperature increase, (b) Temperature increase due to laser heating, (c) Temperature increase due to plastic work, (d) Temperature increase due to viscous sliding. ....	121
Figure 7.15: Nominal stress-strain curves for aggregates with and without small crystalline inclusions in the binder ligaments under coupled high strain rate loading and laser irradiation. ....	122

## **CHAPTER 1: Introduction**

### **1.1 Overview**

Energetic materials are a class of compounds that release large amounts of stored chemical energy through an exothermic reaction at very fast reaction rates. They have many applications in components where fast energy release is required, such as rocket fuels, dynamites, and plastic bonded explosives. Detonations of these materials can result in damage and losses, so it is critical to understand and predict their response to various sources of energy, including mechanical pressures, elevated temperatures, and electromagnetic (EM) radiation.

A variety of applications involve laser irradiation of energetic materials, such as remote laser-based detection [1-5], laser machining [6], and laser-induced ignition [7]. These laser-based techniques can be performed from a standoff distance, which can help to reduce safety hazards. Extensive fracture, plastic deformation, and localized hot spot formation have been observed in energetic materials subjected to high power density laser irradiation [7,8], indicating that the interaction of EM wave propagation, heat generation, and induced high strain rate mechanical loads govern the material response. It is critical, therefore, to develop a fundamental understanding of energetic aggregates under coupled laser-thermo-mechanical loading conditions to accurately predict energetic material behavior.

Three of the most commonly used energetic crystals are RDX, HMX, and PETN, all of which consist of covalently bonded organic molecules held together within a molecularly bonded crystal structure [9]. The crystal parameters and slip systems of these materials have been characterized in some detail, as shown in Table 1.1.

**Table 1.1: Crystallographic Parameters and Slip Systems for RDX, HMX, and PETN.**

Material	Space Group	Lattice Parameters (nm)	Z*	Slip systems	Ref.
RDX	<i>Pbca</i> orthorhombic	a = 1.3182 b = 1.1574 c = 1.0709	8	(010) [001], (021) [100], (02 $\bar{1}$ ) [100]	[10]
RDX	--	--	--	(021)[100], (02 $\bar{1}$ )[100]—slip (011)[100], (0 $\bar{1}$ 1)[100]—slip (010)[100]—cross slip	[11]
HMX	<i>P2<sub>1</sub>/c</i> monoclinic	a = 0.654 b = 1.105 c = 1.0709 $\beta$ = 124.3°	2	(101)[10 $\bar{1}$ ]—twinning (101)[10 $\bar{1}$ ], (001)[100]—slip	[12,13]
PETN	<i>P<math>\bar{4}</math>2<sub>1</sub>c</i> tetragonal	a = 0.938 b = 0.938 c = 0.67	2	(110) [111], (110) [1 $\bar{1}$ 1], ( $\bar{1}$ 10)[111], ( $\bar{1}$ 10) [ $\bar{1}$ 11]	[10]

\* Z denotes the number of molecules per unit cell

Due to the nature of intermolecular bonding and the size and shape of the organic molecules, slip systems available for plastic deformation are limited and unique to each material. Gallagher *et. al.* [10] have identified three unique slip systems in RDX through Knoop hardness indentation experiments. More recent nanoindentation experiments by Ramos *et. al.* [11] report observation of six total slip systems, although they also conjecture that RDX, in general, does not possess five independent slip systems to accommodate general strain distributions and there may be only three independent strain components. In HMX, the plastic deformation mechanisms are based on twinning on the (101)[10 $\bar{1}$ ] system and slip on (101)[10 $\bar{1}$ ] and (001)[100] systems [12], while PETN has four symmetrically equivalent slip systems of the (110) [1 $\bar{1}$ 1]-type [10]. In contrast to metals, where favorable slip systems are governed largely by the inter-planar spacing and shortest lattice translation

distances, the complex, irregularly shaped organic molecules in energetic crystals can cause certain lattice translations on otherwise favorable slip planes to result in energetically unfavorable inter-molecular contacts. Such steric effects appear to govern the favorable slip systems in RDX and PETN, and can explain the unique deformation mechanisms observed in these materials [10].

Energetic crystals are often embedded within a polymer binder to form energetic aggregates used as plastic bonded explosives (PBX) and solid rocket propellants [9]. Commonly used binders include estane, polychlorotrifluoroethylene (PCTFE), and hydroxyl-terminated polybutadiene (HTPB), which are typically present in 5 – 30% volume fractions and add mechanical stability and adhesion between the energetic crystals [14-18]. Additionally, defects including voids, solvent particle inclusions, and dislocations further contribute to the heterogeneous microstructure of energetic aggregates. The primary initiation mechanism occurs when an external stimulus causes heat build-up in localized “hot spots” faster than it can be conducted into the bulk material [19,20]. The high temperatures generated at a hot spot accelerate the local exothermic decomposition reaction and can lead to widespread deflagration and possible detonation [21].

The heterogeneous microstructure of energetic aggregates creates multiple pathways for energy localization under EM, thermal, and mechanical stimuli. Several microstructural characteristics of energetic materials, such as voids [20,22-24], shear banding [25], dislocation pile-ups [26,27], and crystal size [28] have been proposed to affect hot spot formation in energetic materials subjected to mechanical loads. Additionally, crystalline grain-boundaries (GBs), dislocations [7,29], and absorbing particle inclusions [7,30], can



facilitate hot spot formation due to laser electromagnetic energy localization, which is governed by dielectric heterogeneity between the various crystal, binder, and defect constituents. Furthermore, laser energy localization can dominate at wavelengths that are weakly absorbed by the energetic crystals, due to larger penetration depths and greater interactions with defects [31,32]. EM wave scattering and attenuation within PBX materials is also strongly dependent on EM wave frequency and crystal size [33].

Modeling efforts of laser interaction with energetic materials have accounted for varying features of the material's microstructure. Works by Abdulazeem et al. [34] and Khaneft et al. [35] used an analytical Beer-Lambert absorption profile to model laser heating of pure energetic crystals without considering any EM wave propagation effects. Additionally, Wood et al. [36] used molecular dynamics simulations to investigate EM laser induced decomposition in  $\alpha$ HMX molecules at very high power densities and short time scales on the order of picoseconds. Lee Perry et al. [30] used an EM finite-element model loosely coupled with heat and mass transport models to predict EM wave propagation and subsequent laser-induced ignition in homogeneous HMX containing a single SiC inclusion particle. Damm et al. [37] modeled laser heating in CP ([5-cyanotetrazolato- $N^2$ ] penta-amminecobalt (III) perchlorate) pressed powders with carbon black inclusion particles assuming an isotropically scattering medium formulation to describe the EM wave propagation. Zurk et al. [33] used a dense medium model within the quasi-crystalline approximation to account for the multiple scattering between dielectric particles and predict an effective wave vector for THz wave propagation through granular PBX simulant aggregates.

Complex microstructure features present in energetic aggregates, such as crystal-binder interfaces, crystal morphology, polymer binder volume fraction, voids, grain boundaries, and dislocation densities, therefore, would strongly affect EM wave propagation and the coupled thermo-mechanical behavior. Thus, an integrated modeling approach that couples the effects of high frequency EM wave propagation and thermo-mechanical behavior with the material microstructure is needed to understand and predict energetic material behavior and potential hot spot formation during laser irradiation.

## **1.2 General Research Objectives and Approach**

The objectives of this work were to identify coupling mechanisms between the inelastic deformation, EM wave propagation, heat generation, and microstructural evolution present during laser irradiation and to develop a fundamental understanding of the coupled response of energetic aggregates. This will build knowledge of how heterogeneous microstructural features, such as crystal sizes, interfaces and grain boundaries, dislocation densities, voids, polymer binder behavior, and electromagnetic absorption affect the response at different laser intensities and wavelengths. Such understanding will facilitate the ability to control features of energetic aggregates responsible for hot spot formation and may ultimately lead to better methods of stand-off detection or ignition.

Hence, a computational approach was developed that couples high-frequency EM wave propagation, absorption, and heat generation, with a thermo-mechanical dislocation-density based crystalline plasticity formulation to fundamentally understand and predict the coupled response of energetic aggregates under infrared laser irradiation. The model includes the effects of conduction and internal heat generation sources due to mechanical plastic

deformation, the exothermic chemical decomposition reaction, and laser-induced heating, which is modeled as a function of material electromagnetic absorption coefficient and local electric field intensity.

Laser induced hot spot formation mechanisms were studied in RDX-PCTFE aggregates, where the PCTFE binder was modeled as a hypo-elastic material since laser induced temperatures were below its glass transition temperature. These aggregates were studied using both an analytical distribution for laser heating following Beer-Lambert absorption and the full EM finite element method to obtain the laser heating distribution. The laser heat distribution was then coupled to the thermo-mechanical domain to determine the effects of material absorption coefficient, laser intensity, inelastic deformation, voids, and dislocation densities on hot spot formation mechanisms.

Additionally, the coupled EM-thermo-mechanical response of RDX-estane aggregates was studied to include the effects of viscous deformation of the binder above its glass transition temperature. Several different RDX-estane aggregates were modeled under laser irradiation and high strain rate loads to understand the effects of microstructure morphology, aggregate size, binder volume fraction, and non-uniform crystal size distributions on EM and shear strain localization.

### **1.3 Dissertation Organization**

This dissertation is organized as follows: Chapter 2 presents the dislocation density based crystalline plasticity and finite viscoelastic material constitutive relations, formulation for high frequency EM wave propagation, and the electromagnetic-thermo-mechanical coupling mechanisms. Chapter 3 presents the numerical approach developed to couple EM

and thermo-mechanical phenomena and specialized finite element techniques used to obtain the thermo-mechanical quantities. Chapter 4 presents results from a study of laser-induced hot spot formation in RDX-PCTFE aggregates with various absorption coefficients. Chapter 5 presents the effect of laser intensity and microstructural defects on hot spot formation in RDX-PCTFE aggregates. Chapter 6 presents a discussion on the effect of microstructure morphology, aggregate size, and viscous binder sliding on EM localization in RDX-estane aggregates. Chapter 7 presents the effects of small crystals embedded within the binder ligaments, which are present in many energetic aggregates, on the coupled EM-thermo-mechanical response of RDX-estane aggregates and behavior at the crystal-crystal and crystal-binder interfaces.

## CHAPTER 2: Material Constitutive Formulations and Electromagnetic-Thermo-Mechanical Coupling

This section presents the dislocation density-based crystalline plasticity formulation used for the RDX crystals, hypo-elastic and finite viscoelastic formulations used for the polymer binder, and the governing equations for EM wave propagation in dielectric materials. The EM-thermo-mechanical coupling mechanisms that form the basis of the laser-material interaction are presented.

### 2.1 Multiple Slip, Dislocation Density-Based Crystalline Plasticity Formulation

The dislocation-density based crystal plasticity constitutive framework used in this study is based on the formulation developed by Zikry [38], Ashmawi and Zikry [39], and Shanthraj and Zikry [40], and is outlined in the following sections.

#### 2.1.1 Crystalline Plasticity Kinematics

The velocity gradient tensor,  $L_{ij}$ , is calculated from the deformation gradient as

$$L_{ij} = \dot{F}_{ij} F_{ij}^{-1}. \quad (2.1)$$

The velocity gradient is then further decomposed into the symmetric deformation rate tensor,  $D_{ij}$  and an anti-symmetric spin tensor  $W_{ij}$ . It is assumed that the tensors  $D_{ij}$  and  $W_{ij}$  can be additively decomposed into elastic (<sup>e</sup>) and inelastic (<sup>p</sup>) components as

$$D_{ij} = D_{ij}^e + D_{ij}^p, \quad W_{ij} = W_{ij}^e + W_{ij}^p, \quad (2.2)$$

where  $W_{ij}^e$  includes the rigid body spin. The plastic parts are related to the crystallographic slip rates as

$$D_{ij}^p = P_{ij}^{(\alpha)} \dot{\gamma}^{(\alpha)}, \quad W_{ij}^p = \omega_{ij}^{(\alpha)} \dot{\gamma}^{(\alpha)}, \quad (2.3)$$

where  $\alpha$  is summed over all slip-systems, and  $P_{ij}^{(\alpha)}$  and  $\omega_{ij}^{(\alpha)}$  are the symmetric and antisymmetric parts of the Schmid tensor in the current configuration, respectively.

These are defined in terms of the slip plane normal ( $n_i$ ) and slip directions ( $s_j$ ) as

$$P_{ij}^{(\alpha)} = \frac{1}{2} \left( s_i^{(\alpha)} n_j^{(\alpha)} + s_j^{(\alpha)} n_i^{(\alpha)} \right) \quad \text{and} \quad \omega_{ij}^{(\alpha)} = \frac{1}{2} \left( s_i^{(\alpha)} n_j^{(\alpha)} - s_j^{(\alpha)} n_i^{(\alpha)} \right). \quad (2.4)$$

The effective plastic shear slip,  $\gamma_{eff}$ , is calculated from the plastic deformation rate tensor as

$$\gamma_{eff} = \frac{2}{3} \int \sqrt{D_{ij}^p D_{ij}^p} dt, \quad (2.5)$$

to provide a measure of plastic strain accumulation over time.

The objective stress rate is given by

$$\sigma_{ij}^A = L_{ijkl} (D_{kl} - D_{kl}^p) - W_{ik}^p \sigma_{kj} - W_{jk}^p \sigma_{ki}, \quad (2.6)$$

where  $L_{ijkl}$  is the elastic modulus fourth-order tensor of the crystal.

A power law hardening relation is assumed to obtain the slip rate ( $\dot{\gamma}^{(\alpha)}$ ) on each slip system  $\alpha$  as

$$\dot{\gamma}^{(\alpha)} = \dot{\gamma}_{ref}^{(\alpha)} \left[ \frac{\tau^{(\alpha)}}{\tau_{ref}^\alpha} \right] \left[ \frac{\tau^{(\alpha)}}{\tau_{ref}^\alpha} \right]^{(1/m)-1} \quad \text{no sum on } \alpha, \quad (2.7)$$

where  $\tau^{(\alpha)}$  is the resolved shear stress, and  $\dot{\gamma}_{ref}^{(\alpha)}$  is the reference shear strain-rate which corresponds to a reference shear stress  $\tau_{ref}^{(\alpha)}$ . The strain rate sensitivity parameter,  $m$ , is obtained as

$$m = \frac{\partial \ln \tau^{(\alpha)}}{\partial \ln \dot{\gamma}^{(\alpha)}}. \quad (2.8)$$

The reference stress used is a modification of widely used classical forms[41] that relate reference stress to immobile dislocation-density  $\rho_{im}$  as

$$\tau_{ref}^{(\alpha)} = \left( \tau_y^{(\alpha)} + G \sum_{\beta=1}^{nss} b^{(\beta)} \sqrt{a_{\alpha\beta} \rho_{im}^{(\beta)}} \right) \left( \frac{T}{T_0} \right)^{-\xi}, \quad (2.9)$$

where  $\tau_y^{(\alpha)}$  is the static yield stress on slip system  $\alpha$ ,  $G$  is the shear modulus,  $nss$  is the number of slip systems,  $b^{(\beta)}$  is the magnitude of the Burgers vector, and  $a_{\alpha\beta}$  are Taylor coefficients which are related to the strength of interactions between slip-systems [42]. Additionally, the effects of temperature are considered, where  $T$  is the temperature,  $T_0$  is the reference temperature (293 K), and  $\xi$  is the thermal softening exponent. The Taylor coefficients,  $a_{\alpha\beta}$ , are obtained using Frank's rule to determine energetically favorable interactions for immobile dislocation density junction formation [43]. For RDX crystals, the six interactions of self-interaction, co-linear interaction, co-planar interaction, Lomer locks, glissile junctions, and Hirth locks [44] are considered, but only self-interaction is found to be energetically favorable. Thus,  $a_{\alpha\beta}$  is assumed to be 0.6 for self-interactions on each slip system and  $a_{\alpha\beta}$  for the other interactions is set equal to zero.

### 2.1.2 Dislocation Density Evolution

Following the approach of Zikry and Kao [45], it is assumed that, for a given deformed state of the material, the total statistically stored dislocation-density,  $\rho^{(\alpha)}$ , can be additively decomposed into a mobile,  $\rho_m^{(\alpha)}$ , and an immobile dislocation-density,  $\rho_{im}^{(\alpha)}$  as

$$\rho^{(\alpha)} = \rho_{im}^{(\alpha)} + \rho_m^{(\alpha)} \quad (2.10)$$

During an increment of slip, mobile dislocations may be generated, immobile dislocations may be annihilated, and junctions may be formed or destroyed due to interaction between dislocations on the various slip systems. It is assumed that the mobile and immobile dislocation-density evolution rates can be coupled through various interaction mechanisms, including the formation and destruction of junctions as the stored immobile dislocations act as obstacles for evolving mobile dislocations. Thus, the mobile and immobile dislocation density evolution rates are governed by coupled differential equations as

$$\dot{\rho}_m^{(\alpha)} = \dot{\rho}_{generation}^{(\alpha)} - \dot{\rho}_{interaction-}^{(\alpha)} \quad (2.11)$$

$$\dot{\rho}_{im}^{(\alpha)} = \dot{\rho}_{interaction+}^{(\alpha)} - \dot{\rho}_{annihilation}^{(\alpha)} . \quad (2.12)$$

The dislocation density evolution follows the formulation of Shanthraj and Zikry [43], and a brief summary is given in the following discussion. Dislocation density generation is related to Frank Read sources, where  $g_{sour}$  is a coefficient pertaining to an increase in the mobile dislocation-density due to dislocation sources. Trapping of mobile dislocations due to forest intersections, cross-slip around obstacles, or dislocation interactions is described by  $g_{mnter}$ , and the immobilization of mobile dislocations is described by  $g_{immob}$ . The rearrangement and annihilation of immobile dislocations through recovery processes is given by  $g_{recov}$ , and is modeled using an Arrhenius relationship dependent on the frequency of intersection between immobile and mobile dislocations, activation enthalpy, and the local temperature. These coefficients are not known beforehand, but are obtained as a function of the deformation mode as outlined in Shanthraj and Zikry [43] and shown in Table 2.1.



**Table 2.1: Summary of g-Coefficients for Dislocation Density Evolution Equations**

Coefficient	Expression
$g_{sour}^{\alpha}$	$b^{\alpha} \phi \sum_{\beta} \sqrt{\rho_{im}^{\beta}}$
$g_{minter-}^{\alpha}$	$l_c f_0 \sum_{\beta} \left[ \frac{\rho_m^{\beta}}{\rho_m^{\alpha} b^{\alpha}} + \frac{\dot{\gamma}^{\beta}}{\dot{\gamma}^{\alpha} b^{\beta}} \right]$
$g_{immob-}^{\alpha}$	$\frac{l_c f_0}{\sqrt{\rho_{im}^{\alpha}}} \sum_{\beta} \rho_{im}^{\beta}$
$g_{minter+}^{\alpha}$	$\frac{l_c f_0}{\dot{\gamma}^{\alpha} \rho_m^{\alpha}} \sum_{\beta, \gamma} n_{\alpha}^{\beta \gamma} \left[ \frac{\rho_m^{\gamma} \dot{\gamma}^{\beta}}{b^{\beta}} + \frac{\rho_m^{\beta} \dot{\gamma}^{\gamma}}{b^{\gamma}} \right]$
$g_{immob+}^{\alpha}$	$\frac{l_c f_0}{\dot{\gamma}^{\alpha} \sqrt{\rho_{im}^{\alpha}}} \sum_{\beta} n_{\alpha}^{\beta \gamma} \rho_{im}^{\gamma} \dot{\gamma}^{\beta}$
$g_{re cov}^{\alpha}$	$\frac{l_c f_0}{\dot{\gamma}^{\alpha}} \left( \sum_{\beta} \frac{\dot{\gamma}^{\beta}}{b^{\beta}} \right) e^{\left( \frac{-H_0 \left( 1 - \sqrt{\frac{\rho_{im}^{\alpha}}{\rho_s}} \right)}{kT} \right)}$

Substituting the expressions for the coefficients in Table 2.1 into Equations (2.11-2.12), the evolution of mobile and immobile dislocation densities is obtained as

$$\frac{d\rho_m^{\alpha}}{dt} = |\dot{\gamma}^{\alpha}| \left( \frac{g_{sour}^{\alpha}}{b^2} \left( \frac{\rho_{im}^{\alpha}}{\rho_m^{\alpha}} \right) - g_{minter-}^{\alpha} \rho_m^{\alpha} - \frac{g_{immob-}^{\alpha}}{b} \sqrt{\rho_{im}^{\alpha}} \right), \quad (2.13)$$

$$\frac{d\rho_{im}^{\alpha}}{dt} = |\dot{\gamma}^{\alpha}| \left( g_{minter+}^{\alpha} \rho_m^{\alpha} + \frac{g_{immob+}^{\alpha}}{b} \sqrt{\rho_{im}^{\alpha}} - g_{re cov}^{\alpha} \rho_{im}^{\alpha} \right). \quad (2.14)$$

The dislocation activity is then coupled to the stress response through Equation (2.9).

## 2.2 Constitutive Formulations for Polymer Binders

The constitutive relation for the polymer binder was chosen based on the polymer glass transition temperature. For the PCTFE binder, the glass transition temperature is approximately 50° C, and the temperatures due to the EM and adiabatic heating would be lower than this glassy temperature [17]. Thus, PCTFE is modeled as a hypo-elastic material based on the first term of Equation (2.6). For the estane binder, temperatures generated by laser irradiation are well above the glass transition temperature, which is approximately -40°C [46]. Thus, a finite viscoelastic constitutive relation is used to account for the nonlinear viscous relaxation behavior at operating temperatures above the glass transition of estane.

### 2.2.1 Finite Viscoelastic Formulation

Following a generalized Maxwell model based on the approach of Kaliske and Rothert [47], the stresses are decomposed into deviatoric and hydrostatic components, where the deviatoric component exhibits rate-sensitivity and the hydrostatic component exhibits rate-insensitivity.

The hydrostatic stress is updated using finite elasticity through the deformation-rate tensor and the Jaumann rate of Cauchy stress as

$$\hat{\sigma}_{HYD}^n = \mathbb{C}^{HYD} \cdot D^{HYD} + \sigma_{HYD}^n \cdot W - W \cdot \sigma_{HYD}^n, \quad (2.15)$$

where  $D^{HYD}$  is the hydrostatic component of the deformation rate tensor,  $\sigma_{HYD}^n$  is the hydrostatic stress at the current time step, and  $W$  is the total spin tensor.  $\mathbb{C}^{HYD}$  is the isotropic elastic material matrix for plane strain.

The deviatoric stress is updated as the sum of contributions from each element in the Maxwell model as

$$\sigma_{DEV}^{n+1} = \sigma_{0\,DEV}^{n+1} + \sum_{j=1}^{22} H_j^{n+1}, \quad (2.16)$$

where  $\sigma_{0\,DEV}^{n+1}$  is the deviatoric component of the lone spring, and  $H_j^{n+1}$  is the viscous stress corresponding to spring-dashpot element  $j$ . The viscous stress in each spring-dashpot element is updated as

$$H_j^{n+1} = H_j^n \cdot e^{-\frac{\Delta t}{\tau_j}} + \left(\frac{G_j}{G_0}\right) \cdot \left(\frac{1 - e^{-\frac{\Delta t}{\tau_j}}}{\frac{\Delta t}{\tau_j}}\right) \cdot (\sigma_{0\,DEV}^{n+1} - \sigma_{0\,DEV}^n), \quad (2.17)$$

where  $H_j^n$  is the viscous stress at the current time step,  $\Delta t$  is the time step size,  $\tau_j$  is the relaxation time,  $G_j$  is the shear modulus of the spring-dashpot element,  $G_0$  is the shear modulus of the lone spring, and  $\sigma_{0\,DEV}^n$  is the deviatoric component of the lone spring at the current timestep. The time-temperature superposition theory of Williams, Landel and Ferry (WLF) [48] is used to modify the relaxation times through the use of a shift factor,  $a_T$ . Mas et al. [46] have fitted temperature data for estane to a WLF equation as

$$\log(a_T) = \frac{-6.5(T-T_0)}{120+(T-T_0)}, \quad (2.18)$$

where  $T_0$  is a reference temperature and  $T$  is the current temperature. The relaxation time for the Maxwell element  $j$  is related to the temperature shift factor as

$$\tau_j = 1.5a_T 10^{(7-j)}. \quad (2.19)$$

### 2.3 Electromagnetic Formulation for Laser Wave Propagation

EM wave propagation within a material is governed by Maxwell's equations and the material's electrical properties. By combining Maxwell-Ampère's and Faraday's laws, the following differential equation is obtained to describe the electric field within the material, where  $\vec{E}$  is the electric field vector,  $\lambda$  is the wavelength,  $\omega$  is angular frequency, and  $\epsilon_0$  is the permittivity of vacuum.

$$\nabla \times \left( \frac{1}{\mu_r} \nabla \times \vec{E} \right) - \left( \frac{2\pi}{\lambda} \right)^2 \left( \epsilon_r - \frac{\sigma}{\omega \epsilon_0} i \right) \vec{E} = 0. \quad (2.20)$$

The parameter  $\mu_r$  is the magnetic permeability,  $\epsilon_r$  is the electrical permittivity, and  $\sigma$  is the electrical conductivity. The subscript  $r$  denotes that the value is relative to the corresponding property of vacuum. The electrical permittivity is also related to the material refractive index through

$$\epsilon_r = (n - ki)^2, \quad (2.21)$$

where the real part ( $n$ ) governs wave speed and wavelength inside the material and the imaginary part ( $k$ ) governs the material's ability to absorb the EM energy.

Equation (2.20) is based on the assumption that the material has linear electrical constitutive relations and that the EM field varies harmonically with time as

$$\vec{E} = \vec{E}(x, y, z)e^{-i\omega t}. \quad (2.22)$$

It is assumed that a harmonic electric field is appropriate to model laser pulses with microsecond durations, as EM transients generally occur much faster on the order of picoseconds.

Most energetic materials are dielectrics with very low electrical conductivity and unique absorption spectra in the infrared wavelength range corresponding to molecular

structure in the crystals [33]. Thus, it is further assumed that the material is non-magnetic ( $\mu_r = 1$ ) and non-conducting ( $\sigma = 0$ ). With these assumptions and combining Equations (2.20 – 2.21), the EM wave propagation in a dielectric material is described by

$$\nabla \times (\nabla \times \vec{E}) - \left(\frac{2\pi}{\lambda}\right)^2 (n - ki)^2 \vec{E} = 0. \quad (2.23)$$

This equation is solved to obtain the electric field distribution throughout the material as a result of laser irradiation.

## 2.4 Coupling of Electromagnetic and Thermo-Mechanical Behavior

The primary coupling mechanism for dielectric materials occurs as the propagating EM wave is absorbed and converted to heat within the material. Assuming that all energy absorbed is converted to heat, the volumetric laser heat generation rate is equal to the EM power loss density given by the dot product of electric field and current density ( $\vec{J}$ ) as

$$\dot{q}_{laser} = \vec{E} \cdot \vec{J}. \quad (2.24)$$

Although the conduction current is assumed to be zero in such dielectric materials, bound charges switch polarization under the time-varying electric field and produce a non-zero displacement current given by

$$\vec{J} = \epsilon_0 (n - ki)^2 \frac{\partial \vec{E}}{\partial t}. \quad (2.25)$$

Combining Equation (2.22) with Equations (2.24 – 2.25) and taking the time average value for harmonic steady state wave propagation yields the following expression for laser heat generation rate as

$$\dot{q}_{laser} = |\vec{E}|^2 \frac{1}{2} c \epsilon_0 n \left(\frac{4\pi k}{\lambda}\right). \quad (2.26)$$

Equation (2.26) can also be written as the product of the electric field intensity,  $I$ , and material absorption coefficient,  $\alpha$ , by considering their relationship with electric field and material refractive index as

$$\alpha = \frac{4\pi k}{\lambda}, \quad (2.27)$$

$$I = |\vec{E}|^2 \frac{1}{2} c \epsilon_0 n. \quad (2.28)$$

In addition to the laser-induced heating, thermo-mechanical heat generation sources are assumed to occur. During high strain-rate deformation, heat is generated in crystalline materials as the material undergoes plastic work and builds up much faster than conduction away from the deformed area can occur. Thus, adiabatic heat generation due to mechanical energy in crystalline materials is given as

$$\dot{q}_{mechanical} = \chi \sigma'_{ij} \dot{D}_{ij}^P, \quad (2.29)$$

where  $\chi$  is the fraction of plastic work converted to heat, and  $\sigma'_{ij}$  is the deviatoric stress.

Energetic crystals can also produce heat through an exothermic thermal decomposition reaction, which is assumed to occur as a single-step Arrhenius exothermic process [49] as

$$\dot{q}_{decomposition} = \rho \Delta H Z e^{\frac{-E_a}{RT}}, \quad (2.30)$$

where  $\rho$  is the mass density,  $\Delta H$  is the heat of decomposition,  $Z$  is a pre-exponential factor,  $E_a$  is the activation energy of decomposition,  $R$  is the universal gas constant, and  $T$  is the current temperature. Heat generated due to viscous sliding in the polymer [50] is given as

$$\dot{q}_{viscous} = \sum_{j=1}^{22} \frac{H_j^{n+1} : H_j^{n+1}}{4 G_j \tau_j}. \quad (2.31)$$

Equations (2.26, 2.29 – 2.31) are used as heat sources to the Fourier heat equation, which couples their effects with conduction and temperature build up. Thus, the temperature distribution ( $T$ ) resulting from dielectric laser heating, adiabatic heat generation from plastic work, and thermal decomposition mechanisms is obtained as

$$\rho c_p \left( \frac{\partial T}{\partial t} \right) = \lambda \nabla^2 T + \dot{q}_{mechanical} + \dot{q}_{decomposition} + \dot{q}_{laser} + \dot{q}_{viscous}, \quad (2.32)$$

where  $\rho$  is density,  $c_p$  is specific heat at constant pressure, and  $\lambda$  is thermal conductivity.

## CHAPTER 3: Numerical Methods

The computational framework used to couple the high frequency electromagnetic wave propagation discussed in Section 2.3 with the evolution of stresses, temperatures, and other thermo-mechanical quantities is presented in Section 3.1. Additionally, the specialized finite element scheme used in the thermo-mechanical domain to obtain the velocity gradient tensors and temperature distribution is outlined in Section 3.2.

### 3.1 Framework for Coupling EM and Thermo-Mechanical Domains

EM wave propagation, thermal conduction, and inelastic deformation occur on different time and length scales associated with the physical system of interest. For thermo-mechanical processes, the length scale is related to the microstructural features and temperature gradients that must be resolved, and the time scale is associated with the propagating inelastic wave speed and material thermal diffusivity. The various microstructural constituents of energetic aggregates range between 10 to 200  $\mu\text{m}$ , and the timescale associated with dynamic inelastic wave propagation ranges from ms to ns. The time and length scales of interest for EM wave propagation are associated with the EM wavelength and wave speed in a medium, and finite elements used to discretize Equation (2.23) are approximately on the order of five times smaller than the EM wavelength. This requires elements no larger than 2  $\mu\text{m}$  to resolve the infrared wavelengths considered in this study, which is significantly smaller than element sizes required to resolve the microstructural features. Additionally, the EM wave speed is much faster than the inelastic wave speed, and EM waves will traverse a given distance several orders of magnitude faster than inelastic waves.



A different finite-element mesh and solution must, therefore, be used for the EM domain, than the one used for the thermo-mechanical domain. This is accomplished through a computational framework that solves the EM and thermo-mechanical problems using separate domains and passes information sequentially between them (Figure 3.1).

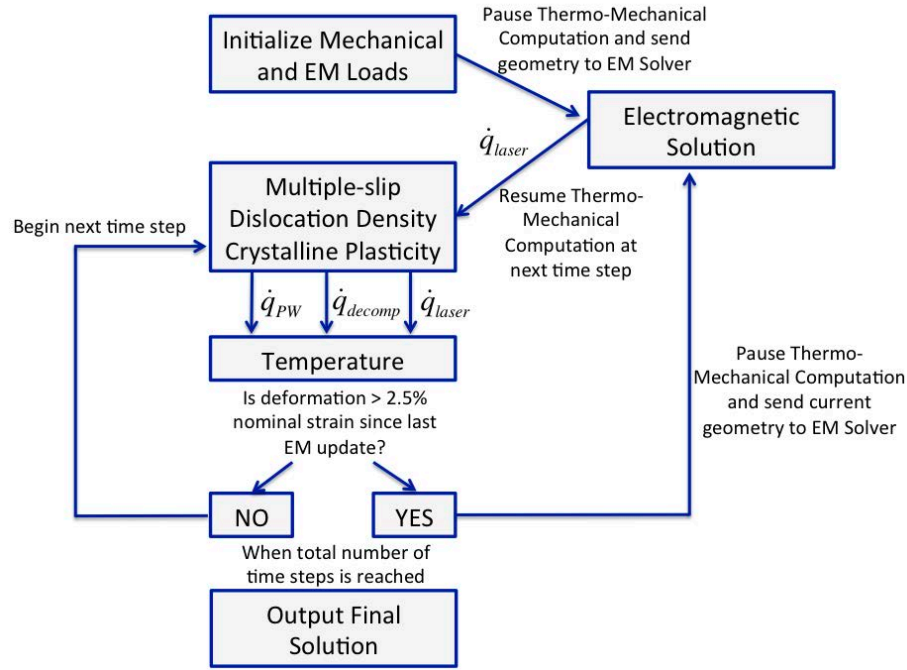


**Figure 3.1: Computational algorithm for coupled electromagnetic-thermo-mechanical model.**

The thermo-mechanical calculation is done so that quantities such as dislocation density and temperature evolution may be tracked during dynamic inelastic wave propagation. Since the EM wave speed is several orders of magnitude faster than the inelastic wave speed, it is assumed that the electric field has reached steady state conditions during a single thermo-mechanical time step. The commercial software COMSOL Multiphysics is used to obtain the electric field distribution according to the finite element

solution of Equation (2.23), and the associated volumetric laser heat generation rate is mapped to the thermo-mechanical domain.

As shown in Figure 3.1, an initial EM solution is obtained before the thermo-mechanical computation is initiated. The laser heat distribution  $\dot{q}_{laser}$  is passed to the thermo-mechanical domain and mapped onto the thermo-mechanical mesh. The multiple-slip dislocation density based crystalline plasticity constitutive model is then used to obtain thermo-mechanical deformation and heat generation, which are then combined with the laser heat generation to obtain the temperatures by Equation (2.32).

Since changes in the microstructure may affect EM wave propagation, it is necessary to consider this effect by re-calculating the laser heat generation rate using the current deformed microstructure. However, to do this at every time step would be computationally expensive and is not necessary as long as the deformation that occurs during a single time step is relatively small. Therefore, information is passed between the different domains at nominal strain increments of 2.5%. If the nominal strain is less than 2.5% since the last EM update, the thermo-mechanical computation continues on to the next time step and uses the laser heating values obtained from the most recent EM update. If the nominal strain increment is equal to 2.5%, however, the thermo-mechanical computation is paused while a new EM solution is obtained with the current deformed geometry. This new distribution of  $\dot{q}_{laser}$  is then mapped back to the thermo-mechanical domain and used until the next EM update.

### 3.1.1 Mapping Methods Between EM and Thermo-Mechanical Domains

For the energetic aggregates and laser wavelengths considered in this study, the elements used in the EM domain are 10-20 times smaller than the elements used in the thermo-mechanical domain. Consequently, the mapping method shown in Figure 3.2 is used to map the laser heat generation rate from the EM domain to the thermo-mechanical domain.

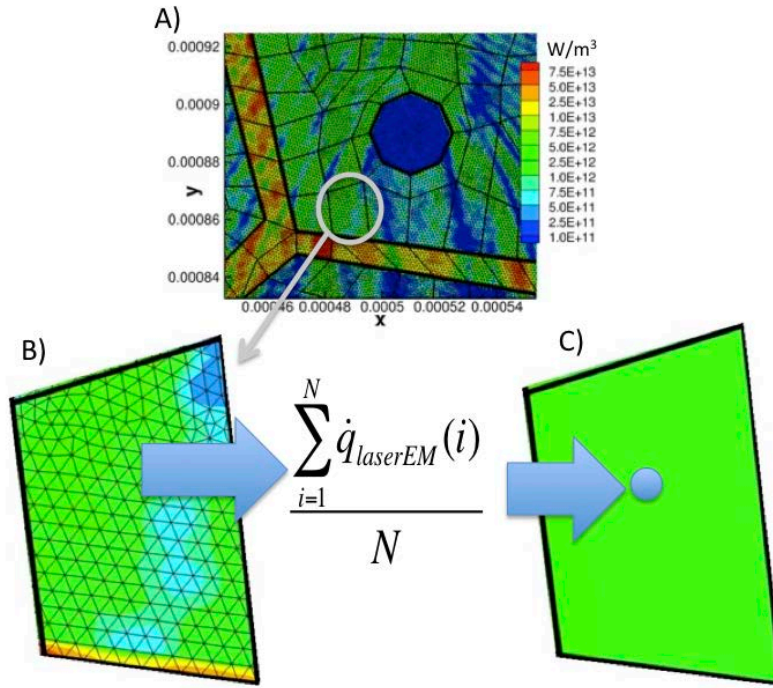


**Figure 3.2: Mapping method for transfer of laser heat generation rate from EM domain to thermo-mechanical domain. (a) Zoomed-in view of model with EM and thermo-mechanical meshes superimposed, (b) Enlarged view from circled region of (a), (c) Element of thermo-mechanical mesh with average laser heat generation rate calculated from (b) applied as a constant value.**

The thermo-mechanical mesh is superimposed on the EM mesh (Figure 3.2(a)), and the EM elements are sorted according to which thermo-mechanical element they are located within. The laser heat generation rate assigned to each thermo-mechanical element ( $\dot{q}_{laserTM}$ ) is then determined by averaging the laser heat generation rate of all the EM

elements ( $\dot{q}_{laserEM}$ ) contained inside that particular thermo-mechanical element (Figure 3.2(b-c)) as

$$\dot{q}_{laserTM} = \frac{\sum_{i=1}^N \dot{q}_{laserEM}(i)}{N}, \quad (3.1)$$

where  $N$  is the number of EM elements contained inside each thermo-mechanical element.

When updating the EM solution, the current nodal coordinates of the thermo-mechanical mesh are used to create a new model in the EM domain with geometry identical to the deformed thermo-mechanical domain. A new EM mesh is then generated for this configuration, and it is used to obtain the updated electric field distribution and laser heat generation rate from Equations (2.23) and (2.26).

### 3.2 Numerical Methods in Thermo-Mechanical Domain

The total deformation rate tensor,  $D_{ij}$ , and the plastic deformation rate tensor,  $D_{ij}^p$ , are needed to update the material stress state through the constitutive formulation presented in Chapter 2. These quantities are obtained through a specialized finite element scheme developed by Zikry [38] for rate-dependent crystalline plasticity formulations and summarized here.

#### 3.2.1 Determination of the Total Velocity Gradient

The total velocity gradient is calculated from the nodal displacements obtained by finite element analysis with Q4 quadrilateral elements. The deformation calculated by the finite element method is used to calculate the total velocity gradient in accordance with Equation (2.1). For quasi-static analysis, an incremental, iterative approach using the quasi-Newton BFGS scheme is used to determine the nodal displacements. For dynamic analyses,

an implicit Newmark- $\beta$ , iterative approach using BFGS to solve the finite element equations linearized about  $t_n$  at each timestep is used. Trapezoidal values of  $\beta = 1/4$  and  $\gamma = 1/2$  were chosen for unconditional stability of the finite element method. Details for this dynamic approach are given by Shanthraj and Zikry [43].

To avoid numerical locking due to incompressible pressure constraints, 1-point integration of the Q4 quadrilateral element is used, which has the added benefit of reduced computational time. However, reduced integration can lead to the zero-energy numerical instability of hourglassing. Stiffness-based hourglass control is implemented to control the hourglass instability following the method of Flanagan and Belytschko [51].

### 3.2.2 Determination of the Plastic Velocity Gradient

The objective stress rate is coupled with the time derivative of the resolved shear stresses to determine the resolved shear stresses on each slip plane given by

$$\dot{\tau}^{(\alpha)} = \frac{d}{dt} \left( P_{ij}^{(\alpha)} \sigma_{ij} \right), \quad (3.2)$$

$$\dot{\tau}^{(\alpha)} = C_{ijkl} P_{ij}^{(\alpha)} D_{kl}^{el}, \quad (3.3)$$

Equation (3.3) can be expanded to

$$\dot{\tau}^{(\alpha)} = 2\mu P_{ij}^{(\alpha)} \left[ D_{ij} - \sum_{\xi=1, nss} P_{ij}^{(\xi)} \dot{\gamma}_{ref}^{(\xi)} \left( \frac{\tau^{(\xi)}}{\tau_{ref}^{(\xi)}} \right)^{\frac{1}{m}} \right], \quad (3.4)$$

where the reference stress is a function of the immobile dislocation density. The slip rates can be determined using the resolved shear stress (Equation (2.9)). The plastic deformation rate tensor and spin rate tensor can then be used along with the Schmid tensor and slip rates to determine the plastic velocity gradient (Equation (2.3)).

The elastic spin rate tensor can be determined as a function of the total spin rate tensor and the plastic spin rate tensor using Equation (2.2). It was assumed in the derivation of Equation (3.4) that the time rate of change of the slip normals and directions is related to the lattice spin as

$$\dot{n}_i^{(\alpha)} = W_{ij}^{el} n_j \quad \text{and} \quad \dot{s}_i^{(\alpha)} = W_{ij}^{el} s_j. \quad (3.5)$$

The non-linear ODE's governing the resolved shear stresses and dislocation density evolution necessitate a solution method that is both accurate and stable due to their non-linear nature and the possibility of numerical stiffness [38]. The non-linear nature of the problem requires a solution method with high order accuracy, while the possibility of numerical stiffness requires a solution method that is stable and will not propagate error due to stiff behavior.

An adaptive timestep fifth-order accurate step halving Runge-Kutta method is employed. Two approximate solutions are taken using the fourth-order Runge-Kutta method, one at step length  $h$  and a second with two steps of length  $h/2$ .

$$\tau(t+h) = \hat{\tau}_1 + (h)^5 \phi + O(h^6) + \dots \quad (3.6)$$

$$\tau(t+2(h/2)) = \hat{\tau}_2 + 2(h/2)^5 \phi + O(h^6) + \dots \quad (3.7)$$

The two solutions are combined to yield

$$\tau(t+h) = \hat{\tau}_2 + \frac{\Delta_1}{15} + O(h^6), \quad (3.8)$$

where  $\Delta_1 = \hat{\tau}_1 - \hat{\tau}_2$  is the local truncation error, which is used to measure the accuracy of the solution. If the accuracy is not less than a specified tolerance,  $\Delta_0$ , the timestep size is reduced by

$$h_{new} = F h_{old} \left| \frac{\Delta_0}{\Delta_1} \right|^{0.20}, \quad (3.9)$$

where  $h_{new}$  is the new timestep size,  $h_{old}$  is the initial timestep size, and  $F$  is used to keep the new timestep small enough to be accepted.

When the timestep is becomes excessively small, the timestep restriction can be due to stability issues caused by numerical stiffness [38]. The integration method is then switched to the first-order accurate, unconditionally stable, backward Euler method,

$$\tau_{n+1}^{(\alpha)} = \tau_n^{(\alpha)} + hf\left(\tau_{n+1}^{(\alpha)}, t_{n+1}\right), \quad (3.10)$$

which is solved using quasi-Newton iteration.

### 3.2.3 Finite Element Representation of Thermal Conduction

Temperatures are obtained from the discretized finite element heat conduction equation,

$$[C]\{\dot{T}\} + [K]\{T\} = \{R_T\}, \quad (3.11)$$

where  $[C]$  is the matrix of coefficients proportional to temperature rate of change,  $\{\dot{T}\}$  is the vector of change in nodal temperatures,  $[K]$  is a matrix of coefficients proportional to temperature,  $\{T\}$  is the vector of nodal temperatures, and  $\{R_T\}$  is the vector of nodal input heat sources for mechanical, decomposition, and laser energies. The elemental matrices of these quantities are given by

$$[C_{ele}] = \int [N^T][N] \rho c_p dV, \quad (3.12)$$

$$[K_{ele}] = \int [B^T][\kappa][B] dV, \quad (3.13)$$

$$[R_{ele}] = \int [N^T] Q dV, \quad (3.14)$$

where  $[N]$  is the vector of shape functions,  $[B]$  is the strain-displacement matrix, and  $[\kappa]$  is the matrix of thermal conductivities. The elemental heat generation rate,  $Q$ , is the sum of heat generation sources within the element obtained from Equations (2.26) and (2.29 – 2.31).

The time-varying temperature histories are obtained by direct time integration of Equation (2.32) as follows

$$\left(\frac{1}{\Delta t} [C] + \beta [K]\right) \{T\}_{n+1} = \left(\frac{1}{\Delta t} [C] + \beta [K]\right) \{T\}_n + (1 - \beta) \{R_T\}_n + \beta \{R_T\}_{n+1}, \quad (3.15)$$

where the parameter  $\beta = 0.5$  for Crank-Nicholson (trapezoidal rule) integration is used.



## **CHAPTER 4: Laser Interaction Effects of EM Absorption and Microstructural Defects on Hot-Spot Formation in RDX-PCTFE Energetic Aggregates**

### **4.1 Introduction**

It is necessary to understand the effects of microstructure on the response of energetic aggregates to incident laser energy, thermal, and mechanical loads, and to identify the mechanisms that contribute to hot spot formation and possible detonations. The complex microstructure of these materials, in conjunction with their mechanical, chemical, and electrical properties, greatly affects their sensitivity to detonation due to the interrelated effects of high mechanical pressures, temperatures, and electromagnetic energy.

Hence, the main objective of this study is to investigate and understand the coupled effects of microstructural crystal-binder interactions, dislocation-density evolution, void distributions and material electromagnetic absorption properties on the thermo-mechanical response and hot spot formation mechanisms in energetic aggregates subjected to simultaneous laser energy and dynamic pressure loads. The effects of electromagnetic absorption coefficient coupled with void distribution and spacing, grain morphology, crystal-binder interactions, and dislocation densities were analyzed to determine their influence on the time, location, and mechanisms of hot spot formation.

### **4.2 Results**

The RDX energetic aggregate was represented by a 1mm x 1mm model consisting of 25 RDX crystals with average size of 200  $\mu\text{m}$  dispersed inside a PCTFE polymeric binder material (Figure 4.1). The morphology of the crystals was generated using a Voronoi tessellation algorithm, and their misorientations at the grain boundaries vary randomly

between -15° and +15°. Material properties of the RDX crystals are given by Armstrong and Elban [9] and Annapragada et al. [15], and are shown in Table 4.1. Experimental data reported by Miller [52] indicates that the melting point of RDX increases linearly under an applied pressure load. However, thermal decomposition was also observed at temperatures below this elevated melting point for a given pressure, which is consistent with the predictions indicating that thermal decomposition will occur for the range of pressure loading conditions used in the study.

**Table 4.1: Material Properties of RDX and PCTFE Binder**

	RDX	PCTFE Binder
Density ( $\frac{kg}{m^3}$ )	1820	2158
Yield Stress (MPa)	580	--
Elastic Modulus (GPa)	18.4	3.66
Poisson Ratio	0.22	0.39
Thermal Conductivity ( $\frac{W}{m K}$ )	0.29	0.142
Specific Heat ( $c_p$ ) ( $\frac{J}{kg K}$ )	1260	1260

The crystals are modeled with the following three slip systems: (010) [001], (021) [100], (02  $\bar{1}$ ) [100] as shown in Gallagher *et al.* [10], and orientations specific to RDX are used to obtain the slip system interaction coefficients used in Equation (2.9). RDX crystals often contain voids, which result due to crystal processing parameters, and can exist in a variety of sizes, distributions, and overall porosity volume fractions [22,53]. For this study, the volume fraction of internal voids was assumed as 2.8%, and both a random distribution and a periodic distribution of these voids were investigated.

The PCTFE binder is randomly dispersed between the grains with a 10% volume fraction of the total aggregate. Thermal conductivity for the binder was taken from measurements given in Kline and Hansen [54], and its specific heat capacity was set equal to that used for RDX based on values reported for a 90% RDX / 10% Kel-F aggregate by Baytos [55]. Its mechanical properties are based on measurements by Brown *et al.* [17], and since the glass transition temperature of the PCTFE binder is approximately 50° C [17], it is assumed that the material will be in an elastic rubbery stage for the dynamic loading conditions used in this investigation. Consequently, it is modeled as a hypo-elastic material based on the first term of Equation (2.6).

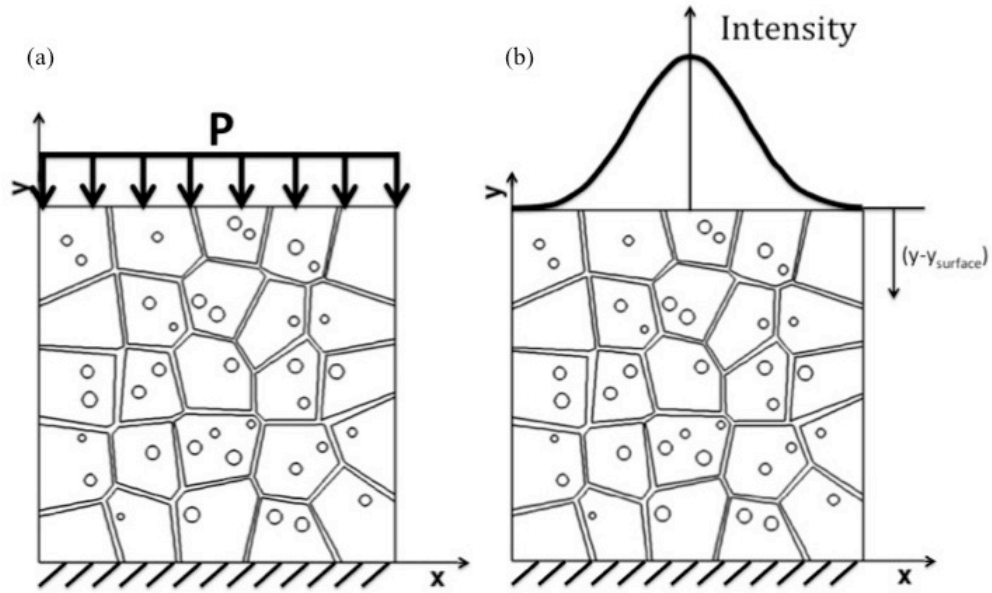


**Figure 4.1: The RDX-polymer aggregate with boundary conditions and loading from (a) Compressive pressure load, and (b) Incident laser intensity. The loading conditions are shown separately for clarity, but were applied to the model simultaneously.**

Two-dimensional plane strain conditions were used with a constant 750 MPa dynamic compressive pressure load applied at the top surface and held constant for the

duration of the time history (Figure 4.1(a)). Boundary conditions are shown in Figure 4.1, with the top and both sides of the model free to deform and a fixed condition on the lower surface. Simultaneously, laser energy was applied as a Gaussian beam with a peak intensity of  $1 \times 10^7 \text{ W/cm}^2$  centered at the location (0.5, 1.0) mm and with a radius of 0.2 mm (Figure 4.1(b)). For this study, the electric field intensity was specified as a function of depth below the material surface ( $y_{\text{surface}} - y$ ) and material absorption coefficient,  $\alpha$ , following a Beer-Lambert absorption relation given by

$$I(x, y) = I_0(x) e^{-\alpha(y_{\text{surface}} - y)}, \quad (4.1)$$

where  $I_0(x)$  is the intensity profile just inside the material surface after any surface reflections have occurred. This expression is obtained from the solution to the time-harmonic electromagnetic wave equation for a wave propagating through a perfect dielectric material in the y-direction, with its electric field polarized in the out-of-plane z-direction [56]. For a Gaussian beam, which is the fundamental operation mode for many lasers, the surface intensity distribution is given by

$$I_0(x) = I_{\text{max}} e^{\frac{-(x-\mu)^2}{r^2}}, \quad (4.2)$$

where  $I_{\text{max}}$  is the peak intensity at the center of the beam,  $\mu$  is the global x-coordinate at the beam center, and  $r$  is the Gaussian beam radius.

We assumed laser energy wavelengths that varied between 10.0 – 10.6  $\mu\text{m}$ , which can be generated by an infrared  $\text{CO}_2$  laser. For this wavelength range, the optical properties of RDX and binder materials have been measured by Isbell and Brewster [57], and there is a wide variation in the RDX absorption coefficient between approximately  $\alpha = 0 \text{ cm}^{-1}$  at wavelength 10.0  $\mu\text{m}$  and  $\alpha = 2800 \text{ cm}^{-1}$  at wavelength 10.6  $\mu\text{m}$  while the binder absorption

coefficient remains relatively constant at  $\alpha = 361 \text{ cm}^{-1}$  for this range of wavelengths.

Consequently, we investigated three different cases with RDX absorption coefficients of  $\alpha = 10 \text{ cm}^{-1}$ ,  $\alpha = 100 \text{ cm}^{-1}$ , and  $\alpha = 1,000 \text{ cm}^{-1}$ , and we assumed a constant value of  $\alpha = 361 \text{ cm}^{-1}$  for the binder absorption coefficient for all cases.

#### ***4.2.1 Low RDX Absorption Coefficient ( $\alpha = 10 \text{ cm}^{-1}$ ) and Random Void Distribution***

For the case of low RDX absorption with a coefficient of  $\alpha = 10 \text{ cm}^{-1}$  and a random void distribution, the spatial temperature distribution, which includes the interrelated effects of heat conduction, decomposition, plastic work heating and laser heating, is shown at a time of  $0.632 \text{ }\mu\text{s}$  after the initial application of thermal and structural loading in Figure 4.2(a). The temperatures are normalized by the initial temperature of 293 K. It can be seen that a large region throughout the center of the model had temperatures that are 1.1 times the initial temperature, while much higher temperatures, up to 2.2 times the initial temperature, are localized around the binder regions at the surface near the center of the applied laser source ( $x = 0.5 \text{ mm}$ ) and scattered throughout the material in local areas near the voids.

The normalized temperature increase due solely to the laser heating is shown in Figure 4.2(b), and it can be seen that the laser heating is the main mechanism affecting the high temperatures generated in the binder at the surface, and also for the general low temperature increase in the RDX crystals. This thermal distribution is due to the absorption properties of both the binder and the RDX crystals. For the RDX crystals, which have a low absorption coefficient ( $\alpha = 10 \text{ cm}^{-1}$ ), most of the laser energy passes through the material, and only a small percentage is absorbed and converted into heat. The binder has a higher absorption coefficient ( $\alpha = 361 \text{ cm}^{-1}$ ), such that more of the laser energy is absorbed by the

binder material at the top surface with temperatures that were 2.2 times the original temperature.

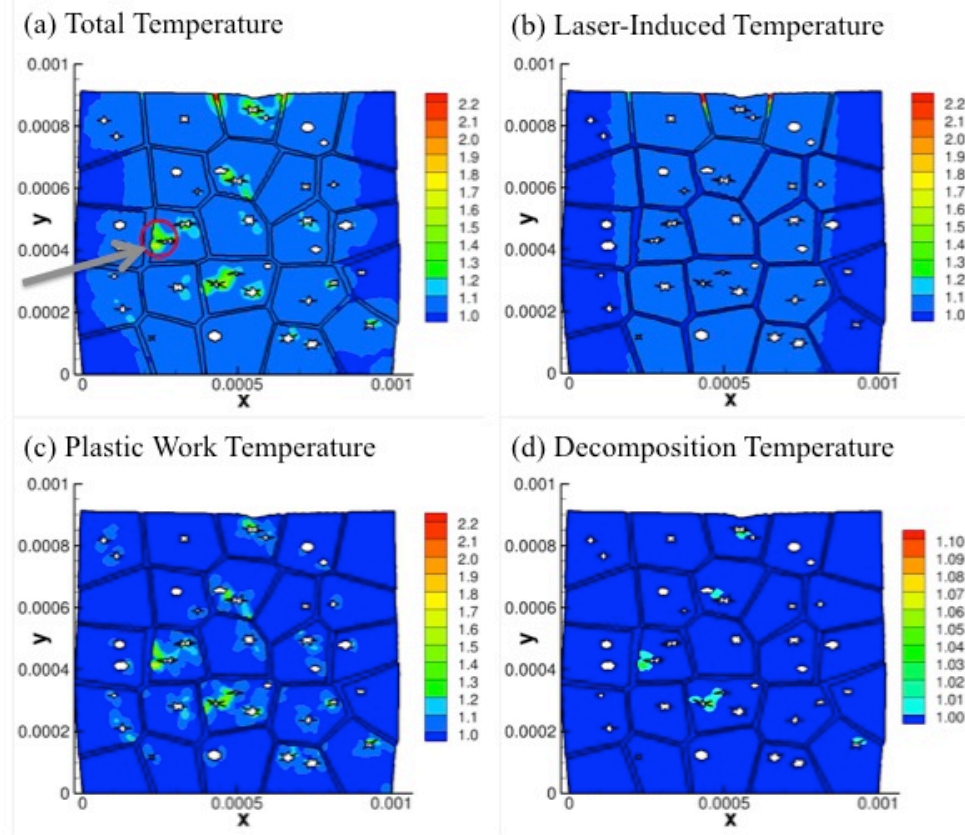


**Figure 4.2:** Temperature components for random void distribution and RDX absorption coefficient  $\alpha = 10 \text{ cm}^{-1}$ , normalized by the initial temperature of 293 K and shown at  $0.632 \text{ } \mu\text{s}$ . (a) Total temperature increase including effects from conduction, laser-heating, decomposition, and plastic work heating, (b) Laser-induced temperature increase, (c) Plastic work induced temperature increase, (d) Temperature increase due to thermal decomposition of RDX.

This result is consistent with the nominal absorption depth for the two materials, which is calculated (based on Equations (4.1) and (4.3)) as  $1/\alpha$  from the one-dimensional analytical solution for laser-induced heating in a homogeneous material given as

$$T(y, t) = T_{initial} + (t) \frac{1}{\rho c_p} I_0 \alpha e^{-\alpha(y_{surface}-y)} \quad (4.3)$$

The absorption depth describes the distance from the material top surface at which the propagating electromagnetic wave is reduced to 33% of its original intensity, or alternatively

the depth at which 67% of the laser energy has been absorbed within the material as heat. For RDX crystals with an absorption coefficient of  $\alpha = 10 \text{ cm}^{-1}$ , the calculated absorption depth is equal to 1 mm. This indicates that at the bottom edge of the model (1 mm from the top surface), only 67% of the energy from the laser has been absorbed within the RDX crystals. The binder, by contrast, has a much shorter absorption depth of 0.028 mm, indicating that 67% of the laser energy applied on the binder is absorbed and converted to heat close to the top surface, and that the binder material within the bulk of the model will be exposed to little of the laser energy. This behavior can be clearly seen in Figure 4.2(a-b).

The temperature increases mainly due to plastic work are localized at regions surrounding the voids (Figure 4.2(c)), and it can be seen that this is the dominant contribution to local temperature buildup within the material. Heating due to decomposition also occurs at some of the inter-void regions that experience plastic work heating (Figure 4.2(d)), although the contributions from decomposition at this time (0.632  $\mu\text{s}$ ) are less than 1.1 times the original temperature indicating that the decomposition process is in its early stages.

Figure 4.3 shows the distribution of normal stress, accumulated plastic shear strain, and immobile and mobile dislocation densities on the most active slip system (010) [001] at a time of 0.632  $\mu\text{s}$ . At this time, the initial pressure wave has propagated throughout the domain and the normal stress, shown normalized by the static yield stress of RDX, was generally compressive throughout the bulk of the material with some localized tensile regions at the peripheries of the voids (Figure 4.3(a)). The accumulated plastic shear strain (Figure 4.3(b)) is highly localized in regions where two voids are located close together, or where a void is near the binder. The immobile (Figure 4.3(c)) and mobile (Figure 4.3(d)) dislocation

densities (normalized by the initial dislocation densities), which correspond to the most active slip system (010) [001], show that dislocation density activity is concentrated in regions of high plastic shear strain around the voids. This accumulation of plasticity in the inter-void regions is directly linked to the temperature increase seen in these areas as heat is dissipated due to the plastic work (Figure 4.2(a, d)).

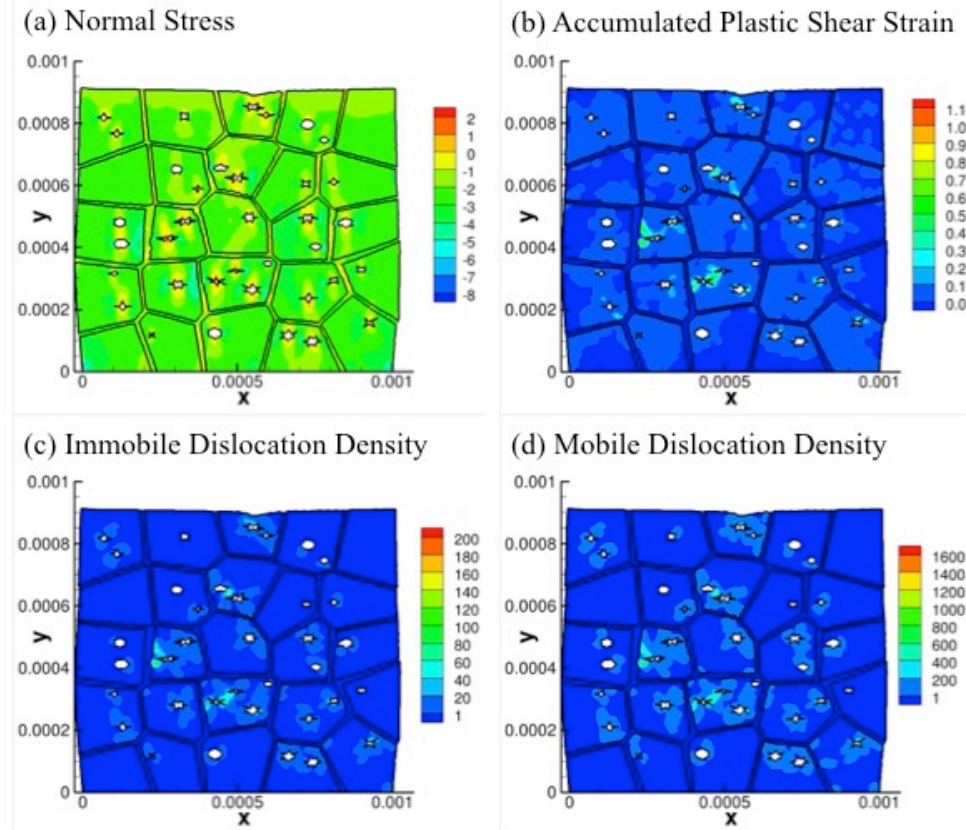


**Figure 4.3:** (a) Normal stress (normalized by static yield stress), (b) Accumulated plastic shear strain, (c) Immobile and (d) Mobile dislocation densities from the most active slip system (010)[001] (normalized by the initial value) for random void distribution and low RDX absorption coefficient  $\alpha = 10 \text{ cm}^{-1}$  at a time of  $0.632 \text{ } \mu\text{s}$ .

The coupled effects of applied pressure loads and incident laser energy are further illustrated by considering the temperature increase and the plastic shear strain along a vertical line extending through the model (Figure 4.4). The predicted temperatures are significantly higher at several locations than those calculated by the analytical 1-D solution for



homogeneous RDX (Equation (4.3)) due to the thermo-mechanical coupling and microstructural interactions.

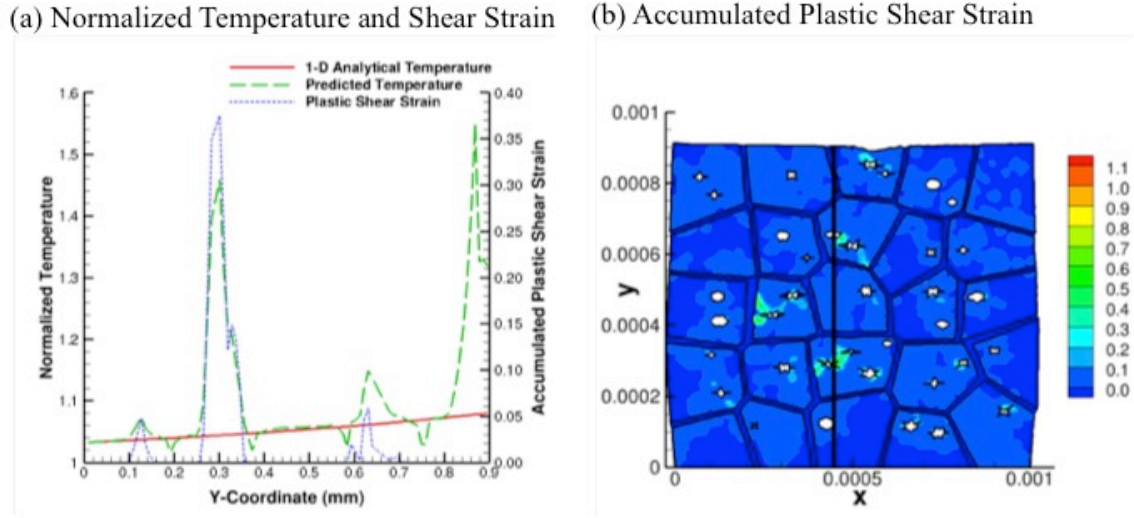


**Figure 4.4:** (a) Predicted temperature, 1-D analytical solution for laser-generated temperature (Equation (4.3)), and plastic shear strain along the vertical line taken from (b) for RDX absorption coefficient  $\alpha = 10 \text{ cm}^{-1}$  with random void distribution. All temperatures are normalized by the initial temperature of 293 K.

The initial temperature increase at  $y = 0.9 \text{ mm}$  is due to heat conduction from the nearby binder, which undergoes significant heating at the top surface due to its higher absorption properties. At depths further within the model, the predicted solution temperature is higher than the 1-D analytical solution in areas with plastic shear strain accumulation ( $y = 0.65 \text{ mm}$ ,  $y = 0.3 \text{ mm}$ , and  $y = 0.15 \text{ mm}$ ) due to the additional heat generation in these areas from plastic work. At the binder regions, a slightly lower temperature than the 1-D analytical solution is predicted due to the difference in absorption properties between these two materials. However, in areas where pure RDX is present without voids, such as the central grain between  $y = 0.4 \text{ mm}$  and  $y = 0.6 \text{ mm}$ , the predicted temperature matches well with the analytical solution.

These localized temperature build-ups are of significant interest, since hot spots can form within energetic materials when the heat generated in a localized area exceeds the heat dissipated to the surrounding material [27,58]. The rapid temperature increase is due largely to the Arrhenius exponential rate of heat generated by the thermal decomposition mechanism (Equation (2.30)), and such unbounded temperature build up in a localized area can indicate hot spot formation as shown by LaBarbera and Zikry [59]. In this case with low RDX absorption ( $\alpha = 10 \text{ cm}^{-1}$ ) and a random void distribution, a hot spot forms in the circled region of Figure 4.2(a) at a time of 0.635  $\mu\text{s}$ . The initial heat generation mechanism in this area is plastic work heating due to the high shear strain accumulation, which then leads to thermal decomposition that quickly causes an unbounded temperature to develop. The laser-induced temperature increase in this region is small (Figure 4.2(b)), so in this case laser heating was not a major contributor in forming the initial hot spot. These results clearly delineate the mechanisms for hot spot generation due to plastic work heating that triggers decomposition in regions that experience high plastic shear strains, which is consistent with LaBarbera and Zikry [59].

#### ***4.2.2 Intermediate RDX Absorption ( $\alpha = 100 \text{ cm}^{-1}$ ) and Random Void Distribution***

For an intermediate absorption coefficient in the RDX crystals of  $\alpha = 100 \text{ cm}^{-1}$  and a random void distribution, the total normalized temperature increase at a time of 0.416  $\mu\text{s}$  is shown in Figure 4.5(a). Similar to the low absorption ( $\alpha = 10 \text{ cm}^{-1}$ ) case, the peak temperature increases of 2.2 times the initial temperature occur at the surface in the binder material, but the temperature of the uppermost RDX crystals has also significantly increased.

The denoted circled area at the edge of the uppermost void indicates a region with unbounded temperature increase, which is indicative of hot spot formation, at  $0.420 \mu\text{s}$ .

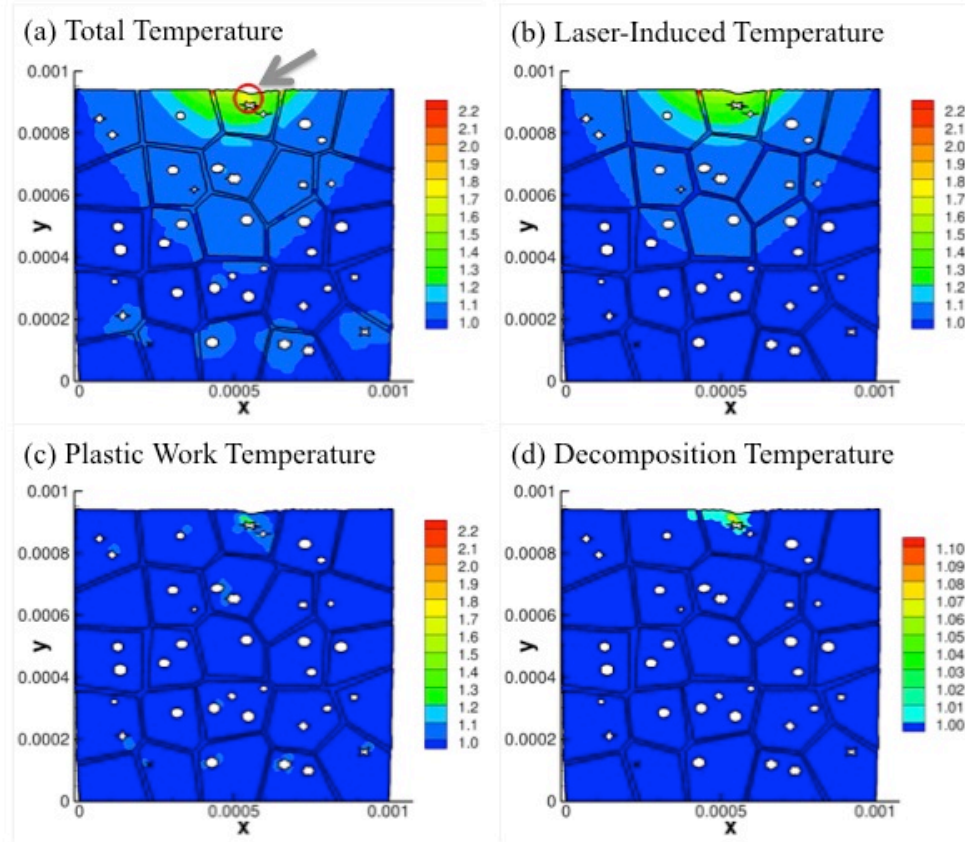


**Figure 4.5: Temperature components for random void distribution and RDX absorption coefficient  $\alpha = 100 \text{ cm}^{-1}$ , normalized by the initial temperature of 293 K and shown at a time of  $0.416 \mu\text{s}$ . (a) Total temperature increase including effects from conduction, laser-heating, decomposition, and plastic work heating, (b) Laser-induced temperature increase, (c) Plastic work induced temperature increase, (d) Temperature increase due to thermal decomposition of RDX.**

The laser-induced temperature increase is shown in Figure 4.5(b), and it can be seen that laser heating is the main mechanism that affects thermal increases throughout the RDX crystals near the top surface. Significant temperature increases between 1.2 and 1.6 times the initial value occur within the Gaussian beam diameter and at depths above 0.5 mm from the top surface. This indicates that most of the laser energy is absorbed and converted to heat

within the top surface grains, and this is consistent with the nominal absorption depth for homogeneous RDX at this value of  $\alpha$ , which is calculated to be 0.1 mm based on the 1-D analytical solution (Equation (4.3)).

The temperature increase due to plastic work heating is localized at areas between neighboring voids (Figure 4.5(c)) with its maximum value occurring at the void closest to the top surface in the area that experiences an unbounded temperature. At this location, temperature increases due to thermal decomposition within the RDX crystal (Figure 4.5(d)) occurred, and this contributed to hot spot formation.

At 0.416  $\mu$ s, just before the hot spot develops, the distributions of normal stress, plastic shear strain, and the immobile and mobile dislocation densities on the most active slip system (010) [001] are shown in Figure 4.6. Similar to the low absorption case with  $\alpha = 10 \text{ cm}^{-1}$ , the normal stress is generally compressive throughout the entire model (Figure 4.6(a)), with several tensile regions near the peripheries of the voids and within the elastic binder. The plastic shear strain accumulation (Figure 4.6(b)) and both the immobile and mobile dislocation density buildups (Figure 4.6(c-d)) are concentrated at areas between voids, and the maximum values for all these quantities are less than those seen in the previous case (Figure 4.3(b-d)).

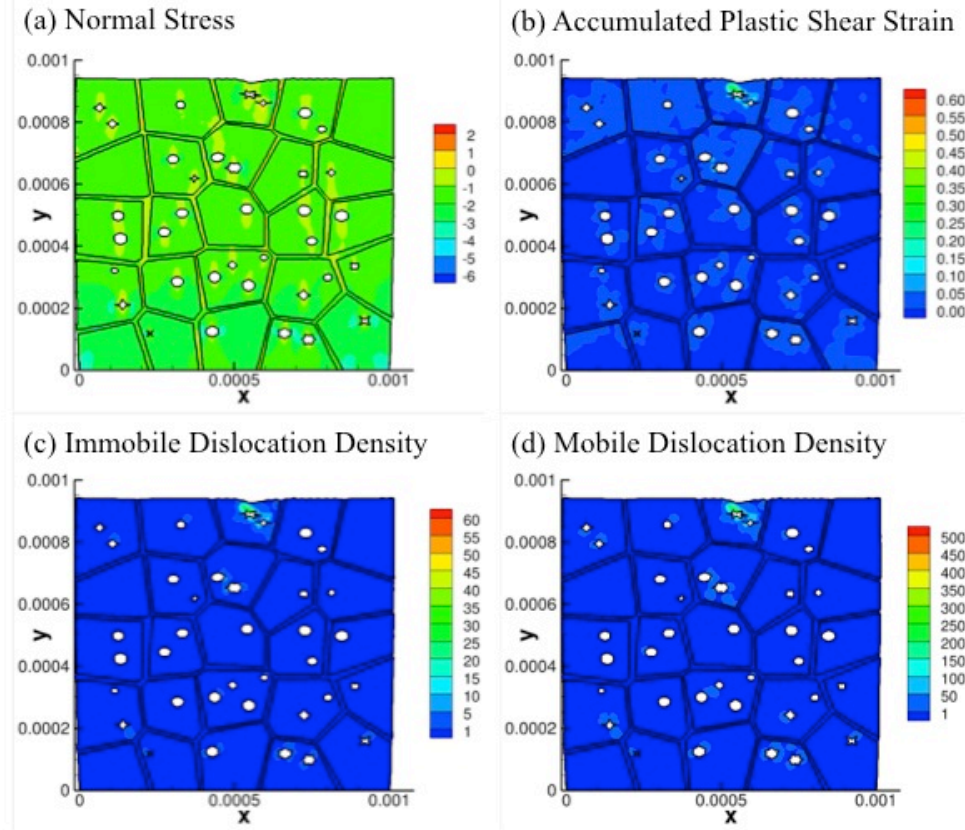


**Figure 4.6:** (a) Normal stress (normalized by static yield stress), (b) Accumulated plastic shear strain, (c) Immobile and (d) Mobile dislocation densities from the most active slip system (010)[001] (normalized by the initial value) for random void distribution and RDX absorption coefficient  $\alpha = 100 \text{ cm}^{-1}$  at a time of  $0.416 \text{ } \mu\text{s}$ .

For the case with low RDX absorption coefficient ( $\alpha = 10 \text{ cm}^{-1}$ ), laser heating was not a major contributor in hot spot initiation, which allowed more time for additional plasticity to develop that eventually caused hot spot formation at  $0.635 \text{ } \mu\text{s}$ . For the intermediate RDX absorption coefficient of  $\alpha = 100 \text{ cm}^{-1}$ , significant temperature increases occurred due to the laser localizing in an area that also had substantial shear strain localization and plastic work heating. The combination of these two heat generation sources increased the temperature, such that the thermal decomposition and unbounded temperature occurred at an earlier time than the  $\alpha = 10 \text{ cm}^{-1}$  case.

A comparison of the two cases at the same time of  $0.416 \mu\text{s}$  (Figure 4.7) shows that both cases have localized plasticity in the same areas, but at this time the maximum value of plastic shear strain is 0.44 for the low absorption coefficient  $\alpha = 10 \text{ cm}^{-1}$  (Figure 4.7(a)), while for the intermediate absorption coefficient  $\alpha = 100 \text{ cm}^{-1}$  the maximum plastic shear strain is 0.60 (Figure 4.7(b)).

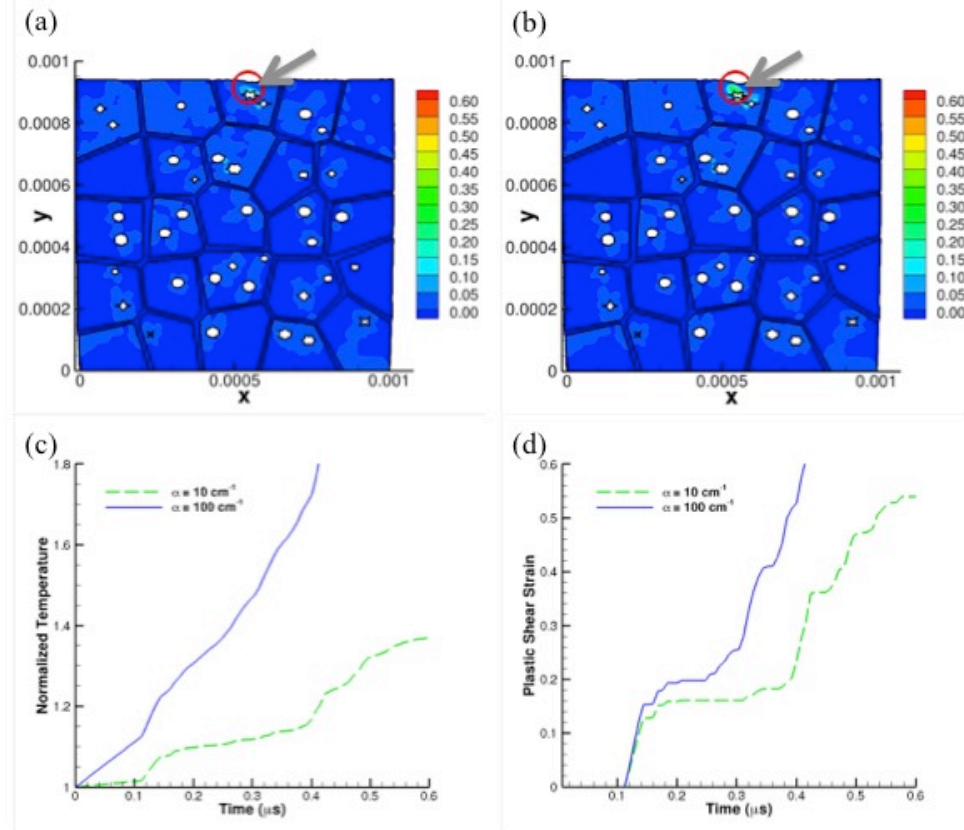


**Figure 4.7:** (a) Plastic shear strain distribution at time  $0.416 \mu\text{s}$  for low RDX absorption coefficient  $\alpha = 10 \text{ cm}^{-1}$  and random voids, (b) Plastic shear strain distribution at time  $0.416 \mu\text{s}$  for intermediate RDX absorption coefficient  $\alpha = 100 \text{ cm}^{-1}$  and random voids, (c) Normalized temperature-time history for an element within the circled region, (d) Plastic shear strain-time history for an element within the circled region. The same element is used for both low and intermediate absorption cases.

These differences can be attributed to the significant temperature increases seen in the uppermost grains due to the higher absorption of laser energy in this region when the absorption coefficient is an intermediate value of  $\alpha = 100 \text{ cm}^{-1}$  (Figure 4.5(a)). The increased

temperature facilitates more plastic shear strain accumulation in this region through thermal softening mechanisms, which reduces the reference shear stress that must be exceeded in order for plastic shear slip to occur (Equation (2.9)). In addition, higher temperatures result in a faster annihilation rate for the immobile dislocation densities due to the recovery process, which also contributes to the increase seen in plastic shear strain.

The relation between temperature and plastic shear strain can be further illustrated by considering the temperature (Figure 4.7(c)) and simultaneous plastic shear strain (Figure 4.7(d)) accumulation over time in the circled region of Figure 4.7(a-b). For the intermediate absorption coefficient  $\alpha = 100 \text{ cm}^{-1}$ , this region is at a consistently higher temperature than for the low absorption coefficient  $\alpha = 10 \text{ cm}^{-1}$ , due to more laser energy being absorbed and converted to heat in the uppermost grains. This corresponds to the larger amounts of plastic shear strain that accumulate more quickly for the intermediate absorption coefficient (Figure 4.7(d)). Consequently, it can be seen that the material's propensity to undergo plastic deformation is increased in regions that have significant absorption of laser energy, which can in turn affect the location and time of potential hot spot nucleation sites.

#### ***4.2.3 High RDX Absorption ( $\alpha = 1000 \text{ cm}^{-1}$ ) and Random Void Distribution***

For a random void distribution with high RDX absorption coefficient of  $\alpha = 1,000 \text{ cm}^{-1}$ , the temperature increase was significant within a thin layer at the top surface (Figure 4.8(a)) at a time of  $0.096 \text{ }\mu\text{s}$ . The circled area indicates a site of unbounded temperature increase at the top surface of the center RDX crystal at  $0.103 \text{ }\mu\text{s}$ . In this case, the laser energy is absorbed and converted to heat within a thin layer close to the top material surface, which results in a high temperature increase in this area and no temperature increase below



depths of 0.1 mm (Figure 4.8(b)). The calculated absorption depth, based on the one-dimensional analytical solution, for this value of  $\alpha = 1,000 \text{ cm}^{-1}$  is 10  $\mu\text{m}$ , which is comparable to the area with the highest temperature increases seen in Figure 4.8(a-b). In contrast to the two previous cases, the high absorption coefficient of RDX ( $\alpha = 1,000 \text{ cm}^{-1}$ ) is much greater than that of the binder ( $\alpha = 361 \text{ cm}^{-1}$ ), so after only 0.096  $\mu\text{s}$  the laser energy absorbed by the RDX crystals is much greater than that absorbed by the binder.

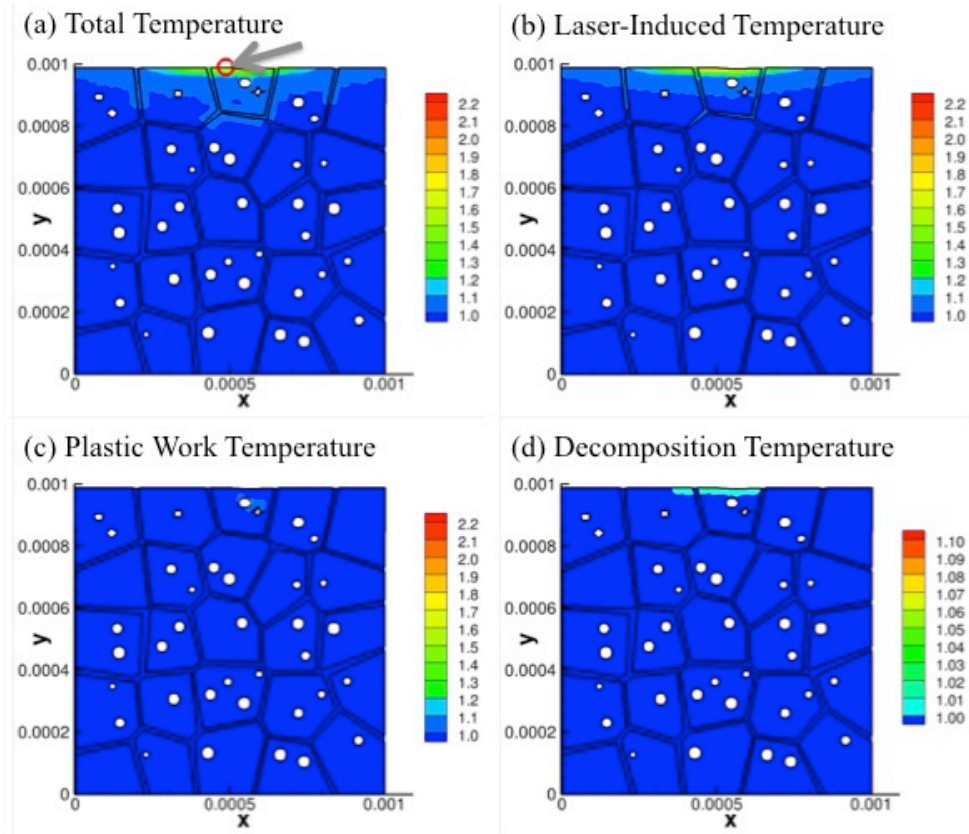


**Figure 4.8:** Temperature components for random void distribution and RDX absorption coefficient  $\alpha = 1,000 \text{ cm}^{-1}$ , normalized by the initial temperature of 293 K and shown at a time of 0.096  $\mu\text{s}$ . (a) Total temperature increase including effects from conduction, laser-heating, decomposition, and plastic work heating, (b) Laser-induced temperature increase, (c) Plastic work induced temperature increase, (d) Temperature increase due to thermal decomposition of RDX.



For this case, at the time that an unbounded temperature increase occurs, heating due to plastic work has only developed in one location (Figure 4.8(c)), and its magnitude is relatively small compared to the temperatures generated by the laser. Plastic work heating also occurs at a location different from that where the unbounded temperature develops, indicating that this mechanism does not contribute to the hot spot formation. At this time, a temperature increase due to decomposition has also occurred (Figure 4.8(d)), and its location does correspond to the site of unbounded temperature increase. It is clear from Figure 4.8(a-d) that for the case of high RDX absorption coefficient  $\alpha = 1,000 \text{ cm}^{-1}$ , hot spot initiation is governed entirely by the fast laser heating that occurs in the top surface layers of the material, which leads to unbounded thermal decomposition, and hot spot formation.

Since a hot spot develops so quickly at this high absorption coefficient, the compressive pressure wave has not yet propagated the entire length of the model, and a clear wave front is visible in the normal stress levels (Figure 4.9(a)). This also explains the much lower levels of plastic shear strain (Figure 4.9(b)) and immobile and mobile dislocation densities for the most active slip system (010) [001] shown in Figure 4.9(c-d), respectively. Since plasticity can only develop in areas that have been subjected to the compressive wave, the only dislocation density activity and plastic strain present at this time is seen for the two voids near the top surface.

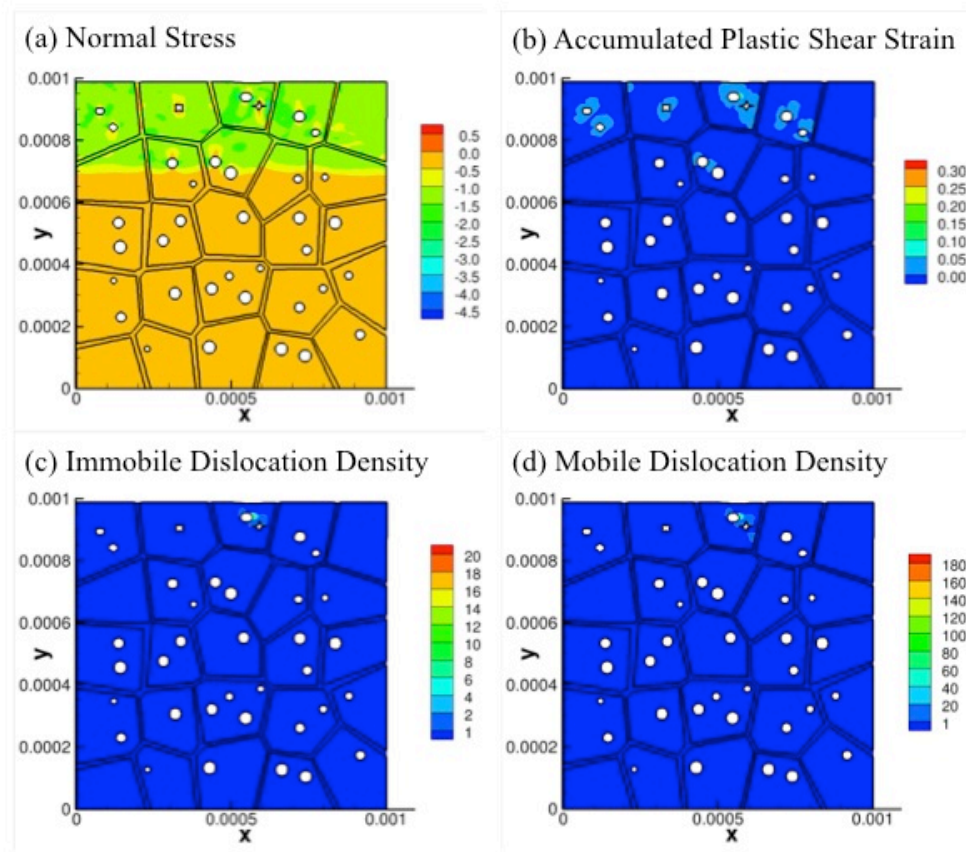


**Figure 4.9:** (a) Normal stress (normalized by static yield stress), (b) Accumulated plastic shear strain, (c) Immobile and (d) Mobile dislocation densities from the most active slip system (010)[001] (normalized by the initial value) for random void distribution and RDX absorption coefficient  $\alpha = 1,000 \text{ cm}^{-1}$  at a time of  $0.096 \text{ }\mu\text{s}$ .

#### ***4.2.4 Periodic Void Distributions and Intermediate RDX Absorption ( $\alpha = 100 \text{ cm}^{-1}$ )***

For a case with periodic voids and intermediate RDX absorption coefficient ( $\alpha=100\text{cm}^{-1}$ ), the normalized temperature profile at  $0.488 \text{ }\mu\text{s}$  is shown in Figure 4.10(a). The maximum temperature increase of 2.2 times the initial temperature occurs in the binder at the surface, but grains within the nominal diameter of the laser beam are also heated in the upper portion of the model and a temperature increase also occurs at the peripheries of some of the

voids. An unbounded temperature increase occurred after  $0.492 \mu\text{s}$  within the circled region of RDX immediately adjacent to the binder (Figure 4.10(a)).

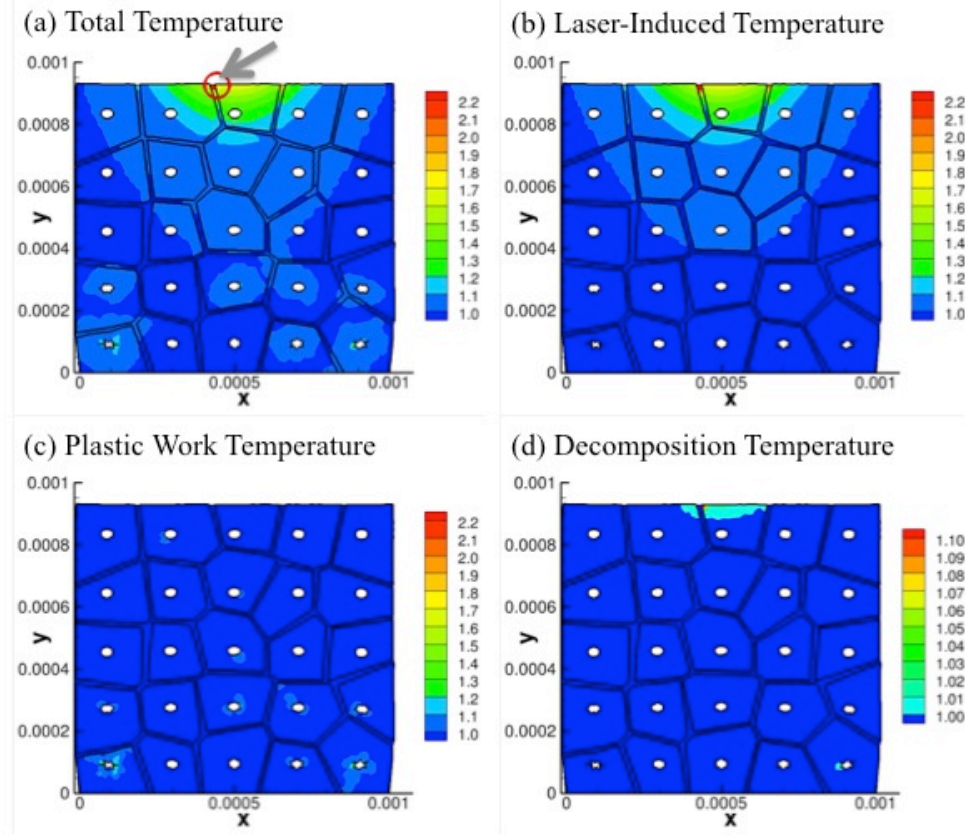


**Figure 4.10: Temperature components for periodic void distribution and RDX absorption coefficient  $\alpha = 100 \text{ cm}^{-1}$ , normalized by the initial temperature of 293 K and shown at a time of  $0.488 \mu\text{s}$ . (a) Total temperature increase including effects from conduction, laser-heating, decomposition, and plastic work heating, (b) Laser-induced temperature increase, (c) Plastic work induced temperature increase, (d) Temperature increase due to thermal decomposition of RDX.**

The temperature increase due to laser heating is shown in Figure 4.10(b), and it is almost identical to the laser induced temperature for the intermediate RDX absorption case with random voids (Figure 4.5(b)). This results from both cases having the same absorption coefficient of  $\alpha = 100 \text{ cm}^{-1}$  in the RDX crystals, which is the primary factor that affects the location and magnitude of the laser-induced heating. The temperature generated by plastic work heating is concentrated largely around the two voids in the lower corners, as shown in

Figure 4.10(c), while temperature increase due to decomposition is present in the area of RDX crystals adjacent to the binder where the hot spot forms (Figure 4.10(d)).

The normal stress distribution (Figure 4.11(a)) is generally compressive and similar to the results for the random void configurations at comparable times (Figure 4.6(a)). The plastic shear strain is largely concentrated around the two voids in the lower corners, and very little accumulation is seen anywhere else in the model (Figure 4.11(b)). The immobile dislocation densities (Figure 4.11(c)) and mobile dislocation densities (Figure 4.11(d)) on the most active slip system (010) [001] are also concentrated around these two voids.

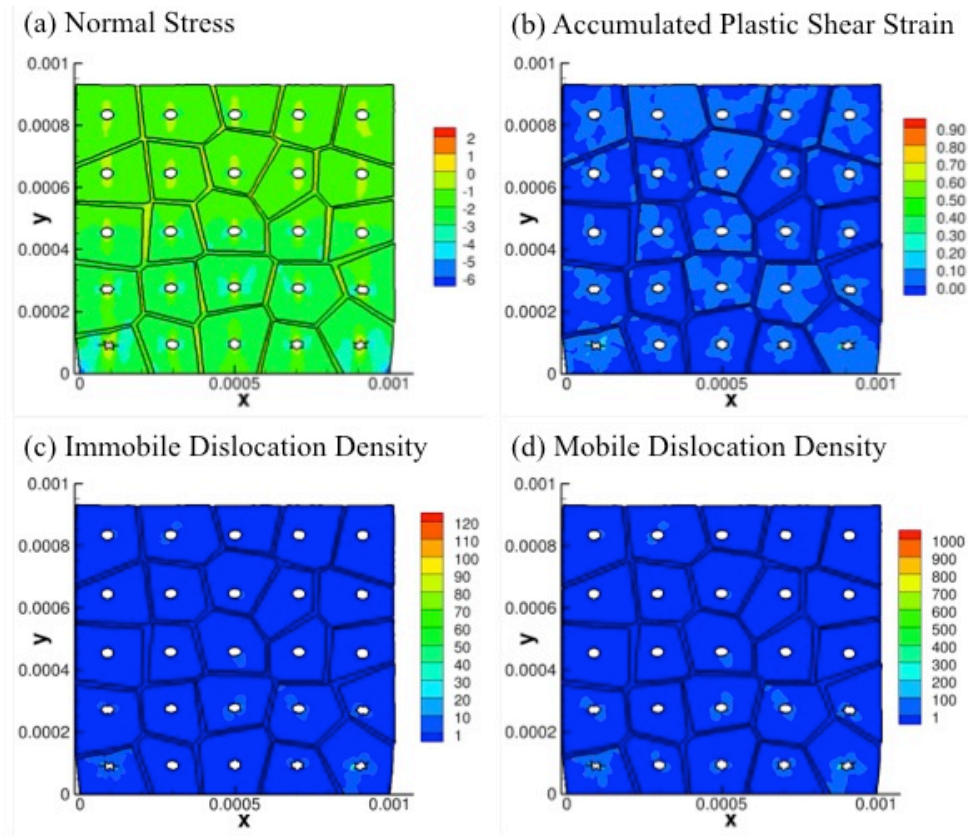


**Figure 4.11: (a) Normal stress (normalized by static yield stress), (b) Accumulated plastic shear strain, (c) Immobile and (d) Mobile dislocation densities from the most active slip system (010)[001] (normalized by the initial value) for periodic void distribution and RDX absorption coefficient  $\alpha = 100 \text{ cm}^{-1}$  at a time of  $0.488 \text{ } \mu\text{s}$ .**

This is in contrast to the cases with a random void distribution, where plastic shear strain occurred with comparable magnitudes at many locations within the model. The difference can be largely attributed to the void distribution and spacing. In cases with a random void distribution, the greatest plasticity developed in areas where two or more voids were spaced closely together or where a void was positioned close to the binder (Figure 4.3(b), Figure 4.6(b)). With periodic void spacing, the voids are evenly spaced close to the center of the RDX crystals, and the interaction between voids that facilitates the additional dislocation activity and shear slip does not occur. The large amount of plasticity that develops around the voids in the lower corner grains for this periodic distribution is most likely a result of higher compressive stresses produced in these grains from the fixed boundary condition applied to the lower surface of the model.

Consequently, for the periodic void distribution and intermediate absorption coefficient  $\alpha = 100 \text{ cm}^{-1}$ , there is no shear slip present within the laser heated area and thus interactions between plastic shear and laser heat absorption do not contribute to hot spot generation. In this case, the hot spot forms in the top-center RDX crystal immediately adjacent to the binder, which is at a higher temperature than the neighboring RDX grains due to its higher absorption coefficient ( $\alpha_{\text{binder}} = 361 \text{ cm}^{-1}$ ). The combination of laser energy absorbed by the RDX with the additional heat conduction from the higher temperature binder caused the decomposition and unbounded temperature to occur in this area. At wavelengths where the absorption coefficient of RDX is higher than that of the binder, however, this mechanism will not occur and surface heating of the RDX will be dominant. It is significant that this mechanism results specifically from the differences in electromagnetic absorption

properties between the RDX and the binder, and that such interfaces are particularly susceptible to laser-induced hot spot formation.

#### 4.2.5 Comparison of Hot Spot Generation Mechanisms

Figure 4.12 shows the normalized temperature-time history for the region where a hot spot develops for each of the four cases discussed previously. It can be seen that the material absorption coefficient and the void configuration greatly affect both the spatial location and the time that the temperature becomes unbounded and subsequently a hot spot forms.

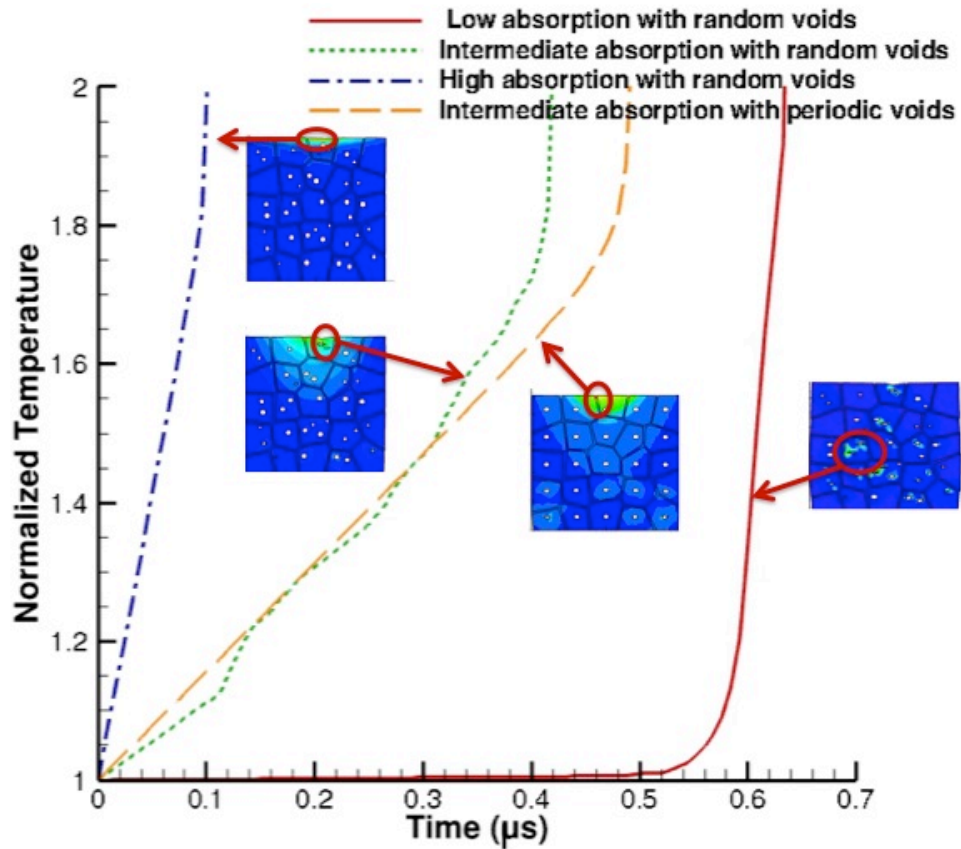


**Figure 4.12:** Temperature-time history normalized by the initial temperature for locations where a hot spot develops.

For the case with low absorption coefficient ( $\alpha = 10 \text{ cm}^{-1}$ ) and random void distribution, the hot spot occurs within the bulk of the material in the region with highest plastic shear strain between a void and the binder. In this case, the initial temperature increase due to the laser energy absorption is negligible, but once local plastic deformation begins at  $0.500 \text{ }\mu\text{s}$ , the temperature increases quickly due to plastic work heating and becomes unbounded at  $0.635 \text{ }\mu\text{s}$ .

With the intermediate absorption coefficient ( $\alpha = 100 \text{ cm}^{-1}$ ) and random voids, the hot spot forms at the top surface of the uppermost void in a region that absorbed a significant amount of laser energy but also had a large amount of plastic shear strain present which contributed additional heat due to plastic work dissipation. The initial linear portion of the temperature increase is due to the laser heat generation, but once the material in this area begins to slip plastically, the temperature increases at a slightly faster rate. This behavior continues until the thermal decomposition reaction begins which causes the temperature to become unbounded and a hot spot forms at  $0.420 \text{ }\mu\text{s}$ . The high absorption coefficient ( $\alpha = 1,000 \text{ cm}^{-1}$ ) with random void distribution case develops a hot spot in the RDX top surface under the laser beam center that experiences a high laser-induced heating rate. The temperature in this region becomes unbounded at  $0.103 \text{ }\mu\text{s}$  as the additional heat generation from thermal decomposition accumulates. At such high RDX absorption coefficient values, it is clear that this mechanism of surface hot-spot generation will occur much faster than the mechanisms observed at lower values of absorption coefficient.

Lastly, the case with intermediate absorption coefficient ( $\alpha = 100 \text{ cm}^{-1}$ ) and periodic voids develops a hot spot in the top-center RDX crystal immediately adjacent to the binder

material. The temperature in this region increases linearly at a rate comparable to the case with the intermediate absorption coefficient ( $\alpha = 100 \text{ cm}^{-1}$ ) and random voids, largely because the hot spots in both these cases form at a similar depth from the material top surface under the same absorption conditions. However, their lateral locations are not the same, and a different mechanism is responsible for the hot spot formation in each case. In the case of periodic voids, the location with unbounded temperature does not undergo any plastic deformation, so its temperature increase remains linear until thermal decomposition begins, resulting in an unbounded temperature at  $0.492 \text{ } \mu\text{s}$ . However, in the case with intermediate absorption and random voids, the location with unbounded temperature shows highly nonlinear temperature increases after approximately  $0.100 \text{ } \mu\text{s}$  due to plastic deformation and the temperature becomes unbounded after a shorter time of  $0.420 \text{ } \mu\text{s}$ . Comparing these two cases, it can be seen that plastic deformation, which occurs in an area of significant laser heating, is an additional heat source that accelerates the hot-spot formation process.

### **4.3 Summary**

The behavior of RDX-PCTFE energetic aggregates due to dynamic pressure loading conditions combined with the simultaneous exposure to incident laser energy has been investigated using a dislocation-density based crystalline plasticity specialized finite-element formulation that accounts for heat conduction, adiabatic heating, thermal decomposition, and laser heating. Four different hot spot generation mechanisms have been identified under these conditions, which are affected by the material electromagnetic absorption properties as well as the presence and spacing of voids within the aggregate.



For a low RDX absorption coefficient of  $\alpha = 10 \text{ cm}^{-1}$  and a random void distribution, only a portion of the incident laser energy was absorbed within the modeled domain, which resulted in a small laser-induced temperature increase throughout the entire depth. The binder material had a large temperature increase at the top surface due to its higher absorption coefficient value of  $\alpha = 361 \text{ cm}^{-1}$ . Plastic shear strain and dislocation densities accumulated in localized areas between two or more voids and also at interfaces between voids and the binder. These areas with high plastic shear strain had an additional temperature increase due to dissipative heating from plastic work. Thermal decomposition occurred at the location of highest plastic shear strain, which was located within the bulk material between a void and the binder, and quickly resulted in an unbounded temperature increase at  $0.635 \text{ } \mu\text{s}$ , which is indicative of hot spot nucleation. Since the laser-induced temperature increase in this region was low, it can be concluded that the laser did not contribute significantly to hot spot formation in this case, and the dominant mechanism responsible for hot spot generation was heating due to plastic shear strain localization.

For the intermediate RDX absorption coefficient of  $\alpha = 100 \text{ cm}^{-1}$  with a random void distribution, most of the laser energy was absorbed within a  $0.1 \text{ mm}$  depth below the model top surface, resulting in a significant temperature increase in the RDX crystals within this region. Plastic shear strain and dislocation activity accumulated in localized areas near the voids. In this case, a hot spot occurred at the edge of the uppermost void due to the combined effects of plastic work heating, laser-induced heating, and thermal decomposition at a time of  $0.420 \text{ } \mu\text{s}$ .

The high RDX absorption coefficient of  $\alpha = 1,000 \text{ cm}^{-1}$  with a random void distribution had a fast laser-induced heating rate at the model top surface, since all the laser energy was absorbed within a depth of several micrometers. A hot spot occurred in the model top surface at  $0.103 \text{ }\mu\text{s}$ , at which time the stress wave had only traversed about half of the model and no significant plasticity had occurred. This indicates that the surface hot spot was generated solely by the laser-induced heating and thermal decomposition mechanisms.

For the intermediate RDX absorption coefficient of  $\alpha = 100 \text{ cm}^{-1}$  with a periodic void distribution, the laser-induced temperature increase was very similar to that seen for the intermediate RDX absorption with random voids, but the plastic shear strain and subsequent heat generation from plastic work occurred in different locations due to the lack of void interactions with other voids and the binder. A hot spot developed in the top-center RDX crystal immediately adjacent to the binder after  $0.492 \text{ }\mu\text{s}$  in a region with no plastic shear strain accumulation. In this case, laser induced heat generation within the RDX crystals combined with heat conduction from the binder resulted in temperature increases necessary for thermal decomposition and hot spot formation.

The material electromagnetic absorption properties and the void distribution significantly affect the time and location of hot spot formation within energetic crystalline aggregates subjected to incident laser energy and compressive pressure loads. In general, as the absorption coefficient increases, the laser-induced heating rate will increase in the grains close to the material surface and hot spots will develop more quickly in these regions, while at low absorption coefficients, more material is subjected to laser-induced heating at a slower rate. Additionally, it is shown that heat generation from plastic work can also facilitate hot

spot formation, and in regions where plastic shear accumulation and laser heating occur simultaneously this process is accelerated. This indicates that under certain incident laser and pressure loads, energetic material aggregates are susceptible to several different hot spot formation mechanisms, and the response is governed by the coupled effects of material electromagnetic absorption properties and microstructural features.

## **CHAPTER 5: Coupled Infrared Laser-Thermo-Mechanical Response of RDX-PCTFE Energetic Aggregates**

### **5.1 Introduction**

The response of materials to incident electromagnetic (EM) fields is of interest in a variety of applications, including laser processing of materials, electromagnetic metal forming, and for the electromagnetic shielding of sensitive components. Hot spot formation, and potential deflagration and/or detonations present safety hazards present during laser irradiation of energetic materials. A fundamental understanding of energetic aggregates under such conditions is, therefore, necessary to accurately predict their response for coupled laser-thermo-mechanical loading conditions and applications.

We use the computational approach presented in Section 3.1 to investigate the response of RDX-PCTFE energetic aggregates to laser irradiation at wavelengths where RDX has low absorption and a large volume of material is subjected to EM waves and high mechanical strain-rates. Different laser intensities and aggregate microstructures were investigated to understand hot spot formation in energetic aggregates.

### **5.2 Results**

The energetic aggregate was represented by a 1 mm x 1 mm model consisting of RDX crystals (volume fraction 87.2%) distributed within a PCTFE polymer binder with a volume fraction of 10%. A 2.8% volume fraction of voids is also randomly distributed, which is consistent with porosities associated with these energetic materials [22,53]. The RDX crystals have an average size of 200  $\mu\text{m}$ , and their randomized morphology was generated using a Voronoi tessellation algorithm. GBs had random misorientations between

-15° and +15°. The RDX crystals are modeled with the three slip systems of (010) [001], (021) [100], (02 $\bar{1}$ ) [100] as observed by Gallagher et al. [10], and their material properties are obtained based on Armstrong [9], Clayton et al. [60], and Annapragada et al. [15], as shown in Table 5.1. The specific heat capacity of both RDX and the binder material are estimated to be equivalent based on measurements for RDX-PCTFE aggregates by Baytos [55].

**Table 5.1: Mechanical, Thermal, and Electrical Properties of RDX and PCTFE Binder**

	RDX	Reference	PCTFE	Reference
Density ( $\frac{kg}{m^3}$ )	1820	Armstrong [9]	2158	Brown [17]
Yield Stress (MPa)	300	Clayton et al. [60]	--	--
Elastic Modulus (GPa)	18.4	Armstrong [9]	3.66	Brown [17]
Poisson Ratio	0.22	Annapragada et al. [15]	0.39	Brown [17]
Rate Sensitivity Parameter	0.01*	--	--	--
Thermal Softening Exponent	0.1	--	--	--
Initial Mobile Dislocation Density ( $m^{-2}$ )	$1 \times 10^{10}$ *	--	--	--
Initial Immobile Dislocation Density ( $m^{-2}$ )	$1 \times 10^{12}$ *	--	--	--
Thermal Conductivity ( $\frac{W}{m K}$ )	0.29	Annapragada et al. [15]	0.142	Kline et al. [54]
Specific Heat ( $c_p$ ) ( $\frac{J}{kg K}$ )	1260	Baytos [55]	1260	Baytos [55]
Refractive Index Real Component $n$	1.5	Isbell et al. [57]	1.7	Isbell et al. [57]
Refractive Index Imaginary Component $k$	0.000834	Isbell et al. [57]	0.030400	Isbell et al. [57]

\*Properties assumed based on other crystalline materials due to lack of experimental data for RDX

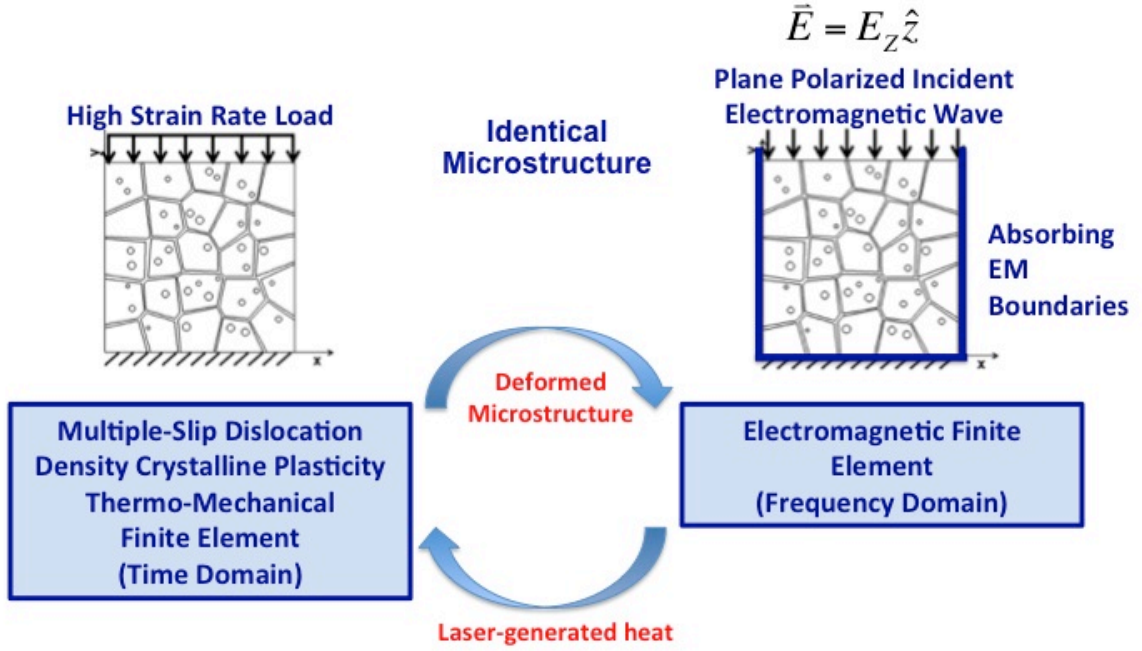
The polymer binder is randomly dispersed between the RDX crystals and is modeled with mechanical properties measured by Brown [17] and thermal conductivity measured by Kline et al. [54] (Table 5.1). It is assumed that the binder material will be in an elastic rubbery stage for the dynamic loading conditions used in this investigation, since its glass transition temperature is approximately 50° C, and the temperatures here due to the EM and adiabatic heating would be lower than this glassy temperature [17]. Thus, it is modeled as a hypo-elastic material based on the first term of Equation (2.6).

Figure 5.1 shows the boundary conditions and applied loads for the thermo-mechanical and EM domain as well as the quantities that are transferred between the domains. Two-dimensional plane strain conditions were used in the thermo-mechanical domain and a displacement boundary condition was applied to the top surface for a constant strain rate of  $10^4 \text{ s}^{-1}$ .

The EM domain is modeled with the same microstructure, and the laser energy was applied to the top surface as a Gaussian beam with the electric field ( $\vec{E}$ ) polarized in the out-of-plane direction as

$$\vec{E} = \left( \sqrt{\frac{2I_0}{c\epsilon_0}} \exp\left(-\frac{(x-x_c)^2}{r^2}\right) \right) \vec{z}. \quad (5.1)$$

This relation specifies the electric field distribution as a function of local  $x$ -coordinate ( $x$ ), beam center ( $x_c$ ), beam radius ( $r$ ), electric field intensity at the beam center ( $I_0$ ), and the constants for light speed ( $c$ ) and permittivity ( $\epsilon_0$ ) in vacuum. The incident beam was centered at the location (0.5, 1.0) mm with a radius of 0.2 mm. It was specified to propagate in the  $y$ -direction, perpendicular to the plane of incidence ( $x$ - $z$  plane) and the polarization direction ( $\vec{z}$ ).



**Figure 5.1: The RDX-PCTFE aggregate with boundary conditions and loading conditions applied in the thermo-mechanical domain (left) and EM domain (right). Quantities transferred between the domains are also shown.**

Two different peak intensities ( $I_0$ ) of  $1 \times 10^5 \text{ W/cm}^2$  and  $1 \times 10^6 \text{ W/cm}^2$  were investigated to study the material response to lower and higher intensity irradiation. Perfectly matched layers were applied on both sides and the lower surface of the model to prevent artificial reflections of the propagating EM wave from these boundaries. We assumed a laser wavelength of  $10.2 \text{ }\mu\text{m}$ , which can be generated by an infrared  $\text{CO}_2$  laser and is only weakly absorbed in RDX. The assumed electrical properties of RDX and binder materials at this wavelength are shown in Table 1, based on measurements by Isbell and Brewster [57]. Electrical properties of the voids are set equal to those of air ( $n = 1$ ,  $k = 0$ ).

### 5.2.1 Low-intensity ( $I_0 = 1 \times 10^5 \text{ W/cm}^2$ ) laser-induced heat generation in various microstructures

The initial electric field magnitude calculated before any deformation has occurred is shown for different microstructural domains (Figure 5.2). For pure RDX containing no binder or defects (Figure 5.2(a)), the EM waves from the laser propagated homogeneously within the material, and the resulting electric field retained its original Gaussian distribution in the  $x$ -direction. The magnitude of the electric field also decayed smoothly in the direction of propagation ( $y$ -direction), since the material had absorbed some of the laser energy at depths below the top surface.

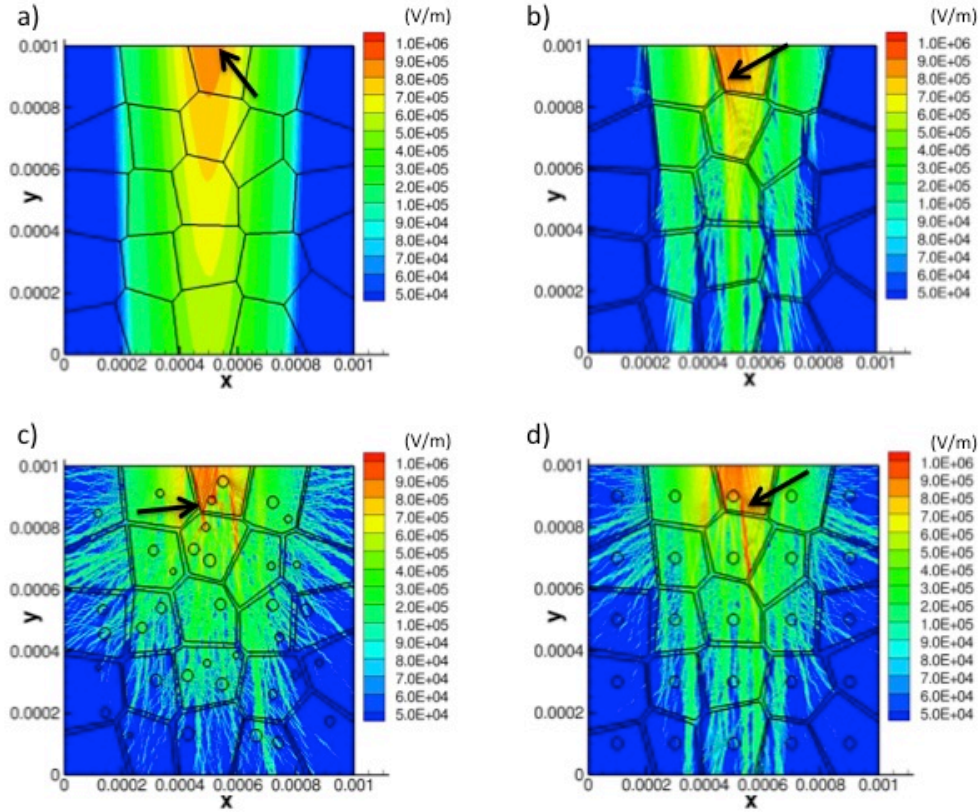


**Figure 5.2:** Electric field magnitude (V/m) obtained from EM finite element solution for various energetic aggregate microstructures before deformation. Arrows indicate the location with maximum electric field in each case. (a) Pure RDX, (b) RDX/Binder with no voids, (c) RDX/Binder with 3 % random porosity, (d) RDX/Binder with 3 % periodic porosity.



With the addition of binder between the RDX grains (Figure 5.2(b)), this homogenous distribution of the electric field was disrupted, particularly in the lower half of the model. This is due to the presence of the polymer binder, which has different electrical properties than the RDX crystals. The mismatch in electrical properties caused internal reflections and refractions at the interfaces between the binder and the RDX crystals, which changed the magnitude and direction of the propagating wave. With the presence of voids, such internal reflections and scattering of the electric field were even more pronounced, since there were three electrically different material surfaces (Figure 5.2(c-d)). The internal reflections also resulted in localized regions where there were high electric fields. These electric field concentrations occurred near the voids, and it can be seen that their locations were different for cases with random void distribution (Figure 5.2(c)) and periodic void distribution (Figure 5.2(d)).

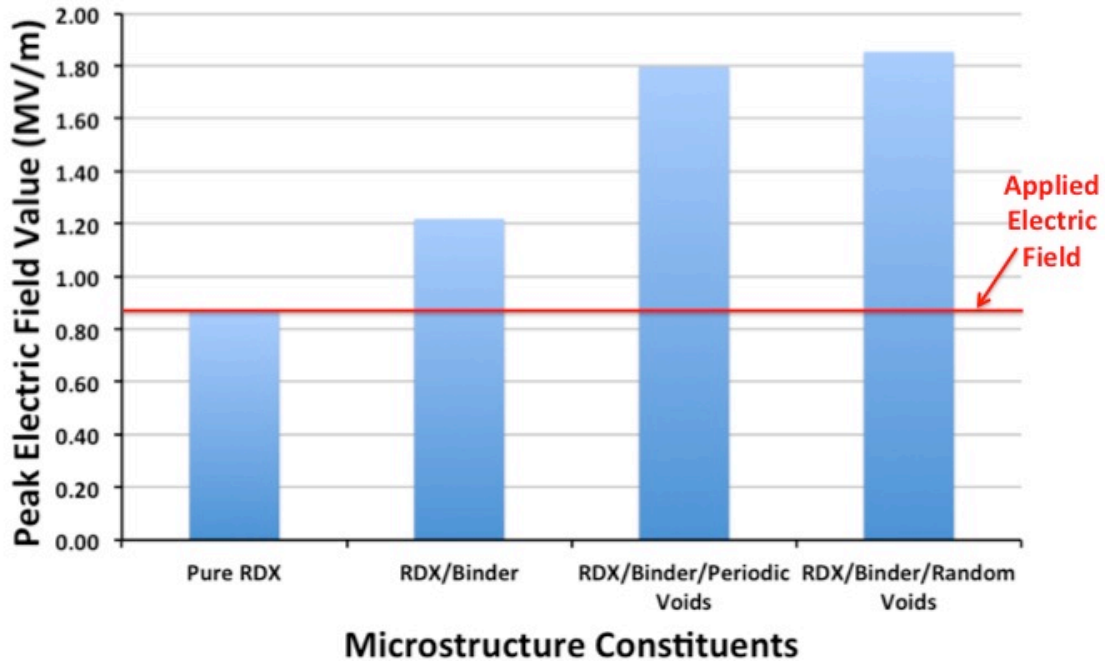


**Figure 5.3: Maximum electric field value (MV/m) for the different energetic microstructures.**

Figure 5.3 shows a bar chart comparison of the peak electric field value for each different microstructure, which occurred at the locations indicated by arrows in Figure 5.2. It can be clearly seen from Figure 5.2 and Figure 5.3 that the heterogeneous microstructure of energetic materials with the polymer binder and defects resulted in a localized electric field magnitude up to 1.8 times greater than the incident field. Both the location and magnitude of these concentrated electric field sites were significantly affected by the microstructural morphology, the orientation of the binder with respect to the propagating EM wave, the size and distribution of voids, and the proximity of voids to the grain edges and binder material.

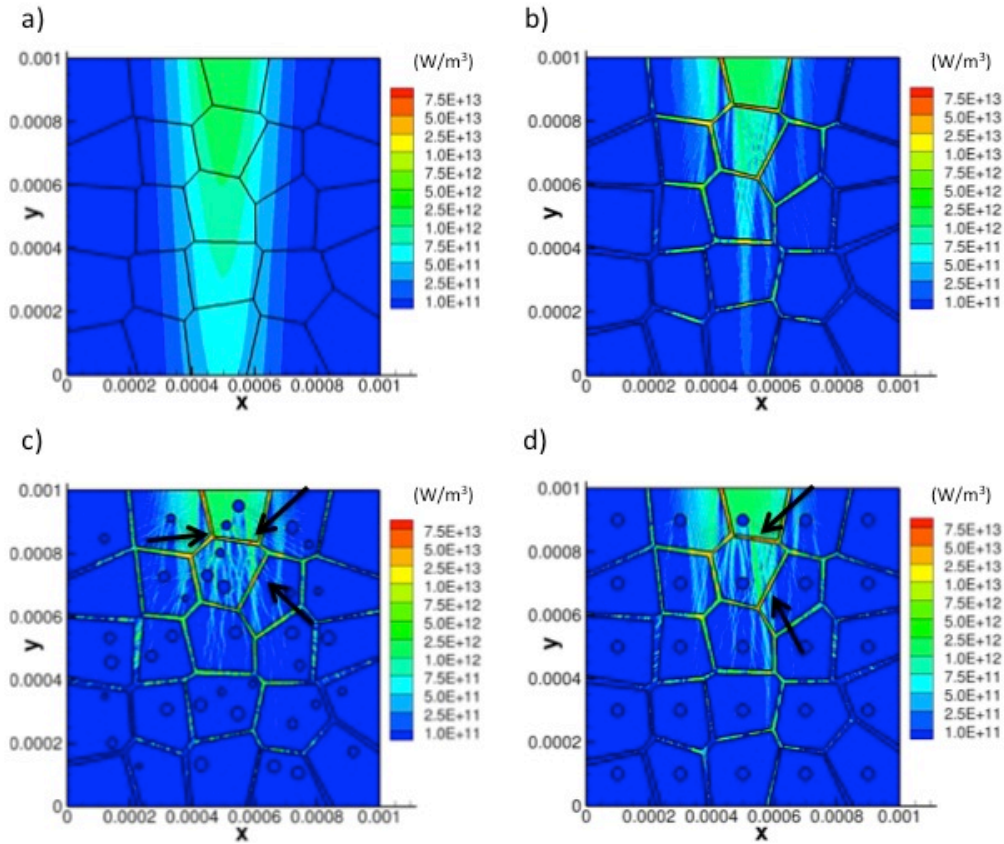


**Figure 5.4: Volumetric laser heat generation rate ( $\text{W/m}^3$ ) obtained from EM finite element solution for various energetic aggregate microstructures before deformation. Arrows indicate localized areas with high laser heat generation. (a) Pure RDX, (b) RDX/Binder with no porosity, (c) RDX/Binder with 3 % random porosity, (d) RDX/Binder with 3 % periodic porosity.**

The laser-generated heating rate for the various microstructures before any deformation has occurred is shown in Figure 5.4. This heating rate is directly proportional to both the electric field intensity and the imaginary part of the material refractive index, which controls how much EM energy the material absorbs (Equations (2.26 – 2.28)). In pure RDX, the laser heat generation occurred as a homogenous function of depth from the top surface and distance from the center of the incident Gaussian beam (Figure 5.4(a)). When the binder was present, however, higher heat generation rates were present within the binder material due to its higher absorption. High absorption in the binder material can reduce the electric field magnitude as the wave propagates into the material, effectively acting to shield the RDX crystals further within the material from much laser heating. However, some localized areas with very high heating rates developed in the binder (Figure 5.4(c-d)) at locations corresponding to the electric field concentrations shown in Figure 5.2.

### ***5.2.2 Low-intensity ( $I_0 = 1 \times 10^5 \text{ W/cm}^2$ ) coupled electromagnetic-thermo-mechanical response***

The fully coupled EM-thermo-mechanical response of the RDX/binder aggregate with a random void distribution is shown in Figure 5.5 compressed to a nominal strain of 8.4% at a strain rate of  $10^4 \text{ s}^{-1}$  and with a laser intensity of  $1 \times 10^5 \text{ W/cm}^2$ . The normal stress was largely compressive, but the voids caused large stress gradients within the material and the formation of some tensile stresses localized at their peripheries (Figure 5.5(a)). This non-uniform stress distribution resulted from inelastic wave reflections that occurred at the peripheries of the voids, the RDX crystal-binder interfaces, and the GB misorientations. Plastic shear strain accumulated in localized regions near the voids and crystal-binder

interfaces (Figure 5.5(b)) where high dislocation densities built up on the dominant slip system (010) [001] (Figure 5.5(c-d)). This behavior is consistent with previous studies of similar materials where it has been shown that voids can act as initiation sites for dislocation activity and localized plasticity [59].

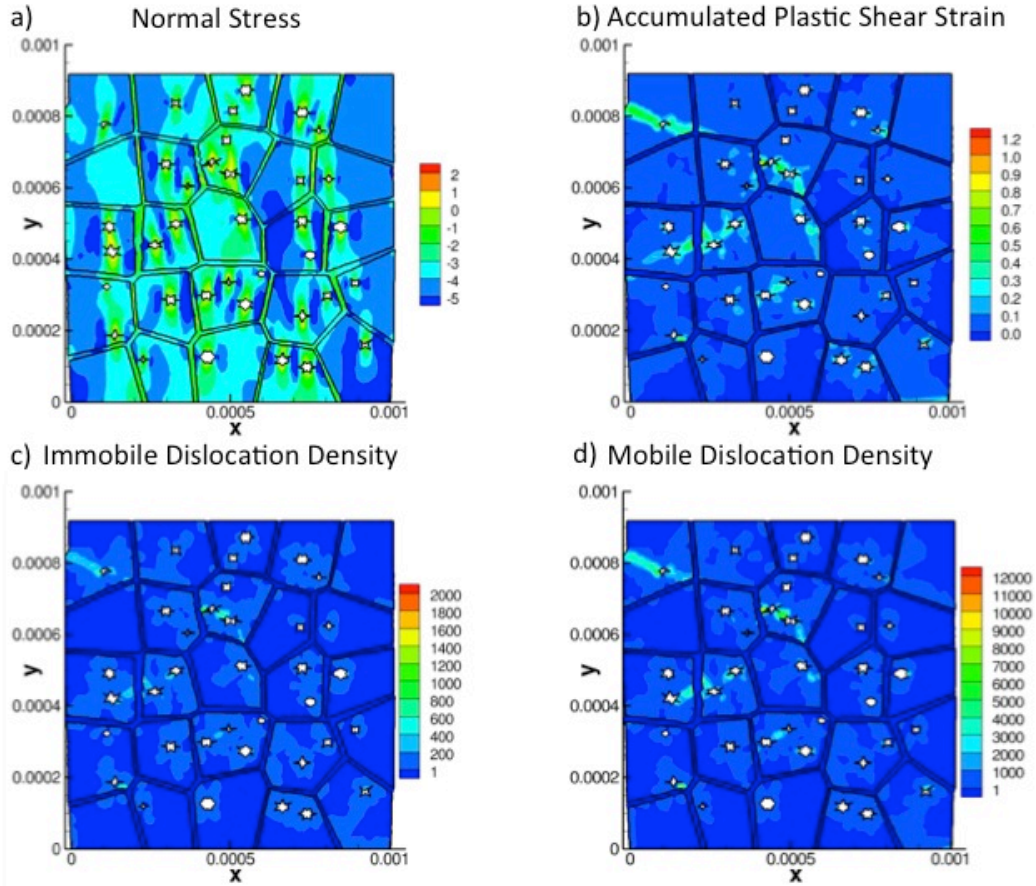


**Figure 5.5: Mechanical response of RDX/binder aggregate with random void distribution compressed to 8.4 % nominal strain with incident laser intensity of  $I_0 = 1 \times 10^5 \text{ cm}^{-1}$ . (a) Normal stress (normalized by static yield stress), (b) Accumulated plastic shear strain, (c) Immobile and (d) Mobile dislocation densities from the most active slip system normalized by the initial dislocation density.**

The total normalized temperature build up within the aggregate is shown in Figure 5.6(a). This predicted temperature distribution was normalized by the initial temperature of 293 K, and it includes the effects of laser heating, thermal decomposition, heating due to plastic

work, and thermal conduction. Most of the material temperatures increased to less than 1.1 times the initial temperature, but there were some regions with significant temperature increases around the voids. In the upper half of the model, the binder had temperatures between 1.2 and 1.6 times the initial temperature and the RDX material adjacent to these areas also had temperature increase due to conduction.

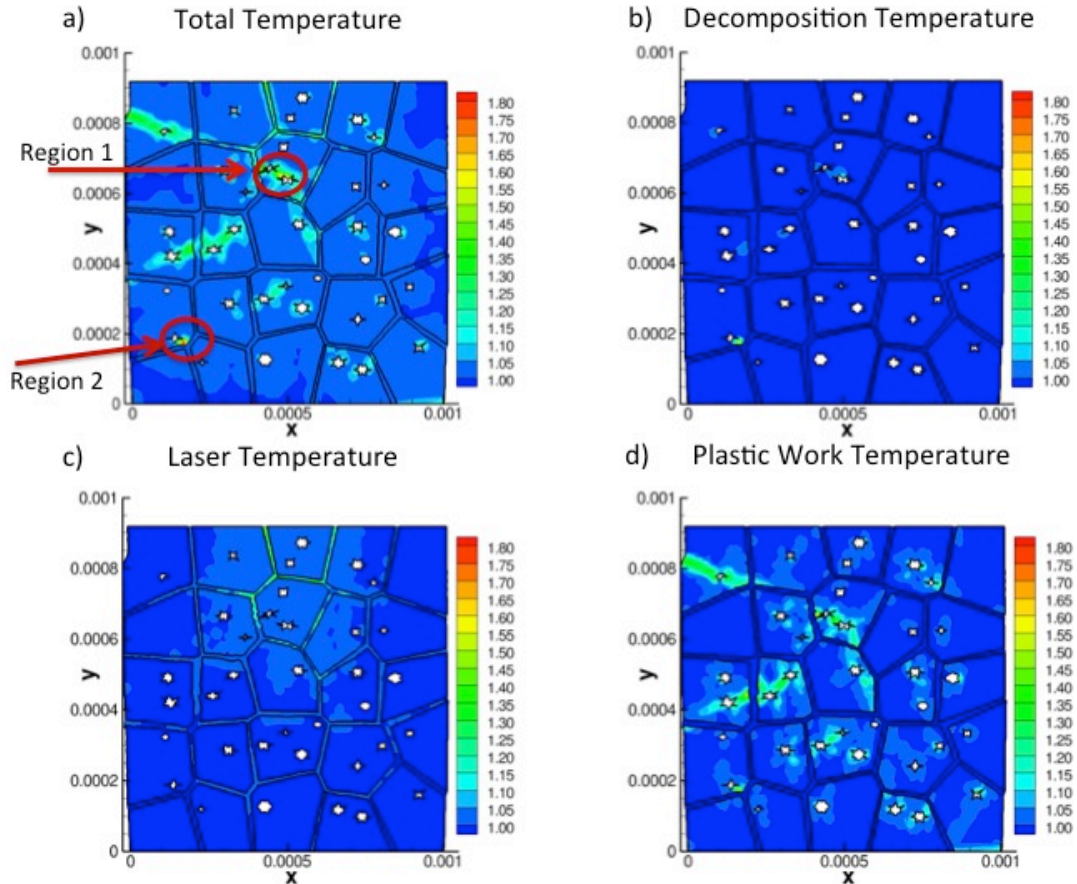


**Figure 5.6: Temperature components normalized by the initial temperature of 293 K for RDX/binder aggregate with random void distribution compressed to 8.4 % nominal strain with incident laser intensity of  $I_0 = 1 \times 10^5 \text{ cm}^{-1}$ . (a) Total temperature increase including effects from conduction, laser heating, decomposition, and plastic work heating. Areas with unbounded temperature increase are highlighted by arrows. (b) Temperature increase due to thermal decomposition of RDX, (c) Laser-induced temperature increase, (d) Plastic work induced temperature increase.**

Temperatures in the two regions highlighted by arrows reached a relatively high value up to 1.8 times the initial temperature, and the temperature continued to increase at an unbounded rate after times of 6.67  $\mu\text{s}$  (Region 1) and 7.96  $\mu\text{s}$  (Region 2). Such unbounded temperature rise has been shown to result in hot-spot formation as noted by LaBarbera and Zikry [59]. This is based on the widely accepted mechanism that hot spots form in energetic materials when heat generation in a localized area occurs faster than heat can be dissipated to the surrounding material [27,58]. This runaway temperature build up is accompanied by thermal decomposition of the energetic crystal, which generates heat at an Arrhenius exponential rate as a function of local temperatures (Equation 2.30). Figure 5.6(b) shows the temperature increase due to thermal decomposition, which occurred mainly in the two locations with unbounded temperature, and it was mostly negligible throughout the rest of the domain.

The temperature increase due to laser heating occurred primarily in the upper half of the model (Figure 5.6(c)) and it was most dominant in the binder. This is due to the higher laser heat generation rate observed in the binder (Figure 5.4) as this material absorbed much more of the laser energy than the RDX crystals at the wavelengths considered in this study. Temperature increases due to plastic work (Figure 5.6(d)) occurred in areas that also had significant shear slip accumulation and dislocation activity (Figure 5.5(b-d)).

It is clear that heating from plastic work is the primary mechanism that contributed to the high temperature increases around the voids, including both locations with unbounded temperature increase (Figure 5.6(a-d)). The hot spot produced at Region 1 formed after 6.67  $\mu\text{s}$ . The primary temperature increase in this area was due to plastic work and

decomposition, but a small temperature rise due to laser heating was also present. The second hot spot formed in Region 2 after a longer time of 7.96  $\mu\text{s}$  in an area where laser heating was insignificant and the only contributions to the temperature increase were plastic work and thermal decomposition mechanisms. Hence, we see that hot spot formation can be accelerated in areas where additional heat generated by laser energy absorption couples with heat generated by high strain rate thermo-mechanical loadings and thermal decomposition mechanisms.

### ***5.2.3 High-intensity ( $I_0 = 1 \times 10^6 \text{ W/cm}^2$ ) coupled electromagnetic-thermo-mechanical response***

Figure 5.7 shows the coupled EM-thermo-mechanical response of the RDX/binder/random voids energetic aggregate compressed to a nominal strain of 8.4% at a strain rate of  $10^4 \text{ s}^{-1}$  with laser radiation at the higher intensity of  $1 \times 10^6 \text{ W/cm}^2$ . The stress state throughout the material was primarily compressive, excluding some regions of tensile stress around the peripheries of the voids (Figure 5.7(a)). These tensile regions occurred due to inelastic wave reflections as before, but both their magnitude and quantity were somewhat higher compared to the case with lower laser intensity. Similarly, the accumulated shear strain (Figure 5.7(b)) and both immobile (Figure 5.7(c)) and mobile (Figure 5.7(d)) dislocation density activity were concentrated in the same general areas as for the lower laser intensity. However, a comparison between the two cases shows more widespread dislocation density activity propagating further outward from the void edges and into the RDX grains for the higher intensity case. This indicates that the higher laser intensity resulted in more favorable conditions for slip and inelastic deformation within the material.



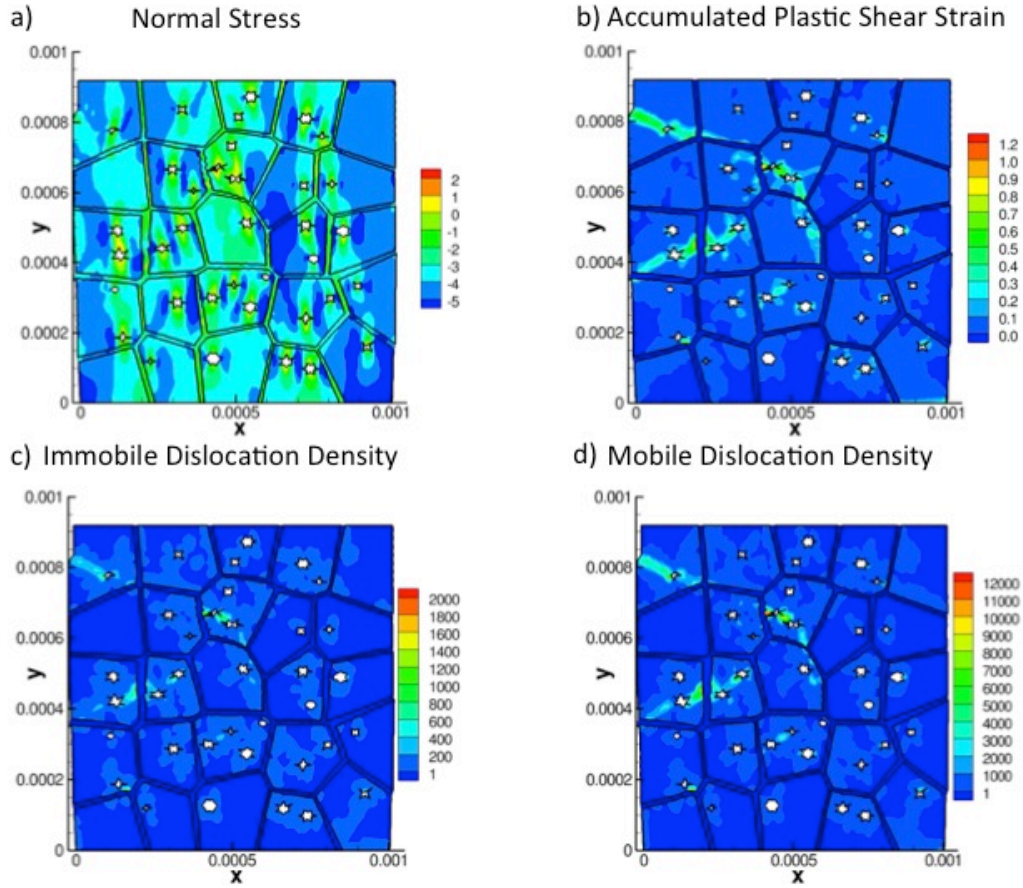


**Figure 5.7: Mechanical response of RDX/binder aggregate with random void distribution compressed to 8.4 % nominal strain with incident laser intensity of  $I_0 = 1 \times 10^6 \text{ cm}^{-1}$ . (a) Normal stress (normalized by static yield stress), (b) Accumulated plastic shear strain, (c) Immobile and (d) Mobile dislocation densities from the most active slip system normalized by the initial dislocation density.**

The total normalized temperature is shown in Figure 5.8(a). High temperatures of 1.8 times the initial temperature occurred along the interfaces between the binder and the RDX crystals within the upper half of the model. Additional moderate temperature rises between 1.2 and 1.5 times the initial temperature were localized in areas of high shear slip near the voids.

In this case with higher laser intensity, several hot spots with unbounded temperatures occurred, mostly in the regions along the binder interface (Region 1) after  $2.83 \mu\text{s}$  and also in



the same location seen in the lower intensity case (Region 2) after 7.96  $\mu\text{s}$ . High decomposition temperatures also occurred in multiple locations (Figure 5.8(b)), indicating that hot spots formed and propagated outward from the binder-interface region into the bulk RDX crystals.

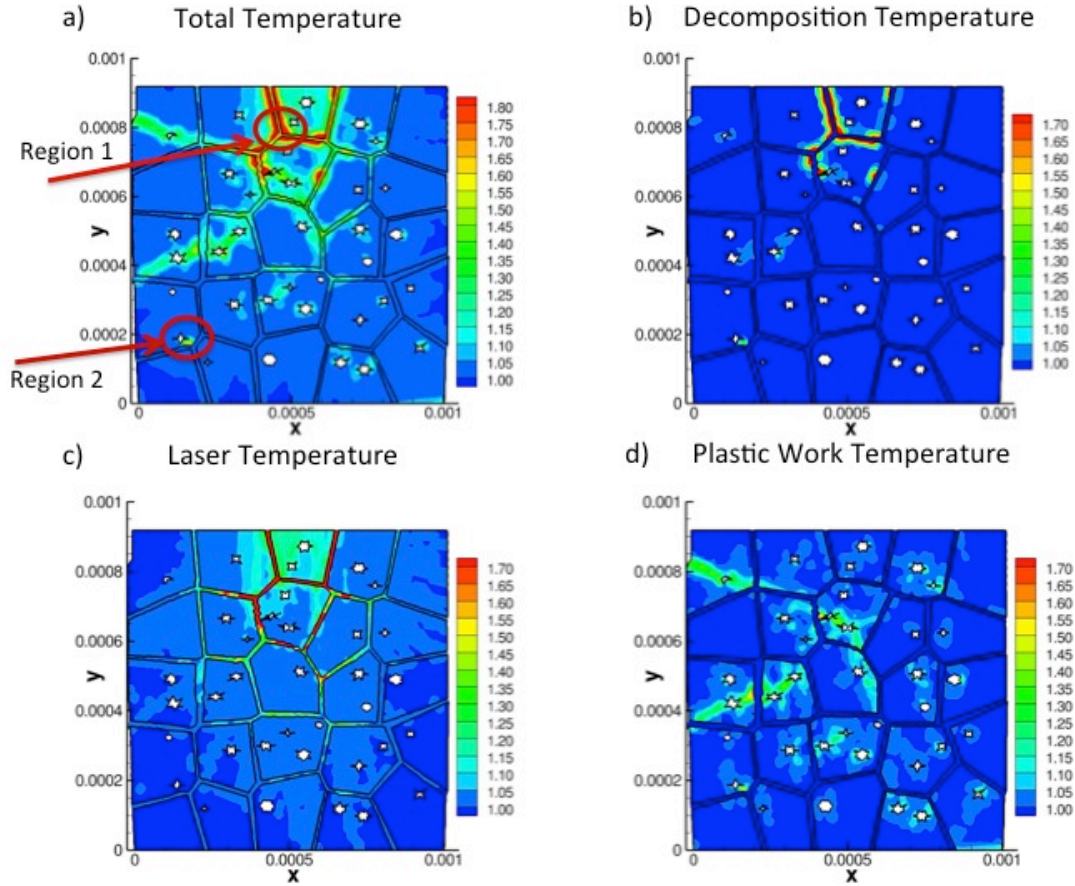


**Figure 5.8: Temperature components normalized by the initial temperature of 293 K for RDX/binder aggregate with random void distribution compressed to 8.4 % nominal strain with incident laser intensity of  $I_0 = 1 \times 10^6 \text{ cm}^{-1}$ . (a) Total temperature increase including effects from conduction, laser heating, decomposition, and plastic work heating. Areas with unbounded temperature increase are highlighted by arrows. (b) Temperature increase due to thermal decomposition of RDX, (c) Laser-induced temperature increase, (d) Plastic work induced temperature increase.**

As with the low intensity case, high laser-induced temperature increase occurred in the binder with relatively smaller temperature increases in the RDX crystals (Figure 5.8(c)). However, the higher intensity laser resulted in a faster heat generation rate (Equations (2.26 – 2.28)) that led to higher temperature accumulation than the low intensity case, especially in the grains closest to the top surface. The spatial variations in laser heat generation rate (Figure 5.4) due to the scattered electric field (Figure 5.2) also led to more significant variations in the temperature field when the higher laser intensity was applied. The temperature increases due to plastic work heating were localized in regions of high shear slip around the voids and had magnitudes ranging between 1.1 and 1.5 times the initial temperature (Figure 5.8(d)). This is less than the laser-induced temperature increases, indicating that for the higher intensity case, the laser heat generation occurred on a faster timescale than heat generated due to plasticity at this strain rate. Additionally, most of the decomposition temperature accumulation and hot spot formation occurred as heat conducted from the binder into the neighbor RDX crystals, which indicates that hot spot formation was dominated by the laser heating.

Further insight into the hot spot generation mechanisms can be gained from snapshots of total temperature evolution at several different times, as shown in Figure 5.9. The initial temperature increase initiated in the binder (Figure 5.9(a)), and then propagated into the adjacent RDX crystals over time as heat conducted into these areas from the higher temperature binder (Figure 5.9(b)). Hot spots initially formed at regions adjacent to the binder (Figure 5.9(c)), and subsequently coalesced into large regions with unbounded temperature increases along the crystal-binder interfaces (Figure 5.9(d)).

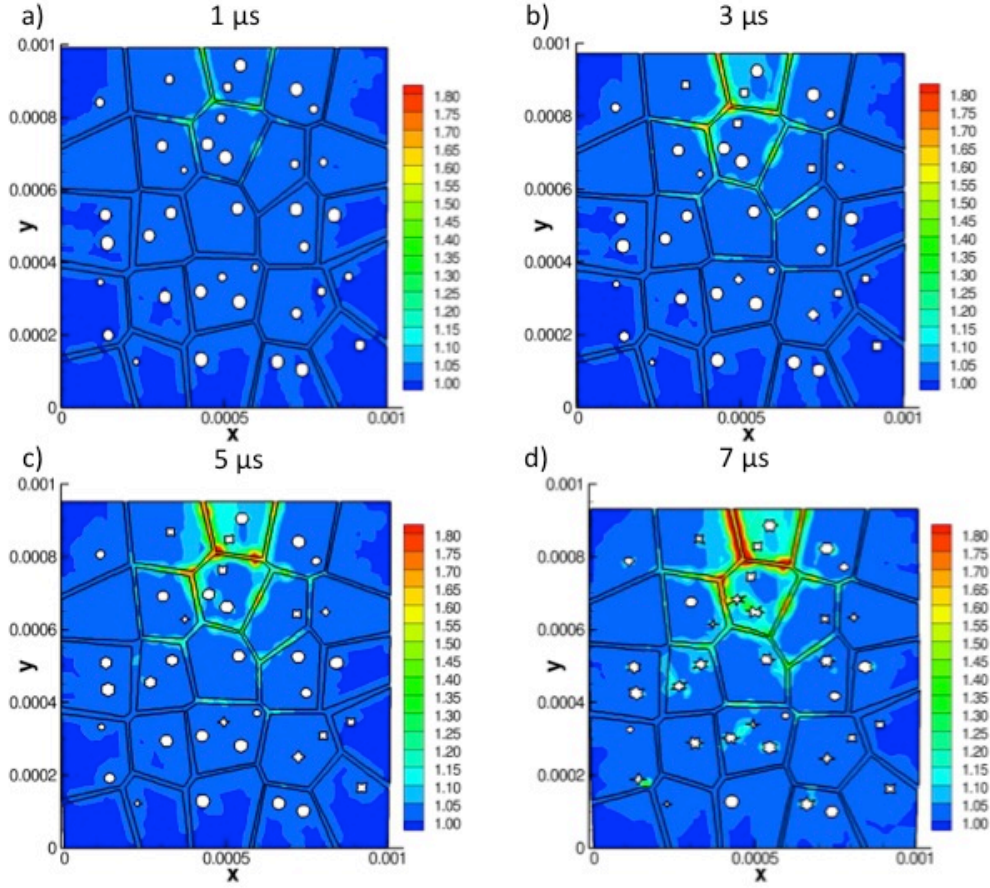


**Figure 5.9:** Total temperature evolution over time with laser intensity of  $I_0 = 1 \times 10^6 \text{ cm}^{-1}$  at times of (a)  $1 \mu\text{s}$ , (b)  $3 \mu\text{s}$ , (c)  $5 \mu\text{s}$ , and (d)  $7 \mu\text{s}$ . All temperatures are normalized by the initial temperature of 293 K.

The sites of initial hot spot formation in Figure 5.9(c) corresponded to the locations with highly concentrated electric field magnitudes (Figure 5.2(c)) and high laser heat generation rates in the binder (Figure 5.4(c)). Hence, the effects of laser wave propagation through the heterogeneous microstructure can significantly affect the locations of hot spot formation under wavelengths with low RDX absorption. This behavior is consistent with experimental observations by Chen et al. [31,32], where single RDX crystals were irradiated at wavelengths with low RDX absorption and temperatures increased in localized areas near crystal facets or internal defects. Thus, it is critical that the material's coupled EM-thermo-

mechanical response is considered to accurately predict hot spot formation when laser energy penetrates far enough to interact with the heterogeneous microstructure.

#### 5.2.4 Hot Spot Generation Mechanisms

A comparison of the temperature-time history from the region that first developed unbounded temperature for both low and high intensity cases is shown in Figure 5.10. A case without the laser (strain rate load only) is also included for comparison.

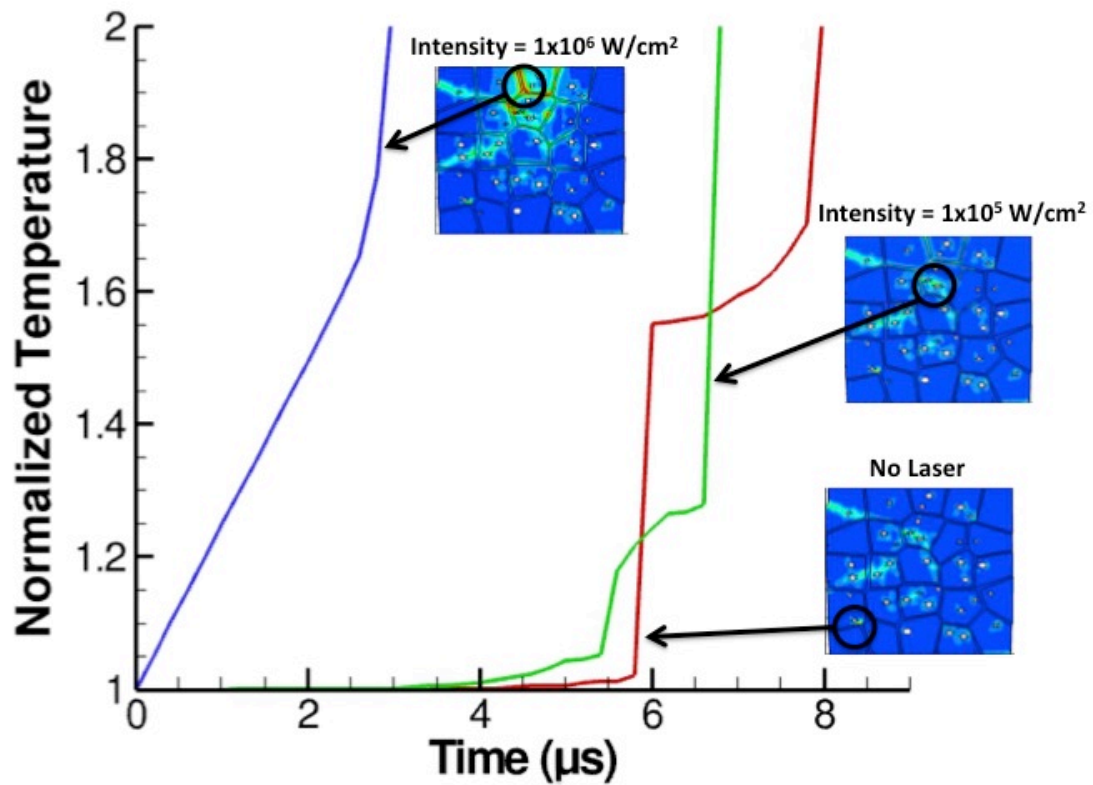


**Figure 5.10: Temperature-time history for locations where the first hot spot developed. All temperatures are normalized by the initial temperature of 293 K.**

For the case without the laser, hot spot formation was governed solely by heat generation due to plastic work. The sharp increase in temperature seen at approximately 6  $\mu$ s is associated with rapid slip that occurred as the circled region between the void and binder began to collapse, followed by additional heating at a nonlinear rate as the material continued

to deform. Once heat generated by the thermal decomposition reaction became significant, the temperature rise quickly became unbounded, and a hot spot developed at 7.96  $\mu\text{s}$ .

With the addition of the lower laser intensity of  $1 \times 10^5 \text{ W/cm}^2$ , hot spot formation was slightly accelerated and occurred at different random locations. The slight temperature increase due to laser heating can be seen between 4 - 5.5  $\mu\text{s}$ , followed by the nonlinear temperature increases associated with plastic work heating. The unbounded temperature increases associated with thermal decomposition and hot spot formation began at 6.67  $\mu\text{s}$ . For the higher laser intensity of  $1 \times 10^6 \text{ W/cm}^2$ , the laser-induced heating mechanisms occurred at a much faster rate, and the initial hot spot formed by thermal conduction from the binder into neighboring RDX crystals. This is clearly seen from Figure 5.10, as the initial temperature increase next to the binder is linear, and became unbounded with the onset of thermal decomposition at 2.83  $\mu\text{s}$ .

From this comparison, the effect of laser intensity on the rate of temperature increase within the material and subsequent hot spot formation is evident. For a given wavelength and material microstructure, a higher intensity laser irradiation will cause the material to heat more quickly. Furthermore, the proximity of the rates of heat generation due to plastic work and laser heating will determine whether one of these mechanisms dominates hot spot formation. For the current study, at the lower intensity of  $1 \times 10^5 \text{ W/cm}^2$ , plastic work heating occurred at a faster rate than laser-induced heating. The subsequent hot spot formation was largely governed by locations with high plastic deformation and laser heating played a relatively small role. For the case with higher intensity of  $1 \times 10^6 \text{ W/cm}^2$ , the laser heating

occurred at a much faster rate than plastic work heating, and the EM wave propagation and absorption of laser energy governed the location that hot spots formed.

### 5.3 Summary

A new computational approach that couples high frequency EM wave propagation, heat generation and transfer, and thermo-mechanical response of materials was developed and used to study the response of RDX-PCTFE energetic aggregates to laser irradiation and high strain rate mechanical loads. The laser heating distribution is obtained from a finite element solution of Maxwell's equations and then mapped to the thermo-mechanical domain, where it is coupled with thermal decomposition, adiabatic heating, and mechanical dislocation-density crystalline plasticity deformation and stresses.

The heterogeneous microstructure of energetic aggregates that includes crystalline grains, binder, and voids, resulted in internal reflections and scattering of the EM wave due to the differences in electrical properties of these components. This effect was particularly notable for microstructures with voids, and often resulted in localized areas with a concentrated electric field magnitude up to 1.8 times greater than the applied field. For the wavelengths considered in this study, laser heat generation occurred mainly in the binder and was particularly high in areas where EM wave reflections caused locally concentrated electric fields. Additionally, the heterogeneous microstructure and unique slip systems of RDX resulted in non-uniform stress states and localized areas of dislocation density activity, accumulated plastic shear strain, and adiabatic plastic work heating around the voids.

Two case studies of the fully coupled response of RDX-PCTFE energetic aggregates at a high strain rate load of  $10^4 \text{ s}^{-1}$  and two different laser intensities were considered. For the

case with lower laser intensity of  $1 \times 10^5 \text{ W/cm}^2$ , mechanical plastic work heating and thermal decomposition were the primary sources of hot spot generation. However, hot spot formation was accelerated when plasticity occurred in a location where laser heat generation was also present. At the higher laser intensity of  $1 \times 10^6 \text{ W/cm}^2$ , laser heating in the binder occurred at a much faster rate than inelastic slip in the RDX crystals. Consequently, hot spots formed as heat conducted from the higher temperature binder into the neighboring RDX crystals, and this triggered the thermal decomposition reaction. In this case, hot spots formed at sites with high electric field localization and propagated along the crystal-binder interfaces.

The specific mechanisms that contribute to hot spot formation in heterogeneous energetic aggregates under laser and high strain rate loads are strongly dependent on the incident laser parameters, microstructure morphology, and the EM and mechanical properties of the material constituents. The rate of laser heating is controlled by both the material absorption properties and the laser intensity, while the rate at which plasticity develops and generates heat is controlled by the strain rate, microstructure, and mechanical properties. Hence, a fully coupled modeling approach is necessary to understand the interrelated effects of EM wave propagation, laser energy absorption, thermo-mechanical behavior, and the microstructural mechanisms that affect failure in heterogeneous energetic aggregates under incident laser irradiation.

## **CHAPTER 6: The Effect of Microstructure on the Coupled EM-Thermo-Mechanical Response of RDX-Estane Aggregates to Infrared Laser Radiation**

### **6.1 Introduction**

Complex microstructure features present in energetic aggregates, such as crystal-binder interfaces, crystal morphology, polymer binder volume fraction, voids, grain boundaries, and dislocation densities strongly affect EM wave propagation and the coupled thermo-mechanical behavior under laser irradiation. Additionally, many energetic aggregates contain estane as the polymer binder, which will be above its glass transition temperature during laser-induced heating and exhibit viscoelastic behavior.

The coupled electromagnetic-thermo-mechanical response of RDX-estane energetic aggregates under laser irradiation and high strain rate loads has been investigated for various aggregate sizes and binder volume fractions to understand the complex interactions between EM waves, mechanical behavior and aggregate microstructure.

### **6.2 Results**

The energetic aggregate was represented by a 1 mm x 1 mm model consisting of RDX crystals distributed within an estane polymer binder. Both 16-grain and 49-grain aggregates were considered to study the effects of grain size and aggregate size. Two binder volume fractions of 10% and 30% were used. The average grain size was 210 – 230  $\mu\text{m}$  for the 16-grain aggregates and 120 – 135  $\mu\text{m}$  for the 49-grain aggregates. Grain morphologies were generated using a Voronoi tessellation algorithm, and the crystals were given randomly generated orientations varying between 30° and 60° from the reference axes such that grain boundaries had angular misorientations of up to 30°. Furthermore, since voids are known to



be present in energetic materials, randomly distributed voids comprised approximately 2.8% volume fraction of the aggregates [22,53].

The RDX crystals were assumed to have the three independent slip systems of (010) [001], (021) [100], (02 $\bar{1}$ ) [100] based on Gallagher et al. [10], and their mechanical, thermal, and electrical properties are shown in Table 6.1. The estane binder was randomly dispersed between the RDX crystals and was modeled as a viscoelastic material with properties for each Maxwell element from the experimental data of Mas et al. [46]. Additional thermal and electrical properties are shown in Table 6.1.

**Table 6.1: Mechanical, Thermal, and Electrical Properties of RDX Crystals and Estane Binder**

	RDX	estane
Density ( $\frac{kg}{m^3}$ )	1820 [9]	1190 [46]
Yield Stress (MPa)	300 [60]	--
Elastic Modulus (GPa)	18.4 [9]	--
Poisson's Ratio	0.22 [15]	0.499 [14]
Thermal Conductivity ( $\frac{W}{m K}$ )	0.29 [15]	0.14 [61]
Specific Heat ( $c_p$ ) ( $\frac{J}{kg K}$ )	1260 [15]	1500 [14]
Refractive Index Real Component $n$	1.5* [57]	1.7* [62,63]
Refractive Index Imaginary Component $k$	0.000834* [32,57]	0.030400* [32]

\*Values estimated at wavelength of 10.3  $\mu m$

The thermo-mechanical domain was modeled using symmetry boundary conditions for plane strain loading (Figure 6.1). To approximate the mechanical loading that can accompany high intensity laser irradiation, a displacement boundary condition was applied to the top surface for a compressive strain rate of  $10^3 \text{ s}^{-1}$ .

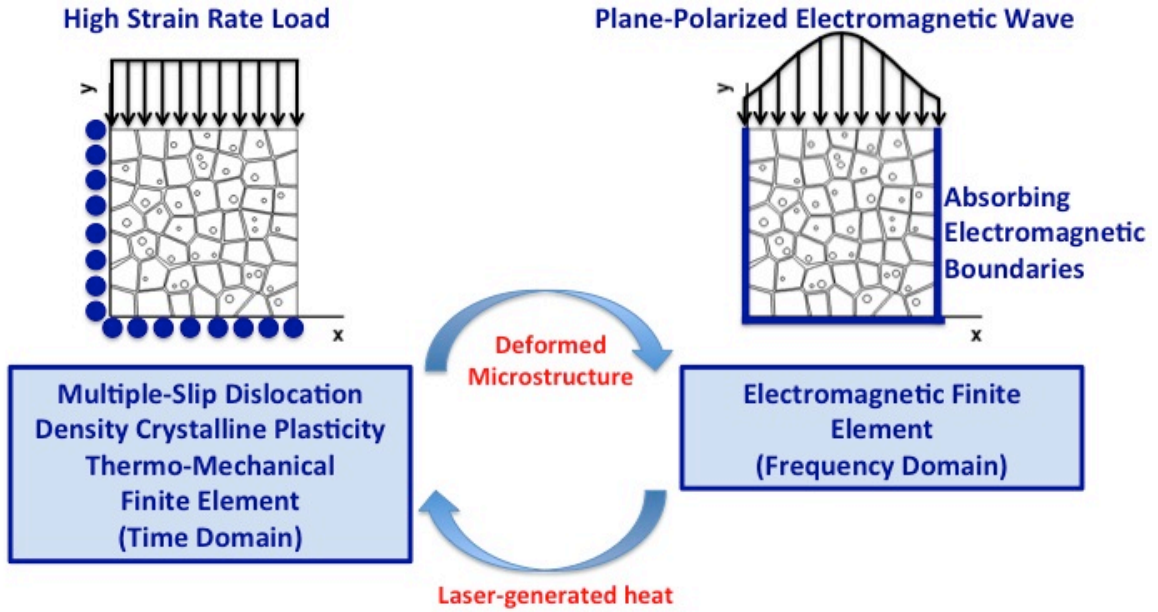


**Figure 6.1:** The RDX-estane aggregate with boundary conditions and loading conditions applied in the thermo-mechanical domain (left) and electromagnetic domain (right). Quantities transferred between the domains are also shown.

The EM domain was modeled with the same microstructure (Figure 6.1), and the laser energy was applied to the top surface as a Gaussian beam with the electric field ( $\vec{E}$ ) polarized in the out-of-plane direction ( $\vec{z}$ ) as

$$\vec{E} = \left( E_0 \exp \left( -\frac{(x-x_c)^2}{r^2} \right) \right) \vec{z}. \quad (6.1)$$

Equation 6.1 specifies the applied electric field distribution as a function of local  $x$ -coordinate ( $x$ ), beam center ( $x_c$ ), beam radius ( $r$ ), and electric field magnitude at the beam center ( $E_0$ ). The applied beam was centered at  $x_c = 0.5 \text{ mm}$  with a radius of  $0.5 \text{ mm}$  and

intensity of  $2.8 \times 10^5 \text{ W/cm}^2$ , corresponding to an applied electric field magnitude of  $E_0 = 1.45 \text{ MV/m}$ . It was specified to propagate in the  $y$ -direction, perpendicular to the plane of incidence ( $x$ - $z$  plane) and the polarization direction ( $\vec{z}$ ).

Perfectly matched layers were applied on both sides and the lower surface of the EM domain to prevent artificial reflections of the propagating EM wave from these boundaries. We assumed a laser wavelength of  $10.3 \text{ }\mu\text{m}$ , which is only weakly absorbed in both RDX and estane. The assumed electrical properties of RDX and estane are shown in Table 6.1. Electrical properties of the voids were set equal to those of air with  $n = 1$  and  $k = 0$ .

### ***6.2.1 Aggregate with 16 grains and 10% volume fraction binder***

Figure 6.2(a) shows the magnitude of the electric field vector, normalized by the maximum applied electric field value,  $E_0$ , for a nominal strain rate of  $10^3 \text{ s}^{-1}$ , and after a time of  $10 \text{ }\mu\text{s}$ . The corresponding volumetric laser heat generation rate is shown in Figure 6.2(b). At this time, the material was compressed to a nominal strain of 10%, and several crystals began to protrude from the free surface.

Most of the aggregate had electric field magnitudes ranging from 1 to 0.4 times the applied electric field, with the exception of a few regions with magnitudes less than 0.2 in the lower left corner and the right side (Figure 6.2(a)). This resulted as the EM wave was diverted from an area due to the sliding of the binder. Within approximately  $0.2 \text{ mm}$  from the top surface, the electric field was concentrated in the binder ligaments with values ranging from 1.4 – 2 times the applied field. Very localized areas within the upper RDX grains also had electric field magnitudes greater than the applied field.

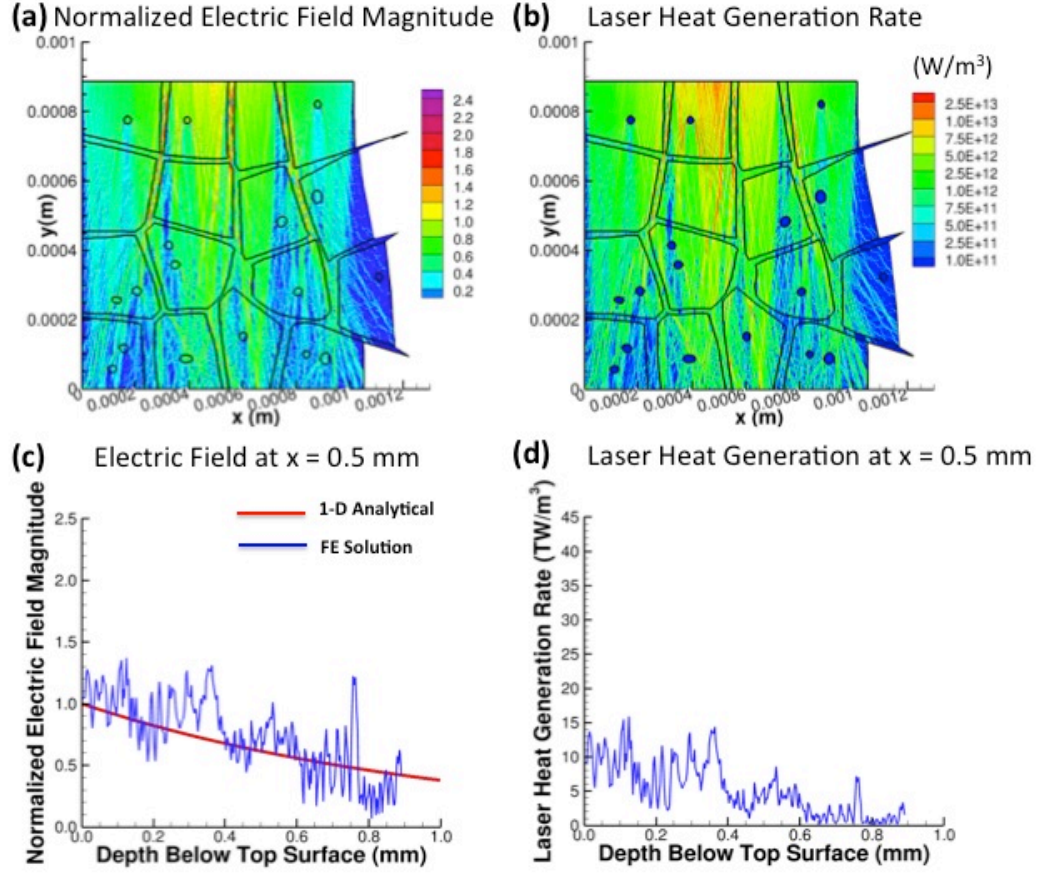


**Figure 6.2:** Electric field magnitude (normalized by the applied electric field  $E_0$ ) and laser heat generation rate for 16-grain 10 % binder aggregate after 10  $\mu\text{s}$ . (a) Normalized electric field, (b) Volumetric laser heat generation rate, (c) Normalized electric field magnitude as a function of depth below the top surface at  $x = 0.5$  mm, (d) Volumetric laser heat generation rate as a function of depth below the top surface at  $x = 0.5$  mm.

This non-uniform electric field distribution resulted as the mismatch of electrical refractive index between the different material constituents caused a portion of the EM wave to reflect at each interface and also changed its direction. Since the microstructural features of grain morphology, binder ligaments, and voids, are generally of equal size or larger than the infrared wavelength investigated (10.3  $\mu\text{m}$ ), these reflections depended on the interface geometry, refractive index mismatch between the materials, and angle of incidence between the EM wave and the interface through the laws of geometric optics. Energetic aggregates

contain numerous interfaces between the RDX crystals, polymer binder, and voids, which contributed to the scattering and localization patterns seen in Figure 6.2(a). Similar EM scattering has been observed experimentally in PBX simulant aggregates exposed to THz radiation and was affected by the grain size and shape as well as the EM frequency [33].

The laser heat generation rate generally followed the same spatial distribution as the electric field, and the highest values occurred in the central grains and binder ligaments close to the top surface (Figure 6.2(b)). Since both RDX and estane have low absorption coefficients at the wavelength investigated, laser heat generation was present throughout the entire depth of the model and neither material showed preferential absorption. Consequently, the laser heat generation rate distribution was governed primarily by the local electric field magnitude.

The normalized electric field magnitude and laser heat generation rate at the center of the applied laser beam,  $x = 0.5$  mm, are shown as a function of depth below the top surface (Figure 6.2(c-d)). The electric field predicted for one-dimensional EM wave propagation in homogeneous RDX given by

$$E(y) = \frac{E}{E_0} \exp \left[ \frac{-2\pi k}{\lambda c} (y_0 - y) \right] \quad (6.2)$$

is shown in Figure 6.2(c) for comparison with the computational predictions.

The normalized electric field magnitude decayed from a value of 1 at the top surface to approximately 0.4 times the incident field at the lower surface. This follows the same trend predicted for homogeneous RDX, but the variations resulting from internal reflections at the crystal-binder interfaces are clearly apparent. These variations were also seen in the

laser heat generation rate, which decayed with depth below the top surface but had local peaks associated with areas of high electric field (Figure 6.2(d)).

The normal stress distribution is shown in Figure 6.3(a). Most of the RDX grains had compressive stresses between 2 – 3 times the static yield stress, but there were also very localized high compressive stress accumulations at the grain corners and void peripheries. The binder had compressive stresses in its horizontal ligaments and tensile stresses in the vertical ligaments. This occurred as some of the grains bulged outward at the free surface through lateral binder sliding, effectively pulling on the connected vertical ligaments.

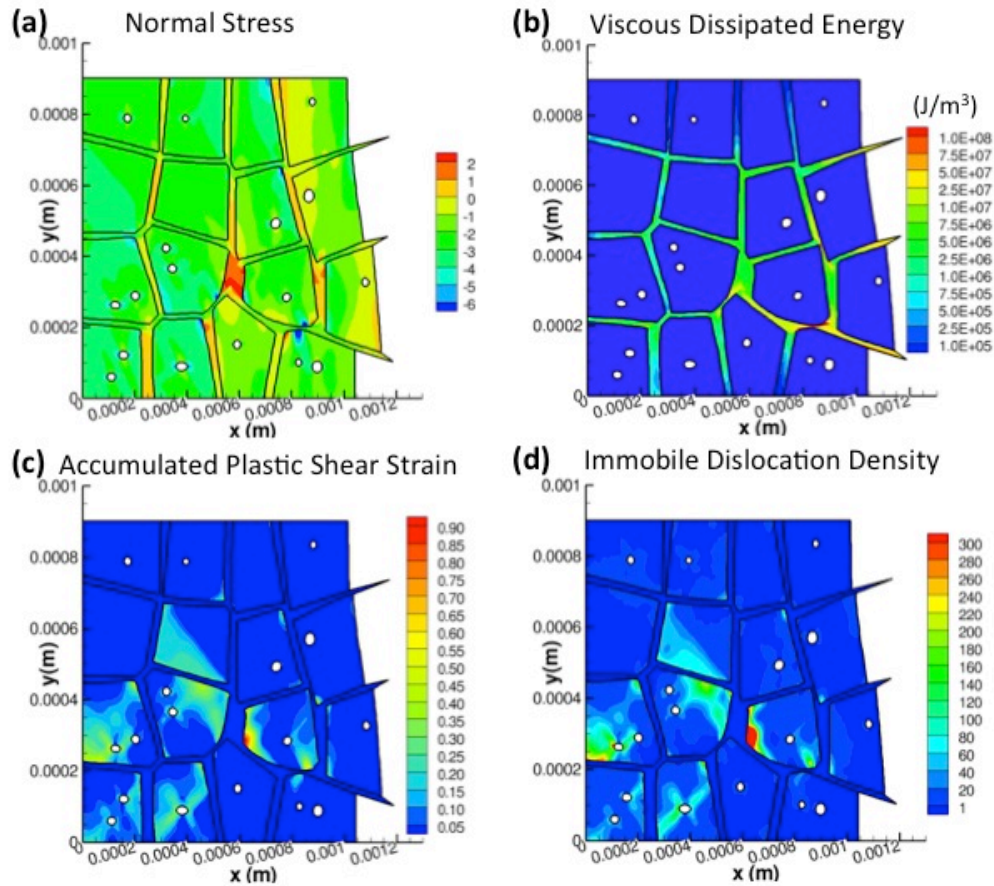


**Figure 6.3: Response of 16-grain, 10% binder aggregate after 10  $\mu$ s. (a) Normal stress (normalized by RDX yield stress), (b) Energy dissipated by viscous sliding in binder, (c) Accumulated crystalline plastic shear strain, (d) Immobile dislocation density on the most active slip system (021) [100].**

Energy dissipated by viscous sliding occurred throughout most of the binder (Figure 6.3(b)), but was concentrated in the regions close to the free edge where large amounts of sliding occurred. Crystalline plastic shear strains (Figure 6.3(c)) accumulated at the grain corners, voids, and locations with large stress gradients at the crystal-binder interface. Immobile dislocation densities also accumulated in these locations, shown normalized by the initial dislocation density for the most active slip system (021) [100] (Figure 6.3(d)). Dislocation activity was much less on the other slip systems, with immobile dislocation densities less than 50 times the initial value. This is consistent with experimental observations that slip system activity in RDX crystals is highly dependent on the crystal orientation with respect to applied load, and dislocation activity occurs predominantly on one or two slip systems[10,11].

The total temperature accumulation within the aggregate is shown in Figure 6.4(a), including effects of thermal conduction and the various heat generation sources. All temperatures are normalized by the initial temperature of 293 K. Temperatures in the entire aggregate increased to at least 1.1 times the initial temperature. More significant temperature increases between 1.1 – 1.3 occurred between  $x = 0.3$  mm to  $x = 0.9$  mm at the center of the applied Gaussian laser beam. The maximum temperature increase occurred in a grain corner with a high accumulation of shear slip and dislocation activity (Figure 6.3(c-d)).

The temperature increase associated with laser heating (Figure 6.4(b)) largely followed the spatial pattern seen in the electric field and the laser heat generation rate (Figure 6.2(a-b)), including areas with localized heating in the binder where electric field concentrations were present. Temperature increases associated with plastic work heating



(Figure 6.4(c)) were present in areas with shear slip and dislocation activity (Figure 6.3(c-d)) and were locally higher in magnitude than the laser-generated temperature increase. Viscous energy dissipation also produced temperature increases in areas of the binder where viscous sliding occurred (Figure 6.4(d)).

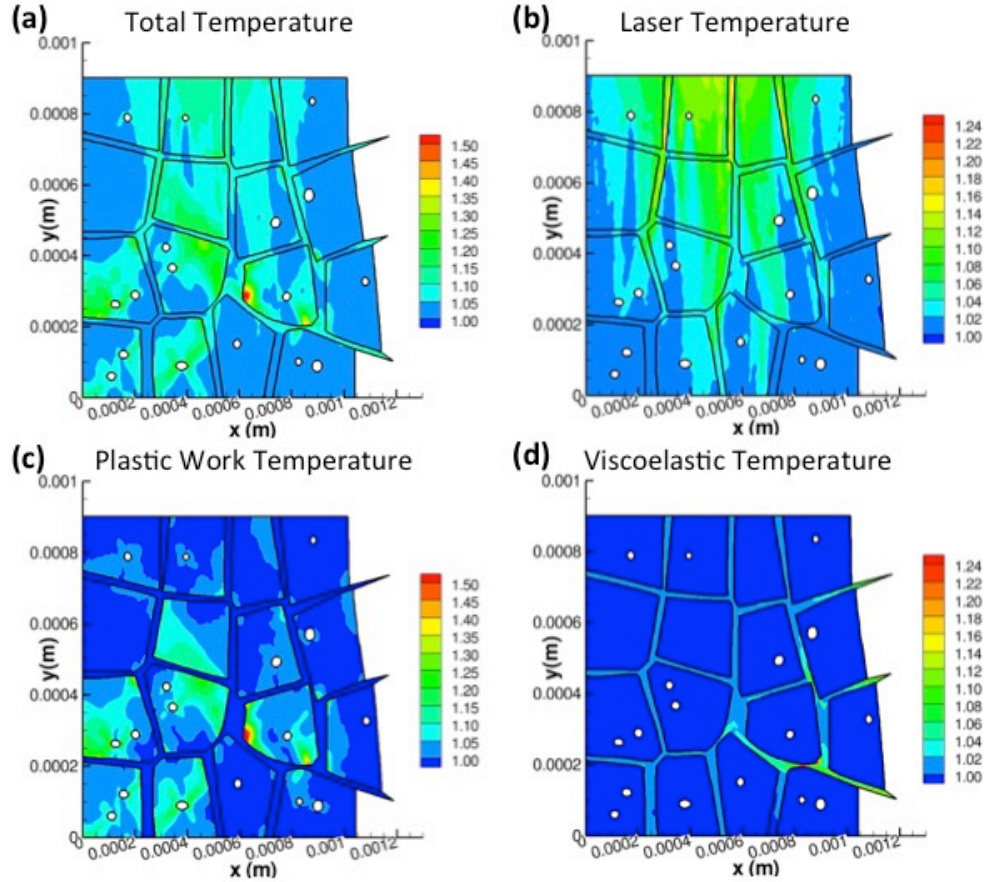


**Figure 6.4: Temperature accumulation (normalized by initial temperature) in 16-grain, 10% binder aggregate after 10  $\mu$ s. (a) Total temperature increase, (b) Temperature increase due to laser heating, (c) Temperature increase due to plastic work, (d) Temperature increase due to viscous sliding.**

In this case, the effects of thermal decomposition did not play a major role since the maximum temperature increase was only 1.5 times the initial temperature of 293 K.

Temperatures on the order of 489 K are necessary for thermal decomposition (Equation (2.30)) to produce significant heating and potentially become a runaway reaction indicative



of hot spot formation [49,59]. Laser heating was the main mechanism to increase the temperature throughout the model, while plastic work and viscous dissipation contributed additional heat to local areas where these mechanisms were present.

### 6.2.2 Aggregate with 49 grains and 10% volume fraction binder

The normalized electric field distribution and laser heat generation rates are shown in Figure 5 for a nominal strain rate of  $10^3 \text{ s}^{-1}$ , and after  $10 \mu\text{s}$ .

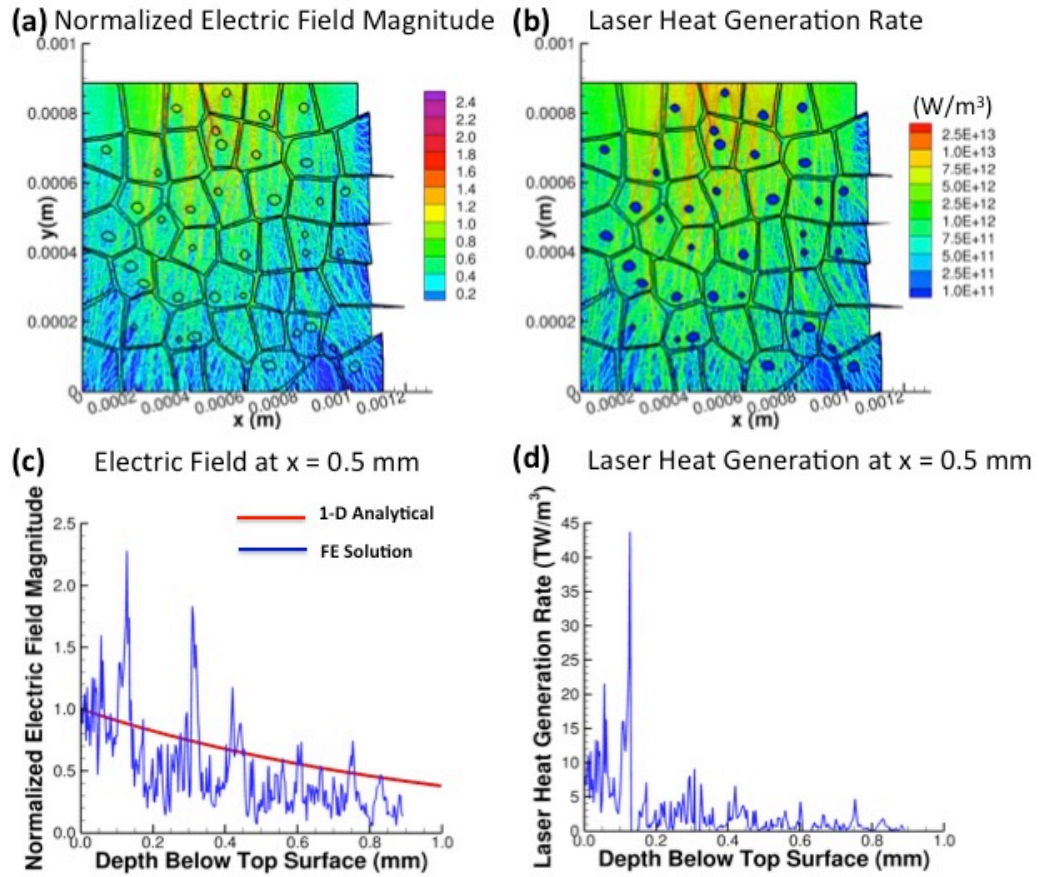


**Figure 6.5:** Electric field magnitude (normalized by the applied electric field  $E_0$ ) and laser heat generation rate for 49-grain, 10 % binder aggregate after  $10 \mu\text{s}$ . (a) Normalized electric field, (b) Volumetric laser heat generation rate, (c) Normalized electric field magnitude as a function of depth below the top surface at  $x = 0.5\text{mm}$ , (d) Volumetric laser heat generation rate as a function of depth below the top surface at  $x = 0.5\text{mm}$ .

The normalized electric field magnitude (Figure 6.5(a)) ranged from 1 – 0.4 times the applied field in most areas, but the field was more scattered in the lower grains compared to the 16-grain aggregate (Figure 6.2(a)). In this case, there were many small areas with electric field magnitude ranging from 0.2 – 0.4 times the applied field, rather than a few large areas with an electric field magnitude less than 0.2 times the applied field. Additionally, there were many localized areas in both the binder and the grains near the top surface with electric field magnitudes ranging from 1.5 – 2.2 times the applied field. These localized sites had higher magnitudes of electric field and occurred in more locations in comparison with the 16-grain aggregate (Figure 6.2(a)). This behavior can be attributed to the increased scattering of the EM wave caused by the greater number of crystal-binder interfaces and smaller grain size compared to the 16-grain aggregate. Furthermore, the electric field is localized at the void peripheries due to the larger number of voids near the top surface. The effect can also be seen in the laser heat generation rate (Figure 6.5(b)), where the laser heating follows the same general pattern as the 16-grain aggregate, but more areas of localized heating occurred.

Figure 6.5(c-d) show the normalized electric field magnitude compared to the one-dimensional prediction for homogeneous RDX (Equation 6.2) and the laser heat generation rate versus depth from the top surface at the beam center  $x = 0.5$  mm. The high number of grains and interfaces caused the electric field to be very non-uniform, with variations from the prediction for homogeneous RDX much greater than those seen in the 16-grain aggregate (Figure 6.2(c)). Local peaks up to twice the applied electric field occurred at depths close to the top surface, but the mean electric field magnitude was generally lower than the homogeneous prediction due to the large effect of scattering at the many interfaces. This

produced high laser heat generation rates within a depth of 0.1 mm from the top surface but reduced laser heating further within the material along the beam centerline (Figure 6.5(d)).

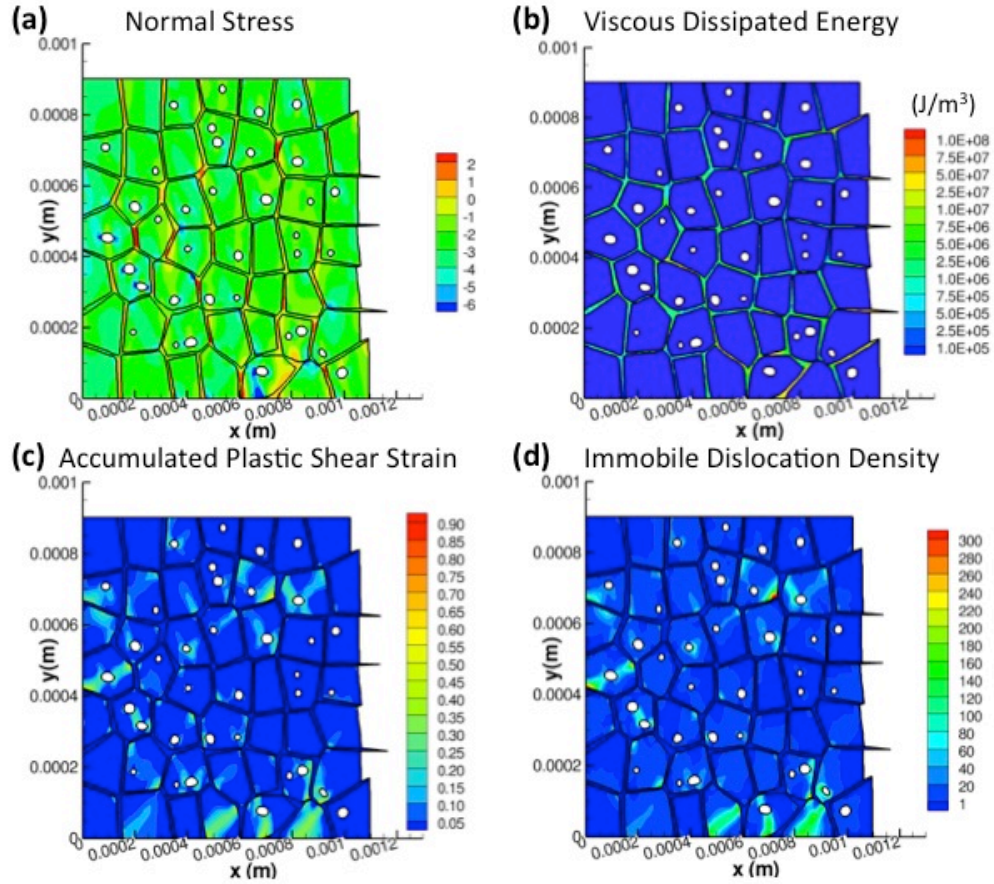


**Figure 6.6: Response of 49-grain, 10% binder aggregate after 10  $\mu$ s. (a) Normal stress (normalized by RDX yield stress), (b) Energy dissipated by viscous sliding in binder, (c) Accumulated crystalline plastic shear strain, (d) Immobile dislocation density on the most active slip system (021) [100].**

The normal stress distribution, shown in Figure 6.6(a), was generally compressive at 2 – 3 times the yield stress. High compressive stress accumulations were present in the grain corners and at the voids, and tensile stresses were present in the vertical ligaments of the binder. There were a larger number of these areas distributed throughout the microstructure than the 16-grain aggregate, due to the smaller grain size and increased number of crystal-binder interfaces. The energy dissipated by viscous sliding was most prevalent at the free

edge of the model as well as in the binder ligaments that form a band roughly  $45^\circ$  to the loading axis (Figure 6.6(b)). In comparison with the 16-grain aggregate, which had thicker binder ligaments, grain bulging from the free edge was constrained due to the thinner binder ligaments in the 49-grain aggregate.

Crystalline plastic shear strain (Figure 6.6(c)) and immobile dislocation density build-up (Figure 6.6(d)) on the most active slip system (021) [100] accumulated at the voids and grain corners, particularly in grains adjacent to binder ligaments with higher viscous energy dissipation (Figure 6.6(b)). In comparison with the 16-grain aggregate, crystalline plastic shear slip and dislocation density activity were more widely distributed and occurred at a higher number of locations. However, the maximum shear strain accumulation was 0.6, which was lower than the 16-grain aggregate by 30%. The smaller grain sizes in the 49-grain aggregate led to higher stresses, and this is due to the higher number of grain boundaries and interfaces.

Figure 6.7 illustrates how the large stress gradients at the crystal-binder interfaces led to dislocation density accumulation in these areas. By comparing the immobile dislocation density on slip system (021) [100] after 5  $\mu$ s (Figure 6.7(a)) with the response at 10  $\mu$ s (Figure 6.6(d)), the initial dislocation density accumulation at 5  $\mu$ s occurred at the crystal corners and the voids. A zoomed-in view of the normal stress distribution after 5  $\mu$ s (Figure 6.7(b)) shows the large stress gradients in these areas.

The normal stress-time history from Region 1 at the grain corner and Region 2 at the grain interior is shown in Figure 6.7(c), and the immobile dislocation density time-history is shown in Figure 6.7(d). A high stress gradient was present between tensile stress in the

binder and compressive stress in the neighboring grain corner, which led to dislocation density build-up after 4.5  $\mu\text{s}$ . Such stress gradients were not present within the interior of the grains, and consequently the immobile dislocation density build-up began at a much later time of 8.5  $\mu\text{s}$ . Similar behavior has been observed in other crystalline-amorphous heterogeneous materials, such as metallic glass laminates [64,65].

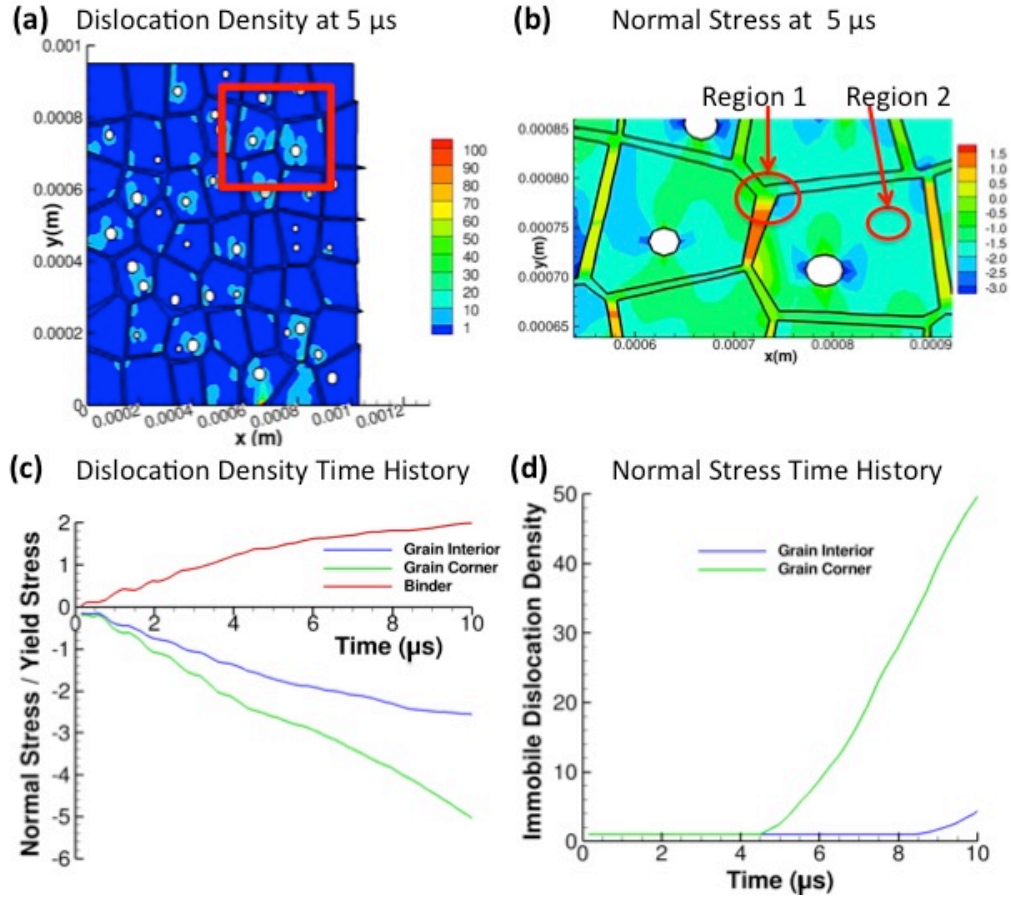


**Figure 6.7:** (a) Immobile dislocation density build-up on slip system (021) [100] after 5 $\mu\text{s}$ , (b) Zoomed-in view of normal stress distribution in boxed region at 5 $\mu\text{s}$ , (c) Normal stress–time history for circled regions, (d) Immobile dislocation density–time history on slip system (021) [100] for circled regions. All quantities are normalized by their initial values.

The total temperature accumulation that accounts for thermal conduction, laser heating, plastic work heating, viscous heating, and thermal decomposition is shown in Figure



6.8(a). There was a temperature increase of at least 1.1 times the initial temperature throughout the entire aggregate, with larger temperature increases in localized areas around the voids and binder in the lower grains. The upper grains above  $y = 0.5$  mm had temperatures 1.1 – 1.3 times the initial temperature, and the peak temperature increase occurred in the corner of one of these grains.

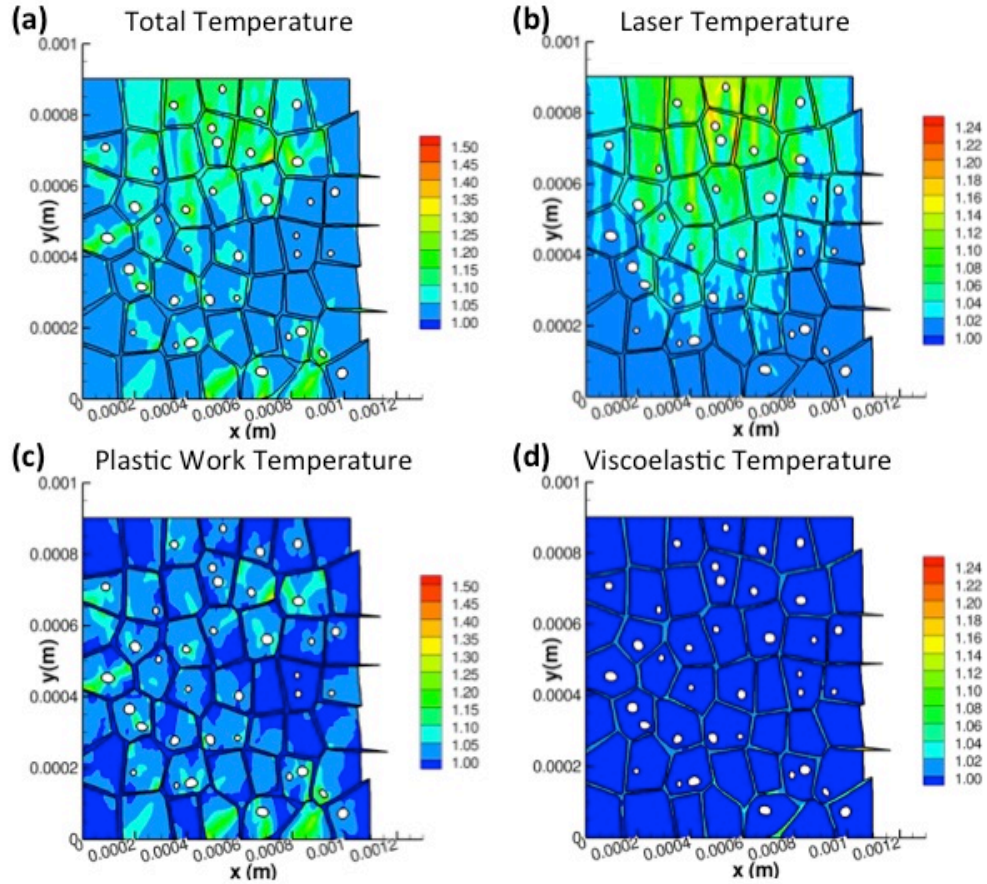


**Figure 6.8: Temperature accumulation (normalized by initial temperature) in 16-grain, 10% binder aggregate after 10  $\mu$ s. (a) Total temperature increase, (b) Temperature increase due to laser heating, (c) Temperature increase due to plastic work, (d) Temperature increase due to viscous sliding.**

The temperature increase due to laser heating (Figure 6.8(b)) occurred mostly in the upper grains. Localized areas in the binder and near the voids that correspond to areas with

electric field concentrations (Figure 6.5(a-b)) had a temperature increase up to 1.2 times the initial temperature. The temperature increase due to plastic work (Figure 6.8(c)) occurred in many locations around the grain corners and voids with magnitudes up to 1.3 times the initial temperature. The temperature increase due to viscous heating (Figure 6.8(d)) was the lowest component of the total temperature, and it occurred in areas of the binder where viscous sliding was present.

Similar to the 16-grain aggregate, laser heating increased the bulk temperature, while plastic work heating contributed additional localized temperature rise to areas with significant inelastic deformation. Neither of these mechanisms increased the temperature enough to cause significant heating from thermal decomposition. Localized areas of laser heating had higher temperatures than the 16-grain aggregate due to the increased electric field concentrations, while the temperature increases from plastic work and viscous heating decreased from the 16-grain aggregate due to lower plastic shear strain accumulation and less viscous sliding in the binder.

### ***6.2.3 Aggregate with 49 RDX grains and 30% volume fraction binder***

The normalized electric field magnitude distribution and the laser heat generation rate are shown in Figure 6.9 after a time of 10  $\mu$ s for an aggregate with 49 grains and 30% binder. The electric field is scattered throughout the aggregate in a similar pattern as the 49-grain 10% binder aggregate, with magnitudes between 1 – 0.4 times the applied field.

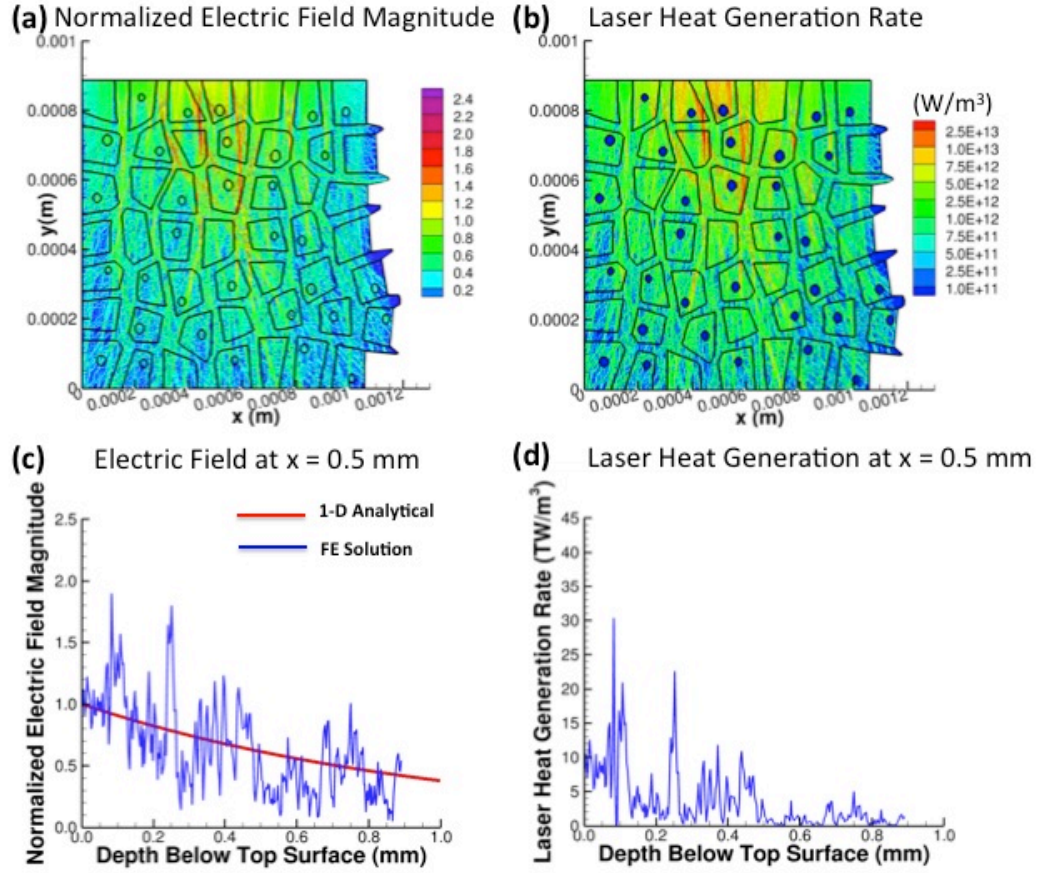


**Figure 6.9: Electric field magnitude (normalized by the applied electric field  $E_0$ ) and laser heat generation rate for 49-grain, 30 % binder aggregate after 10  $\mu s$ . (a) Normalized electric field, (b) Volumetric laser heat generation rate, (c) Normalized electric field magnitude as a function of depth below the top surface at  $x = 0.5mm$ , (d) Volumetric laser heat generation rate as a function of depth below the top surface at  $x = 0.5mm$ .**

Although the number of interfaces is the same, the thicker binder ligaments in this aggregate concentrate the propagating EM wave into linear regions with electric field magnitude between 1.4 – 2.4 times the applied field. These regions are more continuous than both the aggregates with 10% binder (Figure 6.2 and Figure 6.5) and they also extend deeper into the model with higher magnitudes. Additionally, viscous sliding in the binder caused some of the grains to bulge from the free surface, and the changes in microstructure geometry



redirected the propagating EM wave such that the most densely concentrated electric fields occurred slightly to the right of the applied beam center

The laser heat generation rate (Figure 6.9(b)) shows these effects, as areas with high laser heat generation extend deep into the grains where the electric field is concentrated. At the applied beam center  $x = 0.5$  mm, both the normalized electric field magnitude (Figure 6.9(c)) and the laser heat generation rate (Figure 6.9(d)) show the general trend of decaying magnitude with increasing depth below the top surface. Both quantities also show large variations similar in number and magnitude to the 49-grains 10% binder aggregate and much more pronounced than the 16-grain 10% binder aggregate.

The normal stress distribution is shown in Figure 6.10(a) normalized by the RDX yield stress. Most grains exhibited a compressive stress 1 – 2 times the yield stress, which is lower than the stress states that were present in the aggregates with 10 % binder. Additionally, there were no areas with high compressive stresses. The vertical binder ligaments had tensile stresses present, but these were also lower in magnitude than in aggregates with 10% binder. Viscous sliding occurred and dissipated energy throughout the binder (Figure 6.10(b)), and there were no localized regions where the energy dissipation was particularly concentrated. The thick binder ligaments allowed viscous sliding at the free edge, and several of the grains bulged outward. Accumulated plastic shear strain (Figure 6.10(c)) and immobile dislocation density activity on the most active slip system (Figure 6.10(d)) was very low and only occurred in the grain corners.

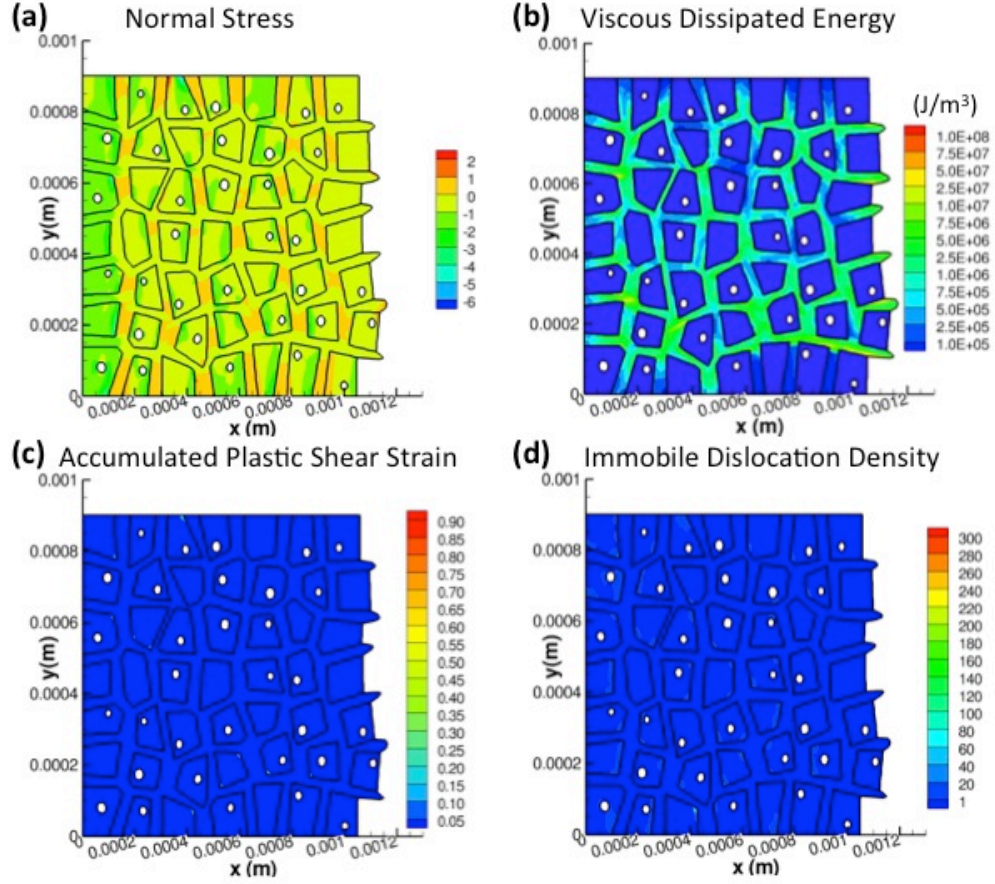


**Figure 6.10: Response of 49-grain, 30% binder aggregate after 10  $\mu$ s. (a) Normal stress (normalized by RDX yield stress), (b) Energy dissipated by viscous sliding in binder, (c) Accumulated plastic shear strain, (d) Immobile dislocation density on the most active slip system (021) [100].**

The total temperature accumulation normalized by the initial temperature is shown in Figure 6.11(a). Similar to the aggregates with 10% binder, there was a large area with temperature rise between 1 – 1.3 times the initial temperature in the upper grains. However, there were no additional localized areas of temperature build-up and the maximum temperature increase of 1.35 times the initial temperature was lower than the 16-grain 10% binder and 49-grain 10% binder aggregates.

The temperature increase due to laser heating (Figure 6.11(b)) occurred in a large area of the grains with values from 1 – 1.5 in the central grains. The area heated to these

temperatures was shifted slightly to the right of the applied beam center ( $x = 0.5 \text{ mm}$ ) as large geometry changes due to binder sliding redirected the EM wave and areas with largest laser heat generation rate (Figure 6.9). Areas with localized temperature increase between 1.2 – 1.3 times the initial temperature are larger in size than both aggregates with 10% binder due to the larger areas of high electric field present.

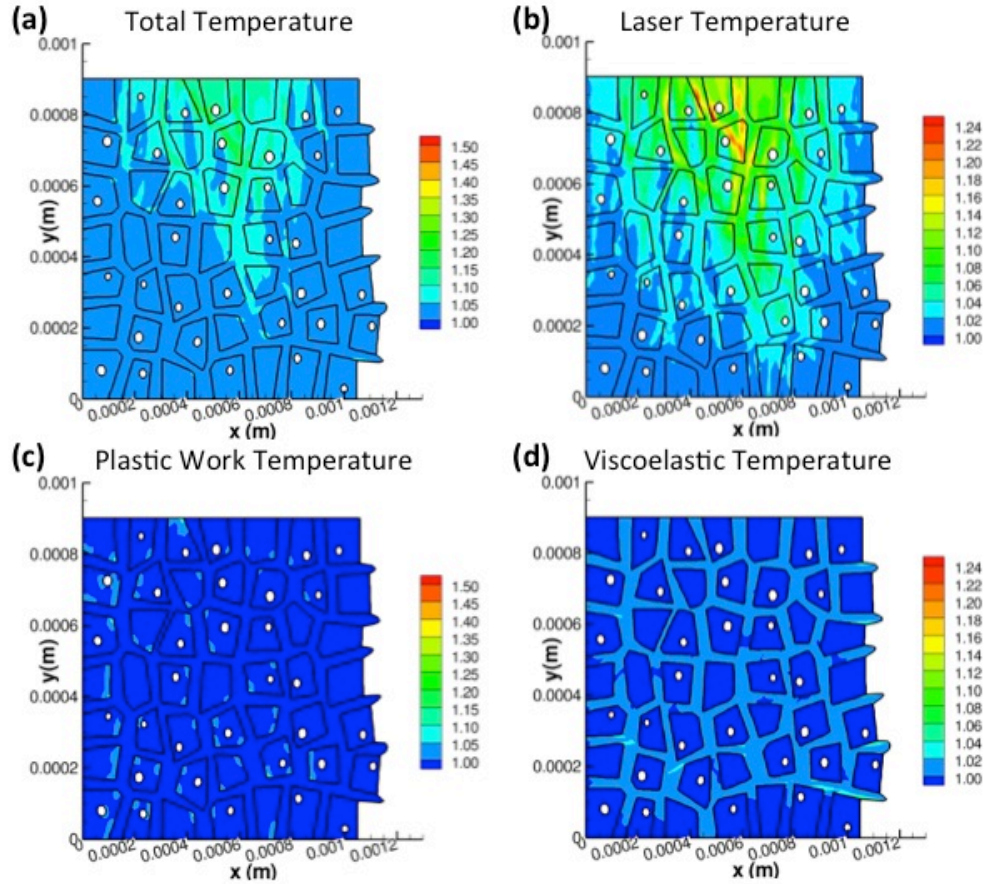


**Figure 6.11: Temperature accumulation (normalized by initial temperature) in 49-grain, 30% binder aggregate after 10 μs. (a) Total temperature increase, (b) Temperature increase due to laser heating, (c) Temperature increase due to plastic work, (d) Temperature increase due to viscous sliding.**

The temperature increase due to plastic work heating (Figure 6.11(c)) occurred only at the grain corners and the crystal-binder interface and was less than 1.1 times the initial temperature. Temperature increase due to viscous heating (Figure 6.11(d)) was distributed

throughout the binder with small concentrations at the free edge where the largest sliding motion occurred. The temperature increase from all combined heat sources (Figure 6.11(a)) was governed completely by laser heating in this aggregate and was not high enough to cause significant heating from thermal decomposition.

#### 6.2.4 Binder Volume Fraction and Grain Size Effects

The laser-induced temperature increase as a function of depth along the applied beam center  $x = 0.5$  mm is shown in Figure 6.12 for aggregates of 16 grains with 10% binder, 49 grains with 10% binder, and 49 grains with 30% binder.

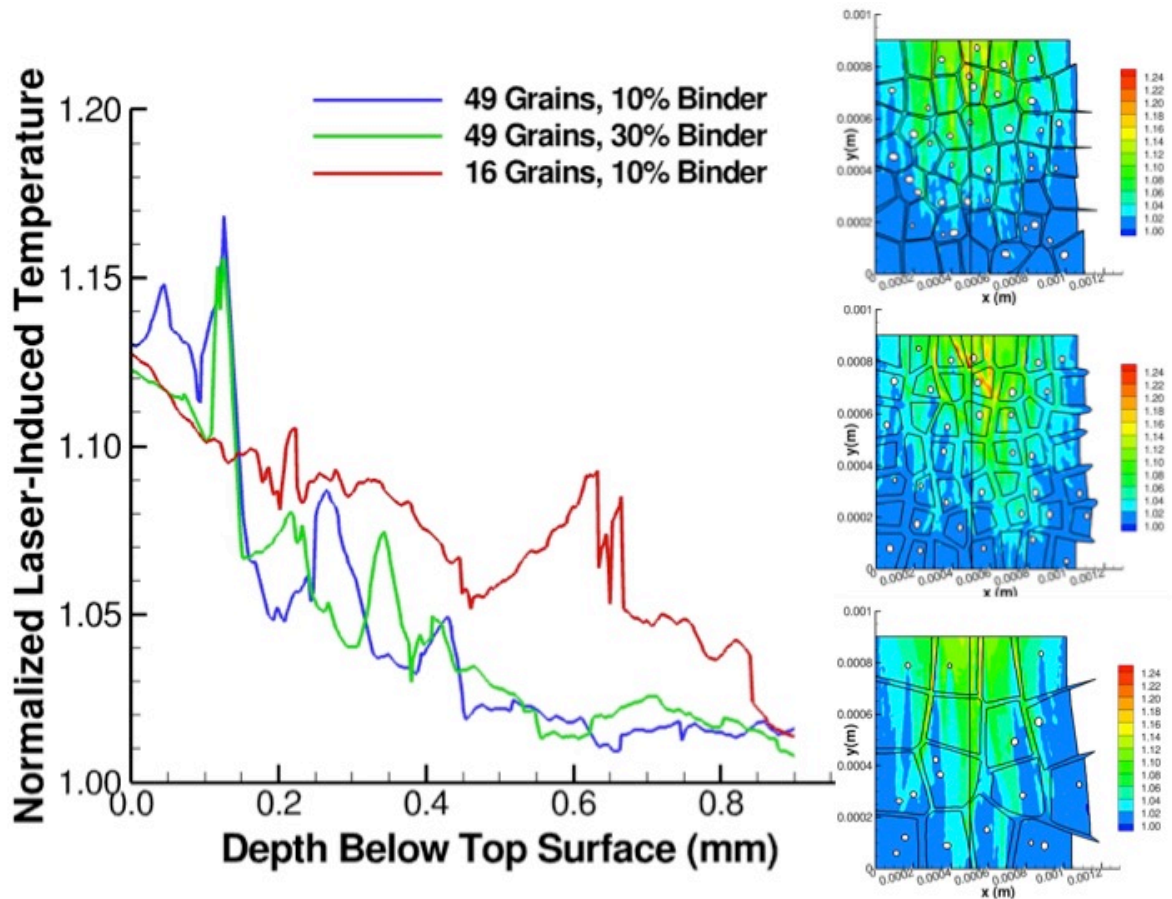


Figure 6.12: Comparison of laser-induced temperature increase vs. depth from top surface at  $x = 0.5$  mm in various aggregates. The full spatial laser-induced temperature distributions are shown on the right. All temperatures are normalized by the initial temperature and shown after time of 10  $\mu$ s.

Although the maximum laser induced temperature did not necessarily occur at the applied beam center, Figure 6.12 gives a good idea of the differences in laser heating profile as a function of depth obtained from each aggregate. The large number of interfaces and smaller grain size present in both the 49-grain aggregates resulted in large temperature variations near the top surface. This is directly related to the EM wave scattering and high values of concentrated electric field present in these aggregates (Figure 6.5 and Figure 6.9).

Both 49-grain aggregates had lower laser-induced temperatures at depths further within the material, but this occurred for different reasons in each case. In the 49-grain 10% binder aggregate, the grains at the bottom of the aggregate were effectively shielded from higher laser heating due to the large amount of electric field scattering and absorption by the RDX grains. In the 49-grain 30% binder aggregate, the larger volume of viscous binder resulted in significant sliding. This consequently redirected the propagating EM wave and shifted the higher laser-induced temperature increases to the right of the applied beam center. The larger grain size and fewer interfaces present in the 16-grain aggregate allowed smoother propagation of the EM wave with less scattering. This resulted in fewer temperature variations and higher temperature increases at depths further from the top surface.

A comparison of the normal stress vs. nominal strain response for several aggregates is shown in Figure 6.13. The binder volume fraction clearly governed the aggregate behavior as cases with 30% binder had much lower stresses than the cases with 10% binder. The binder ligaments in aggregates with 30% binder were approximately 50  $\mu\text{m}$  thick, which made sliding in the binder the preferred deformation mechanism and mitigated plasticity

build-up within the RDX grains. For aggregates with 30% binder, there was little crystalline shear slip accumulation, and the global stress-strain response was entirely governed by binder sliding.

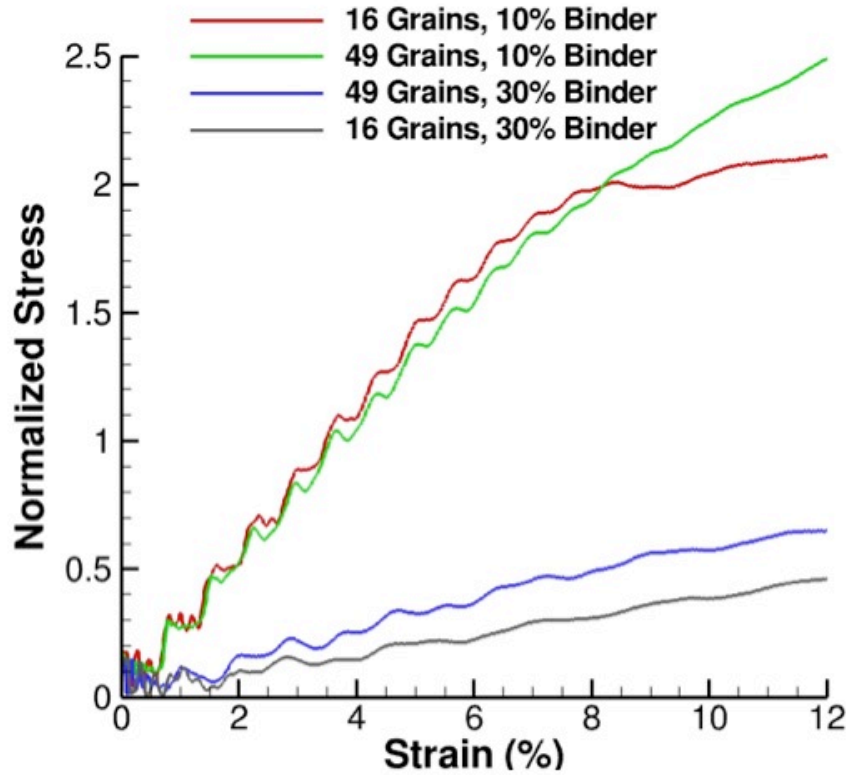


**Figure 6.13: Nominal stress-strain curves for various aggregates. All stresses are normalized by the RDX yield stress.**

### 6.3 Summary

A non-linear finite-element formulation that couples EM wave propagation and heat generation with dislocation-density based crystalline plasticity and viscoelastic constitutive formulations was used to investigate the response of RDX-estane aggregates to laser irradiation and high strain rate loading conditions.

For the 16-grain aggregate with average grain sizes of 230  $\mu\text{m}$  and 10% binder volume fraction, the electric field produced by the laser decayed gradually with depth. EM reflections and refractions at the crystal-binder interfaces resulted in localized areas with high electric field magnitudes. The crystal-binder interfaces were also sites of large stress gradients between tension in the vertical ligaments of the binder and high compressive stresses in the crystal corners that resulted in plastic shear strain and dislocation density accumulation. Viscous sliding in the binder resulted in lateral grain sliding and grain bulging from the free surface. The temperature build-up was associated primarily with heating from laser energy absorption and additional localized heating in areas with plastic work and viscous sliding in the binder.

For the 49-grain aggregate with average grain sizes of 135  $\mu\text{m}$  and 10% binder volume fraction, the greater number of crystal-binder interfaces caused more internal reflections of the EM wave and higher electric field magnitudes than for the 16-grain aggregate. The larger number of interfaces also resulted in stress, crystalline shear strain and dislocation density accumulations that were more spatially distributed. However, the smaller grain sizes constrained plasticity accumulation within RDX crystals. Additionally, the thin binder ligaments were more constrained, in comparison with the 16-grain aggregate, by the surrounding RDX grains, which prevented grain bulging from the free edge.

Aggregates with 30% binder volume fraction exhibited lower overall global stresses, as viscous sliding in the thick binder ligaments mitigated plasticity within the grains and resulted in grain bulging from the free surface. This sliding also redirected the laser EM

wave, such that the maximum laser induced temperature build-up occurred off-center from the applied beam.

In all aggregates, the mismatch of electrical and mechanical properties and behavior at the crystal-binder interfaces resulted in electric field localization, high stress gradients, dislocation density and crystalline shear slip accumulation. The combined effects of adiabatic plastic work heating, laser heating, and viscous dissipative heating resulted in non-uniform temperature distributions throughout the aggregates with high local temperatures in areas with concentrated electric field or plastic shear slip. Results from this study underscore the need to couple fundamental phenomena such as electromagnetism and mechanical behavior for laser interactions with heterogeneous materials.



## **CHAPTER 7: Heterogeneous Crystal Size Distribution, Crystalline-Crystalline, and Crystalline-Amorphous Interfaces in RDX-Estane Energetic Aggregates**

### **7.1 Introduction**

Energetic aggregates contain a wide range of crystal sizes, varying from less than 10  $\mu\text{m}$  to over 500  $\mu\text{m}$  [15,66]. This results in a complex microstructure consisting of large crystals surrounded by polymer binder with many smaller crystals embedded within the polymer binder ligaments. The addition of the smaller crystals embedded in the binder can greatly affect the aggregate response to incident laser energy and high strain rate loads, through viscoelastic deformation of binder ligaments, interaction between large and small crystals, geometrically necessary dislocation density build up, high stress gradients at the crystal-crystal and crystal-binder interfaces, and scattering of the EM wave by the small crystals.

The quasi-static and the coupled EM-thermo-mechanical response to high strain rate loads with laser irradiation has been investigated for RDX-estane aggregates containing both large grains and small crystals embedded in the binder ligaments. Aggregates with and without small crystals embedded in the binder were studied to understand the effects of crystal size distribution and crystal-crystal and crystal-binder interfaces present in real energetic aggregates. Additionally, geometrically necessary dislocation densities (GNDs) were calculated to characterize the effects of shear strain localization and gradients at the interfaces.

## 7.2 Results

A model consisting of four RDX crystals separated by ligaments of estane polymer binder was used to study the effect of crystal-crystal and crystal-binder interfaces present in energetic aggregates. The large crystalline grains were approximately 425  $\mu\text{m}$  in length and the binder ligaments were 150  $\mu\text{m}$  wide for a global aggregate size of 1mm x 1mm. Smaller crystals ranging in size between 20  $\mu\text{m}$  – 150  $\mu\text{m}$  with arbitrary shape were embedded within the binder ligaments. In this aggregate, the large grains occupied approximately 70% volume fraction, the small grains occupied approximately 10% volume fraction, and the binder occupied approximately 20% volume fraction. A second aggregate with the same large grains and binder thickness, but no smaller crystals within the binder ligaments, was also studied. In the aggregate without small crystals, the volume fraction of the large grains was 70%, and the binder volume fraction was 30 %. The RDX crystals had randomly generated orientations between  $-15^\circ$  and  $15^\circ$  from the reference axes, such that the maximum angular misorientations at the crystalline-crystalline grain boundaries was  $30^\circ$ .

Based on Gallagher et al. [10], the RDX crystals were assumed to have the three independent slip systems of (010) [001], (021) [100],  $(02\bar{1})$  [100]. The mechanical, thermal, and electrical properties used for the RDX crystals are shown in Table 7.1. The estane binder was modeled as a viscoelastic material, where properties for each Maxwell element were obtained from the experimental data of Mas et al. [46]. The thermal and electrical properties used for the estane binder are shown in Table 7.1.

**Table 7.1: Material Properties of RDX Crystals and Estane Binder Materials.**

	RDX	estane
Density ( $\frac{kg}{m^3}$ )	1820 [9]	1190[46]
Yield Stress (MPa)	300[60]	--
Elastic Modulus (GPa)	18.4 [9]	--
Poisson's Ratio	0.22[15]	0.499[14]
Strain Rate Exponent	0.02**	--
Thermal Softening Exponent	0.1**	--
Initial Immobile Dislocation Density	$1 \times 10^{12}$ **	--
Initial Mobile Dislocation Density	$1 \times 10^{10}$ **	--
Thermal Conductivity ( $\frac{W}{m K}$ )	0.29 [6]	0.14[61]
Specific Heat ( $c_p$ ) ( $\frac{J}{kg K}$ )	1260[15]	1500[14]
Refractive Index Real Component $n$	1.5*[57]	1.7*[62,63]
Refractive Index Imaginary Component $k$	0.000834*[32,57]	0.030400*[32]

\*Values estimated at wavelength of 10.3  $\mu m$

\*\*Properties assumed based on other crystalline materials due to lack of experimental data for RDX

The thermo-mechanical domain was modeled using symmetry boundary conditions for plane strain loading. For quasi-static loading conditions without laser irradiation, a compressive displacement boundary condition was applied to the top surface for a strain rate of  $10^{-3} s^{-1}$  and no coupling to the electromagnetic domain was considered (Figure 7.1(a)). For dynamic loading conditions with laser irradiation, the compressive displacement boundary condition was applied to the top surface for a much higher strain rate of  $10^3 s^{-1}$  and the full coupling to the electromagnetic domain was employed (Figure 7.1(b)).

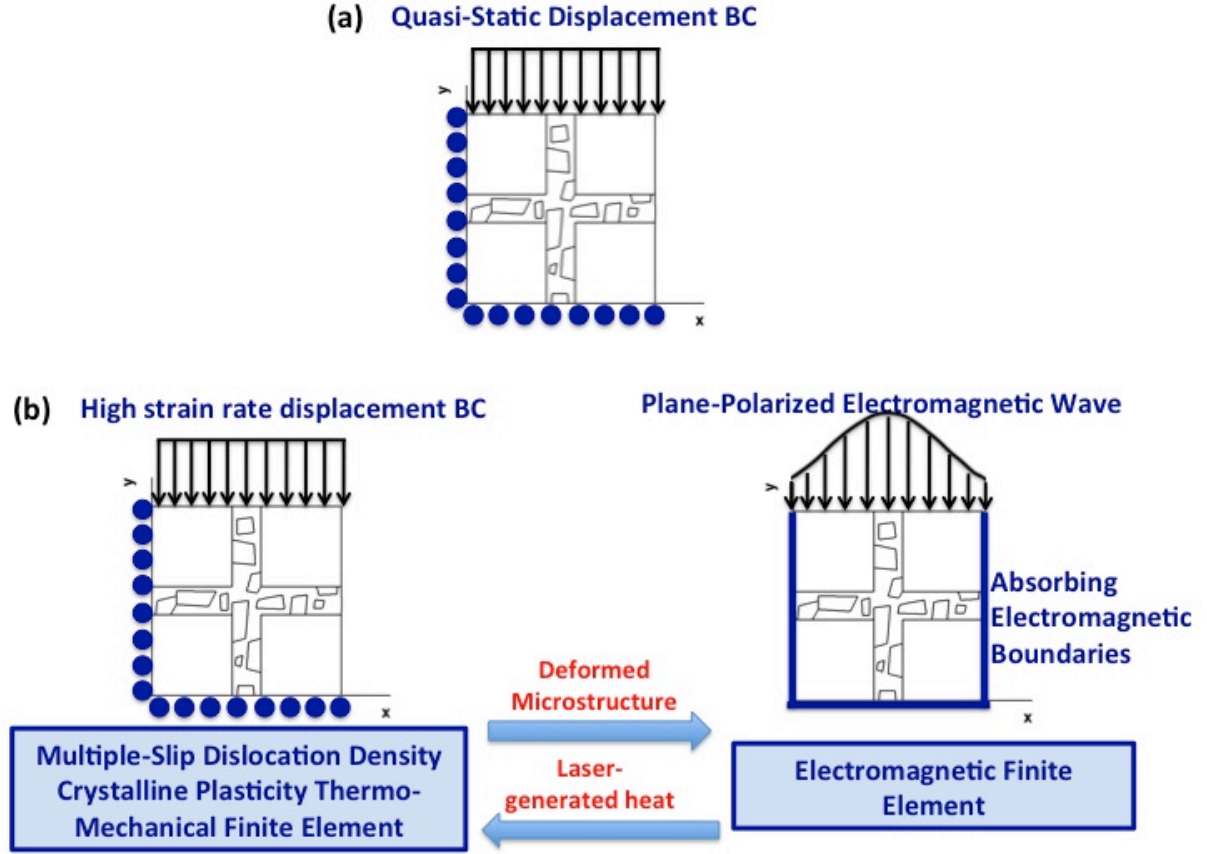


**Figure 7.1: The RDX-estane aggregate with boundary conditions and loading conditions for (a) Quasi-static loading without laser, (b) Dynamic high strain rate load with laser irradiation.**

For the electromagnetic domain, the laser energy was applied to the top surface as a Gaussian beam centered at  $x_c = 0.5$  mm with a radius ( $r$ ) of 0.5 mm. The beam was polarized in the out-of-plane direction ( $\vec{z}$ ) and specified to propagate in the  $y$ -direction. The applied electric field ( $\vec{E}$ ) is given as a function of beam dimensions and local  $x$ -coordinate ( $x$ ) as

$$\vec{E} = \left( E_0 \exp \left( -\frac{(x-x_c)^2}{r^2} \right) \right) \vec{z}, \quad (7.1)$$

where the electric field magnitude at the beam center ( $E_0$ ) was specified as 0.87 MV/m. This corresponds to an intensity of  $1 \times 10^5$  W/cm<sup>2</sup>. Perfectly matched layers were used on the sides and lower surface of the EM domain to reduce artificial reflections of the EM wave

from the boundaries. A wavelength where EM energy is weakly absorbed in both RDX and estane was investigated (estimated at 10.3  $\mu\text{m}$ ), and the assumed material refractive index values are shown in Table 7.1.

### 7.2.1 Quasi-Static Response of Aggregate with Small Crystals in Binder

Figure 7.2 shows the stress and pressure distributions for the aggregate containing small crystals embedded in the binder after compression to 8% nominal strain at a quasi-static strain rate of  $10^{-3} \text{ s}^{-1}$ .

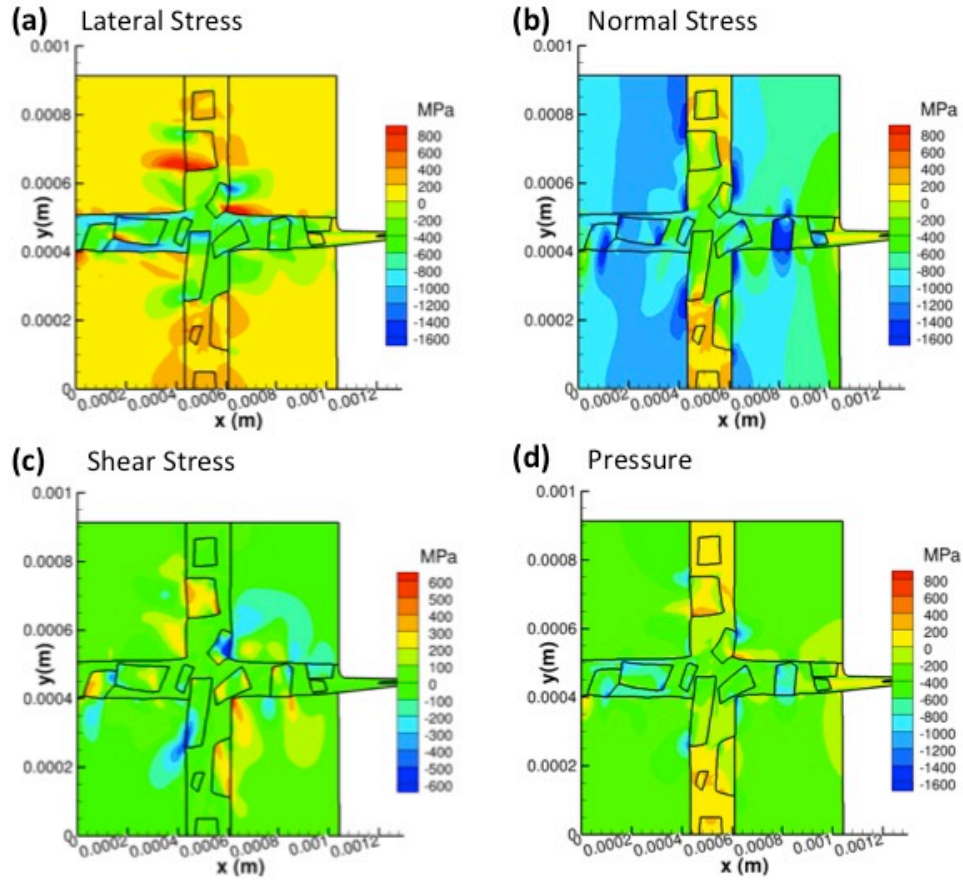


**Figure 7.2: Stress distribution at 8 % nominal strain for quasi-static compression. (a) Lateral stress, (b) Normal stress, (c) Shear stress, (d) Hydrostatic pressure.**

The lateral stresses (Figure 7.2(a)) were generally tensile throughout the large grain interiors, but large stress gradients were present at the crystal-binder interfaces and throughout the polymer binder. Compressive lateral stresses built up in the horizontal binder ligaments in between the large grains and the small crystals where the binder thickness was effectively reduced by the presence of the embedded small crystals.

The normal stresses (Figure 7.2(b)) were generally compressive throughout the large grains, but the vertical ligaments of the binder had some tensile stress build up, particularly in the thin sections of binder between small and large crystals. This resulted as the horizontal ligaments bulged outward at the free edge. Very high compressive normal stress accumulated in the small crystals embedded in the horizontal binder ligaments and also extended into the larger grains at these crystal-crystal interfaces. Shear stresses (Figure 7.2(c)) were primarily concentrated at the crystal-crystal interfaces between the small and large crystals, as these locations also had large gradients in normal and lateral stress. High hydrostatic pressures (Figure 7.2(d)) also developed in the smaller crystals embedded within the binder ligaments, with large gradients between compressive and tensile pressures at regions where the small crystals, larger crystals, and polymer meet. This stress state resulted from the small crystals pushing against the larger grains as the polymer binder deforms and resulted in both tensile and compressive stresses at the crystal-crystal and crystal-binder interfaces.

Figure 7.3 shows the stress distribution along a horizontal line at  $y = 0.6$  mm for an aggregate with the small crystals embedded in the binder (Figure 7.3(a)) compared with an aggregate without the small crystals (Figure 7.3(b)). In both aggregates, there is a large

mismatch in normal stress at the crystal-binder interface from compressive stress within the large grains to low tensile stresses in the binder. However, the magnitude of this mismatch is much greater in the aggregate containing small crystals, and the stress state is also much more non-uniform within the large grains.

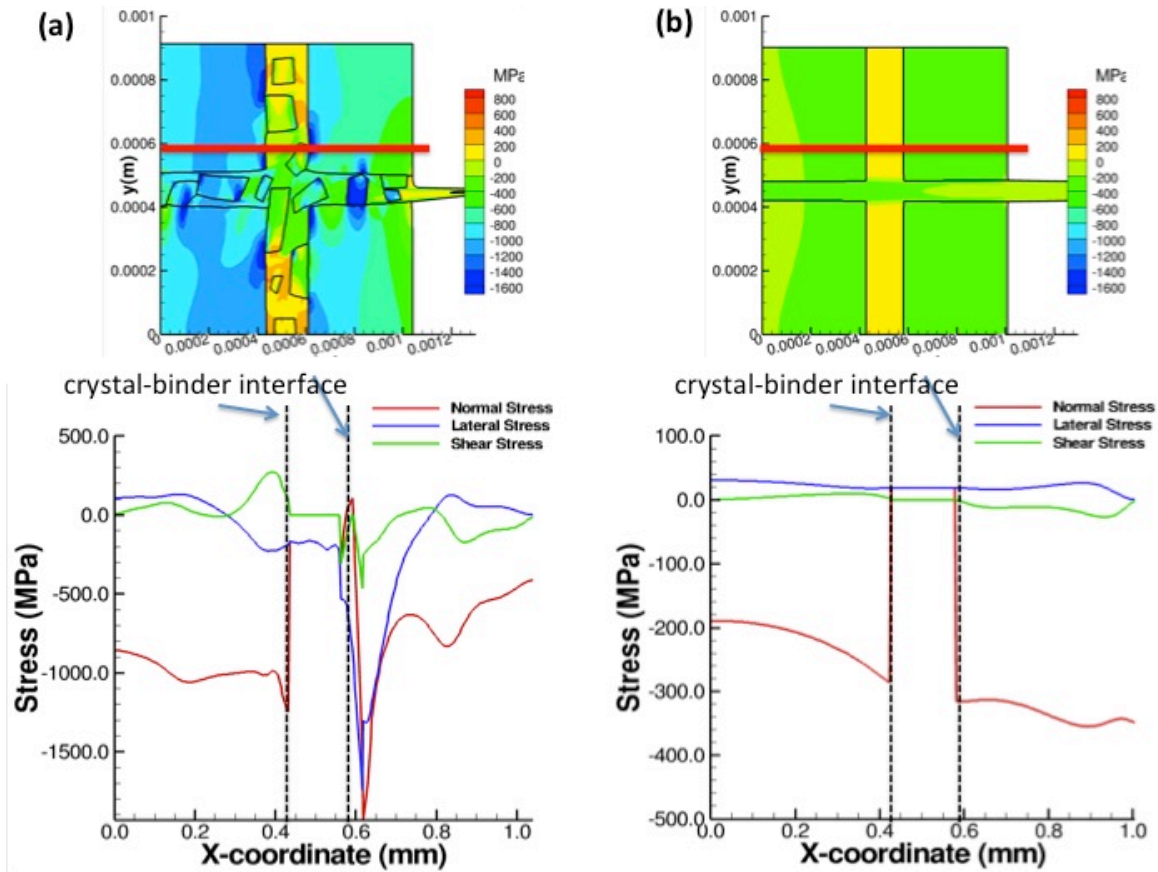


**Figure 7.3: Stress distribution along horizontal line at  $y=0.6 \text{ mm}$  for (a) Aggregate with small crystals embedded in the binder, (b) Aggregate without any small crystals.**

The lateral stress was tensile in the aggregate without small crystals and showed no mismatch between the large grains and binder. When small crystals were present in the binder, however, the lateral stresses were much less uniform, including an area with very high compressive stress at the interface between a large crystal, small crystal, and binder at  $x = 0.6 \text{ mm}$  (Figure 7.3(a)). Much greater variation was seen in the shear stress distribution as

well when small crystals were present in the aggregate. This shows that the addition of small crystals embedded in the binder ligaments greatly increased the magnitude of stresses present in the aggregate and also resulted in a much more non-uniform stress state.

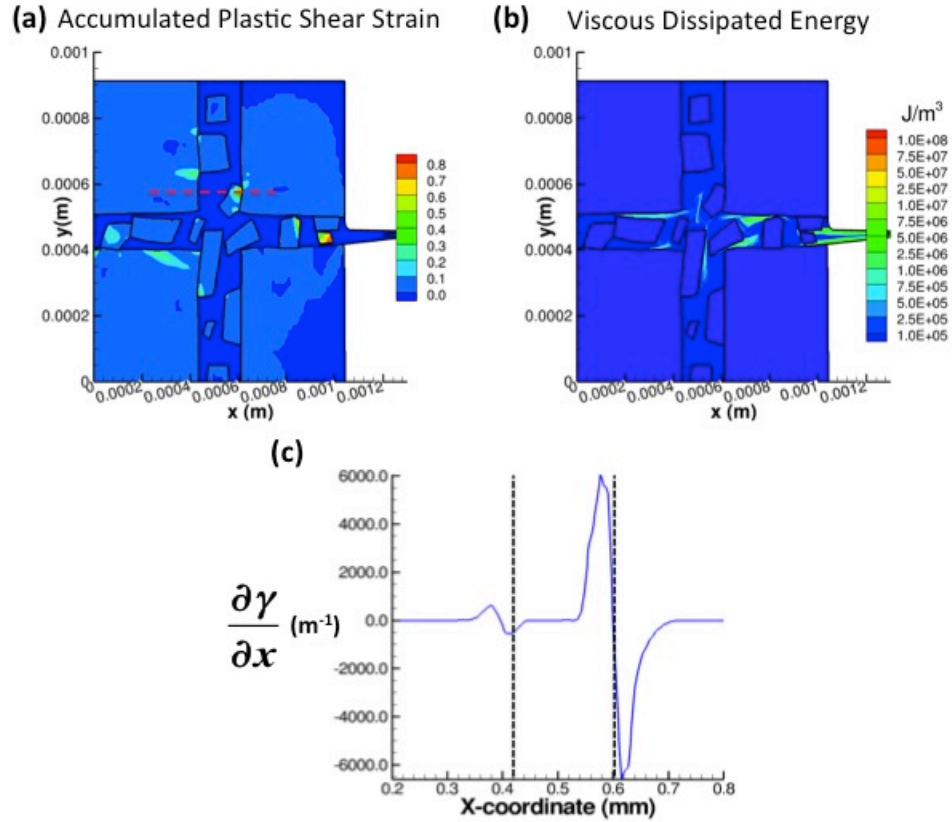


**Figure 7.4: Inelastic response at 8% nominal strain for quasi-static compression. (a) Accumulated crystalline plastic shear strain, (b) Energy dissipated by viscous sliding in binder, (c) Gradient of accumulated plastic shear strain,  $\frac{\partial \gamma}{\partial x}$ , along the dashed line in (4a). Dashed lines indicate the location of the large grain edges.**

As a result of the large stresses and stress gradients present in the aggregate containing small crystals, crystalline plastic shear strain (Figure 7.4(a)) accumulated at the corners of the small crystals at the interfaces with large RDX crystals and extended into the interior of large RDX crystals. The energy dissipated by viscous sliding in the binder (Figure 7.4(b)) was concentrated in areas of binder between two small crystals or between a small crystal and large crystal within the horizontal binder ligaments. In these regions, the



thickness of the binder ligament was effectively reduced and the viscous sliding mechanism was prevalent.

The localized accumulation of crystalline plastic shear slip resulted in large shear slip gradients at the interface region between large and small crystals. This is illustrated by Figure 7.4(c), which plots the gradient in the x-direction of accumulated plastic shear slip along the horizontal line in Figure 7.4(a). Both positive and negative gradients are present as the line crosses the small crystal embedded in the binder at  $x = 0.5 - 0.6$  mm where large changes in slip accumulation occurred over a length scale on the order of  $10 - 100$   $\mu\text{m}$ .

Dislocation activity for both immobile (Figure 7.5(a)) and mobile (Figure 7.5(b)) statistically stored dislocation densities (SSD) accumulated primarily on the slip system (010) [001] in areas with high shear slip at the crystal-crystal interfaces between small and large RDX grains. The other two slip systems both had less than two times the initial immobile dislocation density.

Additionally, geometrically necessary dislocation densities (GND) accumulate to accommodate lattice misorientations that occur due to large gradients of plastic slip [67,68]. Edge GND density  $\rho_{GND,e}^{(\alpha)}$  form due to gradients of plastic slip along the slip direction ( $\vec{s}^{(\alpha)}$ ) of slip system  $\alpha$  as

$$\rho_{GND,e}^{(\alpha)} = -\frac{1}{b^{(\alpha)}} \vec{s}^{(\alpha)} \cdot \nabla \gamma^{(\alpha)}. \quad (7.2)$$

Screw GND of density  $\rho_{GND,s}^{(\alpha)}$  form due to gradients of plastic slip along the dislocation line vector ( $\vec{l}^{(\alpha)}$ ) as

$$\rho_{GND,s}^{(\alpha)} = -\frac{1}{b^{(\alpha)}} \vec{l}^{(\alpha)} \cdot \nabla \gamma^{(\alpha)}. \quad (7.3)$$

The plastic strain gradients in the normal direction ( $\vec{n}^{(\alpha)}$ ) do not contribute to the GND formation [69]. The GND were present in both edge (Figure 7.5(c)) and screw (Figure 7.5(d)) type on the slip system (010) [001], with very little activity on the other two slip systems. The GND densities are primarily of edge type and are roughly an order of magnitude less than the statistically stored dislocation densities (Figure 7.5(a,b)).

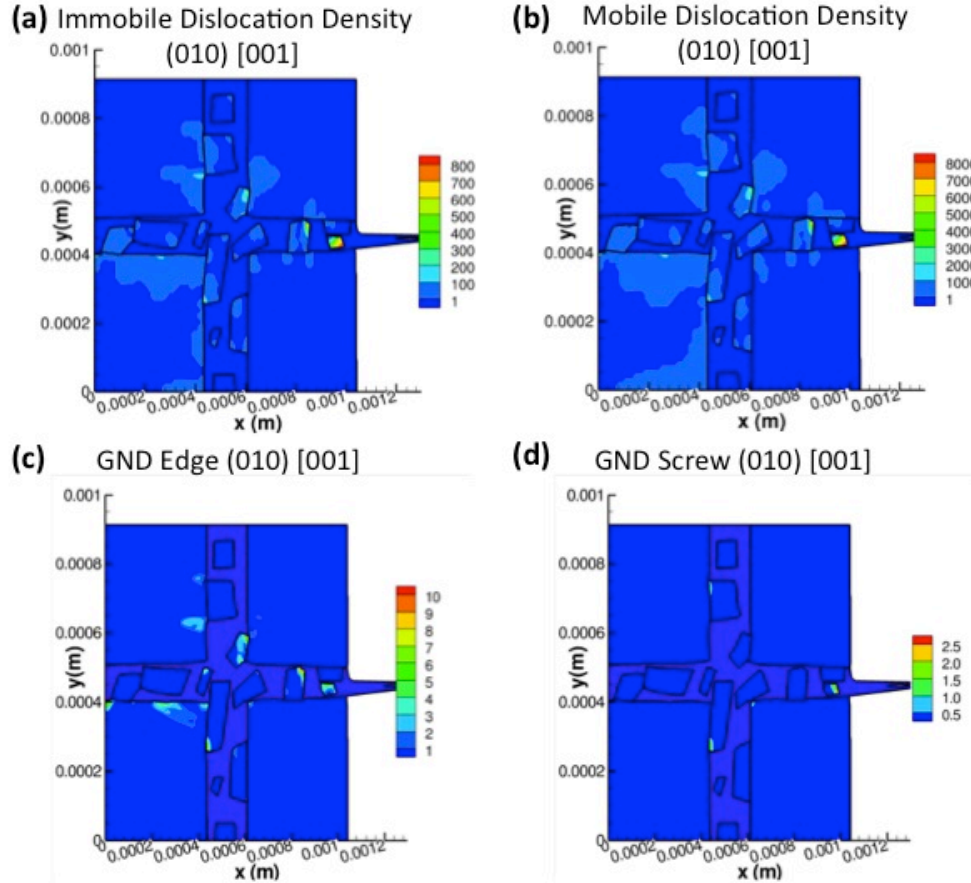


**Figure 7.5: Dislocation density activity on the most active slip system (010) [001] normalized by the initial immobile dislocation density of  $1 \times 10^{12} \text{ m}^{-2}$ . (a) SSD Immobile dislocation density, (b) SSD Mobile dislocation density, (c) Edge GND, (d) Screw GND.**

Similar to the SSD, the GND form in areas of high shear slip at the crystal-crystal interfaces between large and small crystals. However, since GND are formed to accommodate lattice mismatches produced by the shear slip gradient, this type of dislocation

density extends into the grain interiors following lines of high shear slip gradient between slipped and undeformed crystalline material. While SSD accumulation was the dominant form of dislocation activity, the high shear slip gradients resulted in GND formation that was an additional pathway for deformation at the crystal-crystal and crystal-binder interfaces.

The crystal-binder and crystal-crystal interfaces are locations of high stresses, stress gradients, crystalline shear slip and dislocation density build up of both SSD and GND types. Figure 7.6 shows a comparison of stress gradients and GND build up along a horizontal line traversing the crystal-binder and crystal-crystal interfaces (Figure 7.6(a)). The dashed vertical lines indicate the location of the binder ligament edges.

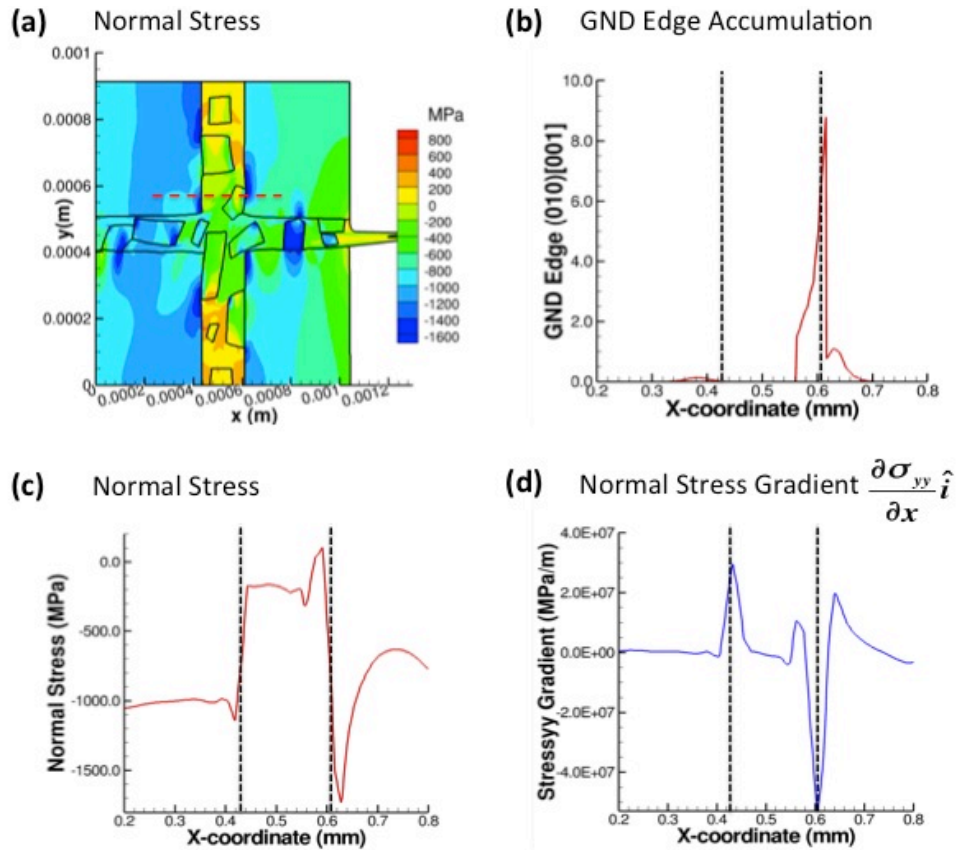


**Figure 7.6:** (a) Spatial location of horizontal lineplots for (b-d) across binder ligament at  $y = 0.6\text{mm}$ , (b) GND accumulation as a function of x-coordinate, (c) Normal stress as a function of x-coordinate, (d) Normal stress gradient in x-direction as a function of x-coordinate. Dashed lines indicate the location of the large grain edges.

The GND accumulation (Figure 7.6(b)) is concentrated at the interface between a small crystal embedded in the binder and the large grain at  $x = 0.6\text{mm}$ , which is also a location with high shear slip gradients (Figure 7.4(c)). This GND accumulation can lead to hardening at the crystal-crystal interface and potentially act as a strengthening mechanism for the aggregate [69].

However, the normal stress (Figure 7.6(c)) shows large variations at the crystal-binder and crystal-crystal interfaces between a high compressive stress in the large crystals and a much lower stress in the binder. This produced stress gradients (Figure 7.6(d)) with very high magnitude at the interfaces, which resulted from the large change in stress over spatial length scales on the order of  $10 - 100\text{ }\mu\text{m}$ . It is hypothesized that such high stress gradients over small length scales could lead to crack nucleation, should the stress gradient at the interface exceed some critical value. As such, there were competing effects of hardening due to GND and SSD dislocation accumulation and potential failure due to high stress gradients at the crystal-binder and crystal-crystal interfaces.

### ***7.2.2 High Strain Rate Coupled EM-Thermo-Mechanical Response of Aggregate with Small Crystals in the Binder***

Figure 7.7 shows the electric field and laser heat generation rate for the aggregate with small crystals embedded in the binder after  $2.5\text{ }\mu\text{s}$  of applied laser energy and high strain rate compression for a strain rate of  $10^{-3}\text{ s}^{-1}$ . The electric field is normalized by the incident electric field (Figure 7.7(a)) and is generally reduced to between  $0.8 - 0.6$  times the incident field throughout the large crystals as some of the EM energy is absorbed. The small crystals within the binder ligaments caused local scattering of the EM wave and electric field concentrations up to  $1.8$  times the incident electric field within the binder ligaments. This is

due to the mismatch of refractive index between the crystals and binder materials, which caused internal reflection and refraction of the EM wave at each crystal-binder interface. As a result, the electric field in the large crystals below the horizontal binder ligament is more disrupted and less uniform than the electric field in the upper grains.

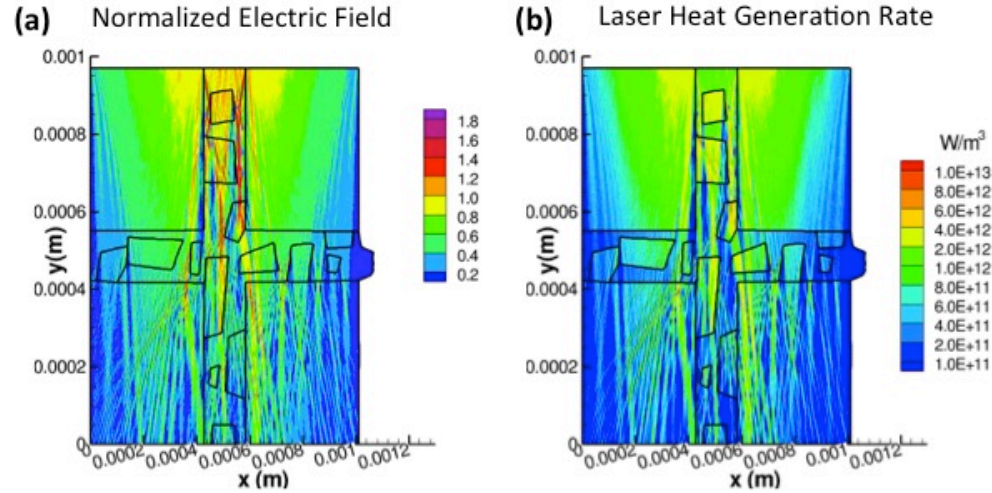


**Figure 7.7: EM response of aggregate with small crystals after 2.5  $\mu$ s for dynamic compression at strain rate of  $10^3 \text{ s}^{-1}$ . (a) Electric field magnitude normalized by the applied electric field, (b) Volumetric laser heat generation rate.**

The laser heat generation rate (Figure 7.7(b)) is concentrated in the two large grains above the horizontal binder ligaments. Since the absorption coefficient of RDX is slightly higher than that of estane at this wavelength, the small crystals embedded within the binder had higher laser heat generation rates than the binder. Some of these embedded small crystals had an even higher laser heat generation rate where an electric field concentration occurred, since the laser heat generation is the product of electric field intensity and material absorption coefficient. The laser heat generation rate in the large crystals below the horizontal binder ligaments was much lower and less uniform due to the reduced electric field present in these crystals.

Figure 7.8 shows the coupled response of the aggregate with the small crystals in the binder after 2.5  $\mu\text{s}$  to applied laser energy and high strain rate compression for a strain rate of  $10^{-3} \text{ s}^{-1}$ .

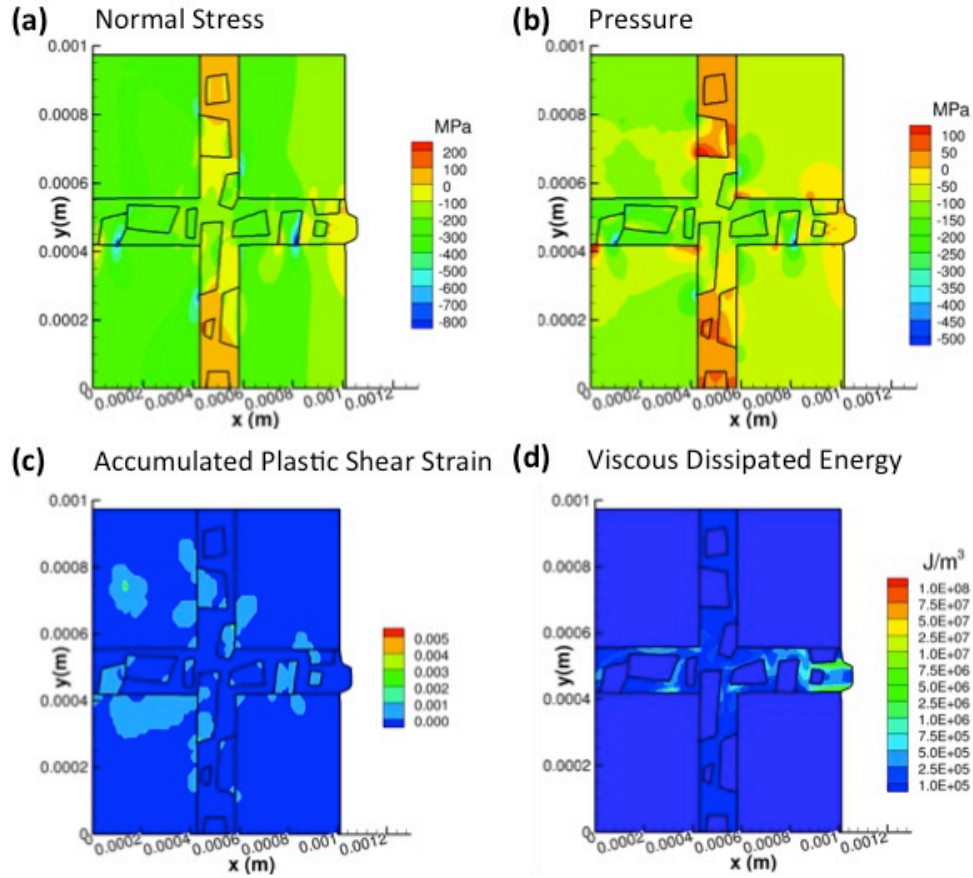


**Figure 7.8: Response of aggregate with small crystals after 2.5  $\mu\text{s}$  for dynamic compression at strain rate of  $10^{-3} \text{ s}^{-1}$ . (a) Normal stress, (b) Hydrostatic pressure, (c) Accumulated plastic shear strain, (d) viscous dissipated energy.**

The normal stress (Figure 7.8(a)) was compressive within the large crystals and horizontal binder ligaments, but the stresses were tensile in the upper and lower parts of the vertical binder ligaments. There were also high stresses (both compressive and tensile) in the small crystal corners at the crystal-crystal interface with the large grains. The hydrostatic pressures (Figure 7.8(b)) also had large gradients within the binder and at the crystal-crystal

and crystal-binder interfaces, which extended outward into the interior of the large grains. At this time, crystalline plastic shear strain (Figure 7.8(c)) began to accumulate at the crystal-crystal interfaces and corners similar to the quasi-static loading, and the energy dissipated by viscous sliding (Figure 7.8(d)) was concentrated in the horizontal binder ligaments, particularly in the thin regions between the small crystals. At this time, the binder began to protrude from the free edge, but not to the extent that was seen for the quasi-static loading.

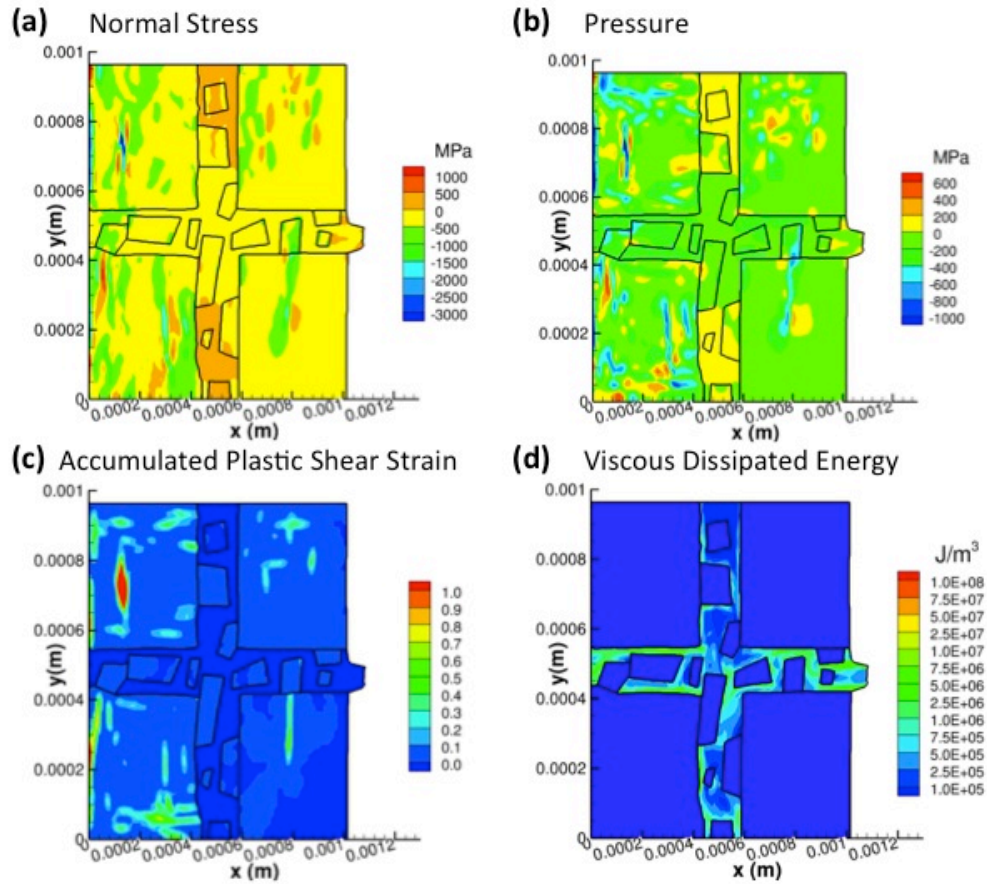


**Figure 7.9: Response of aggregate with small crystals after 3.5  $\mu\text{s}$  for dynamic compression at strain rate of  $10^3 \text{ s}^{-1}$ . (a) Normal stress, (b) Hydrostatic pressure, (c) Accumulated plastic shear strain, (d) viscous dissipated energy.**

Comparing the response at 2.5  $\mu\text{s}$  (Figure 7.8) with the response at 3.5  $\mu\text{s}$  (Figure 7.9), higher compressive stresses and pressures built up from the crystal-crystal interfaces



and corners and eventually spread into the large grain interiors. At 3.5  $\mu\text{s}$ , very high normal stresses (Figure 7.9(a)) and pressures (Figure 7.9(b)) had developed in the large grains on the left side of the aggregate at the symmetry boundary. These high stresses were accompanied by a large build-up of crystalline plastic shear strain (Figure 7.9(c)) in the large grains and viscous energy dissipation (Figure 7.9(d)) throughout the binder ligaments much more widely distributed than for the quasi-static loading. This resulted as large stress and pressure gradients between the small crystals, binder, and large grains accumulated at the interfaces and spread into the large grain interiors very quickly under the high strain rate loads.

The dynamic laser irradiation also resulted in large temperature accumulation throughout the aggregate from the various heat generation mechanisms, shown in Figure 7.10 normalized by the initial temperature of 293 K. The total temperature increase (Figure 7.10(a)) was 1.1 – 1.3 times the initial temperature throughout the upper large grains, with several localized areas with increase greater than 1.6 times the initial temperature. Temperature increases of this magnitude can trigger a runaway thermal decomposition reaction and result in hot spot formation [49,59]. In this case, the thermal decomposition mechanism (Equation 2.30) was beginning to produce significant heating at these localized sites and hot spot formation was likely. The laser-induced temperature increase (Figure 7.10(b)) was concentrated in the upper half of the aggregate, as the small crystals in the binder disrupted smooth propagation of EM waves and reduced the laser heating in the lower grains.



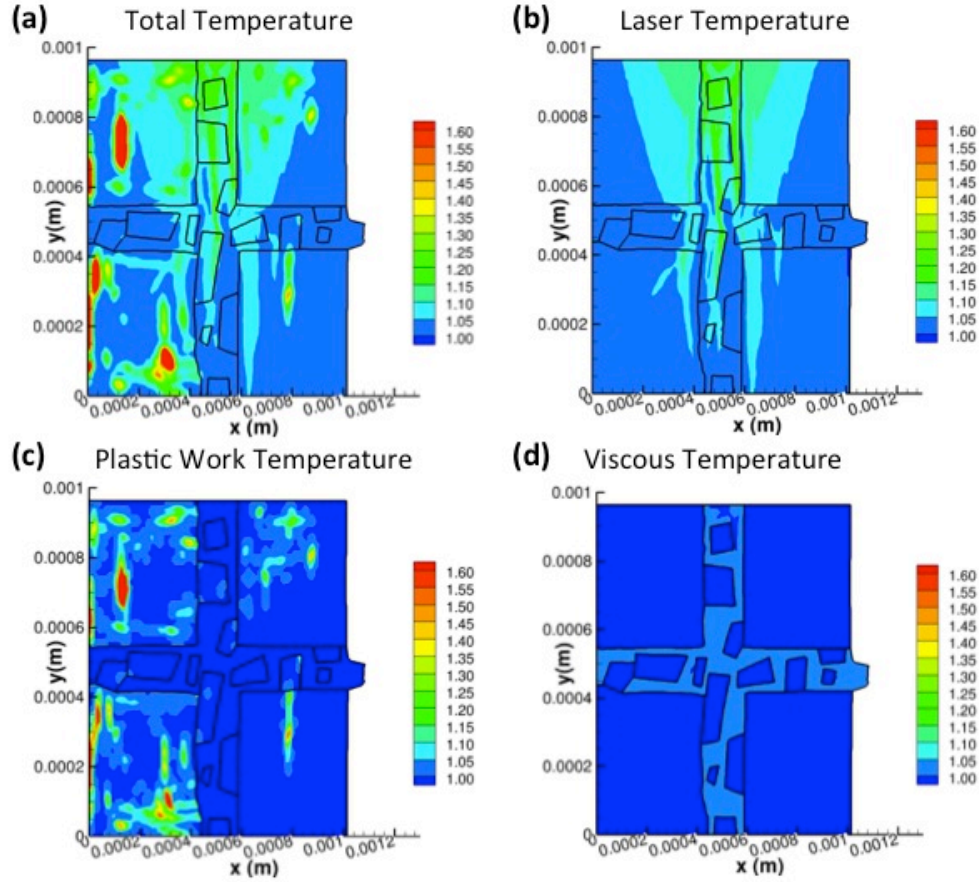


**Figure 7.10: Temperature accumulation (normalized by initial temperature of 293 K) in aggregate with small crystals after 3.5  $\mu\text{s}$  for dynamic compression at strain rate of  $10^3 \text{ s}^{-1}$ . (a) Total temperature increase, (b) Temperature increase due to laser heating, (c) Temperature increase due to plastic work, (d) Temperature increase due to viscous sliding.**

High temperature increases due to plastic work heating (Figure 7.10(c)) were localized in areas with large crystalline plastic shear strain accumulations in the large grains (Figure 7.9(c)). Viscous heating (Figure 7.10(d)) was present throughout the binder ligaments, but was very low compared to the other heat generation mechanisms. From Figure 7.10(a-d), laser heating increased the temperature significantly in the upper grains, and plastic work heating occurred in areas with high shear slip to produce localized areas with high temperature increase and activate the thermal decomposition mechanism.

### 7.2.3 High Strain Rate Coupled EM-Thermo-Mechanical Response of Aggregate Without Small Crystals in the Binder

Figure 7.11 shows the electric field normalized by the incident electric field and the laser heat generation rate for the aggregate without small crystals in the binder after 6  $\mu\text{s}$  of laser irradiation and high strain rate compression for a strain rate of  $10^{-3} \text{ s}^{-1}$ . The response of this aggregate is shown at a later time than the aggregate with crystals embedded in the binder since it took much longer for plasticity to develop in this aggregate. Most of the large crystals had an electric field magnitude between 0.4 – 0.8 times the incident electric field (Figure 7.11(a)). Electric field concentrations approximately 1.2 times the applied field were present within the vertical ligaments of the binder due to internal reflections at the crystal-binder interface. However, there was much less scattering of the EM wave when compared to the aggregate containing small crystals in the binder, and the large crystals below the horizontal binder ligaments had a much more continuous electric field distribution.

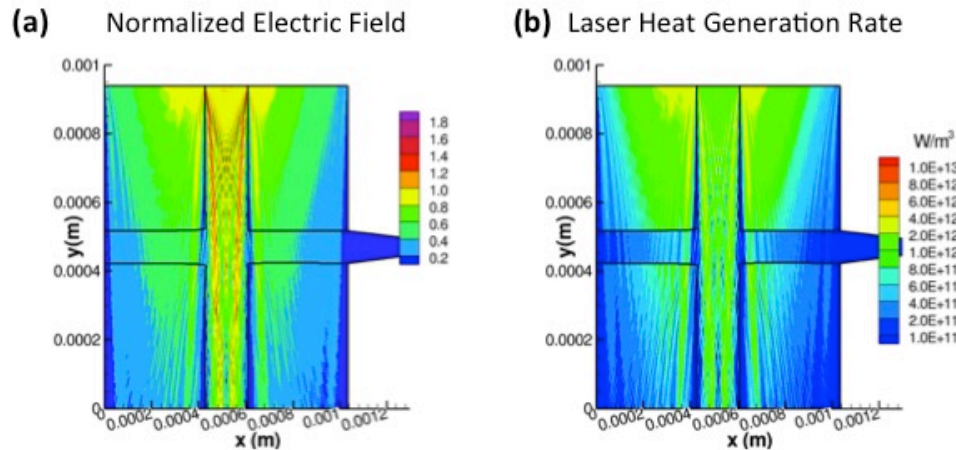


**Figure 7.11:** EM response of aggregate without small crystals after 6  $\mu\text{s}$  for dynamic compression a strain rate of  $10^3 \text{ s}^{-1}$ . (a) Electric field magnitude normalized by the applied electric field, (b) Volumetric laser heat generation rate.

The laser heat generation rate (Figure 7.11(b)) was also much more uniform than the aggregate containing small crystals in the binder, especially in the large crystals below the horizontal binder ligaments. Electric field concentrations in the vertical binder ligaments led to laser heat generation rates comparable to those present in the large grains, while the horizontal binder ligaments had lower electric fields and less laser heating.

Figure 7.12 shows the coupled response of the aggregate without small crystals in the binder to applied laser energy and high strain rate compression for a strain rate of  $10^3 \text{ s}^{-1}$  after  $6 \mu\text{s}$ .

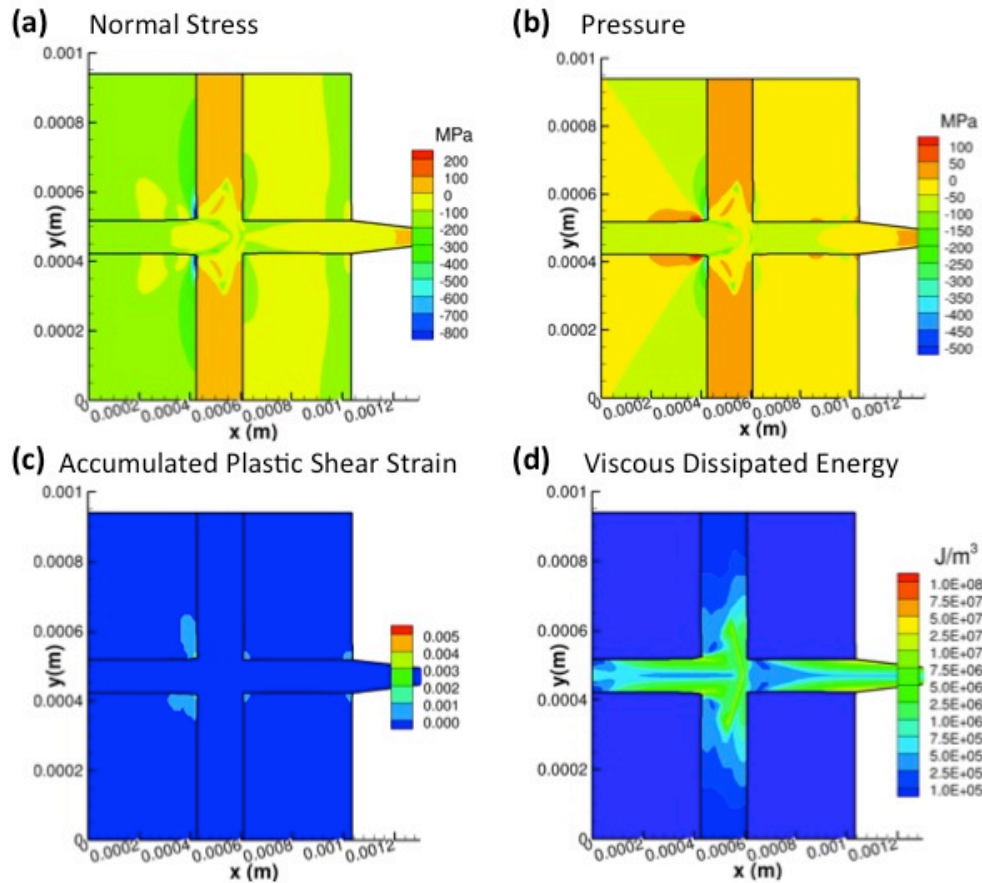


**Figure 7.12: Response of aggregate without small crystals after  $6 \mu\text{s}$  for dynamic compression at strain rate of  $10^3 \text{ s}^{-1}$ . (a) Normal stress, (b) Hydrostatic pressure, (c) Accumulated plastic shear strain, (d) viscous dissipated energy.**

The normal stresses (Figure 7.12(a)) and hydrostatic pressures (Figure 7.12(b)) were generally lower in magnitude than the aggregate with small crystals in the binder. However, high compressive stress and large pressure gradients developed at the corners of the large crystals, particularly in the two crystals constrained by the symmetry boundary. The two grains on the free surface had lower stresses.

As with the aggregate including small crystals, tensile stresses were present in the vertical binder ligaments due to the binder bulging outward at the free surface. In this case, however, the binder protruded outward substantially from between the large crystals as its sliding deformation was uninhibited. As such, viscous energy dissipation (Figure 7.12(d)) was high throughout both vertical and horizontal the binder ligaments. At this time, crystalline plastic shear strain (Figure 7.12(c)) began to accumulate in the large grain corners where high stress gradients were present. However, in comparison with the aggregate containing small grains, shear strain accumulation was delayed and began to accumulate after a longer time of  $6\mu\text{s}$ .

At a later time of  $7\mu\text{s}$ , high compressive stresses (Figure 7.13(a)) and very high stress gradients developed in the large grains on the left side of the aggregate. High pressure gradients (Figure 7.13(b)) were also present in these grains. This contributed to crystalline plastic shear strain accumulation (Figure 7.13(c)) in the large grains following a similar pattern to the case with small crystals in the binder and with much greater magnitude than at  $6\mu\text{s}$  (Figure 7.12(c)). The energy dissipated by viscous sliding (Figure 7.13(d)) increased in magnitude from its value at  $6\mu\text{s}$  (Figure 7.12(d)), and was concentrated at the junction between horizontal and vertical binder ligaments as the binder slid around the corner towards

the free edge. The large amount of binder sliding delayed the onset of high stress build up and plastic shear strain accumulation compared to the aggregate with small crystals embedded in the binder, where the embedded crystals restricted the binder's ability to slide.

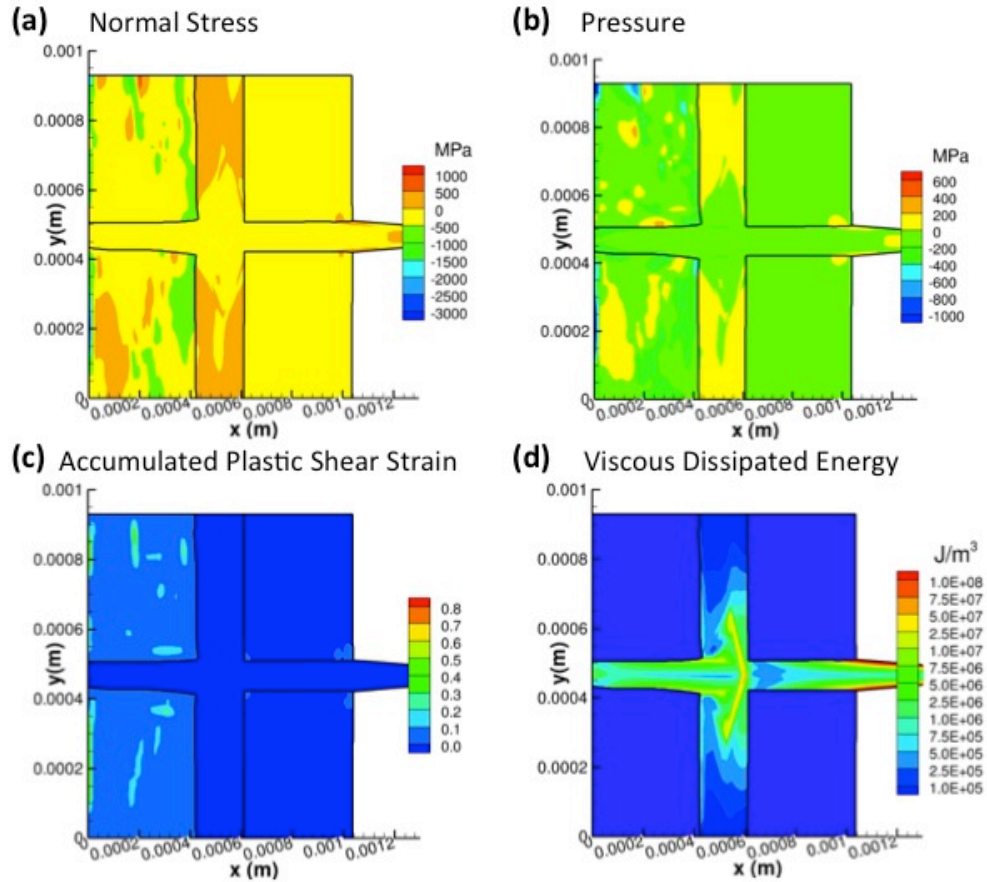


**Figure 7.13: Response of aggregate without small crystals after 7  $\mu\text{s}$  for dynamic compression at strain rate of  $10^3 \text{ s}^{-1}$ . (a) Normal stress, (b) Hydrostatic pressure, (c) Accumulated plastic shear strain, (d) Viscous dissipated energy.**

The total temperature increase (Figure 7.14(a)) was generally higher in magnitude than the case with small crystals in the binder, but there were not any localized areas with very high temperatures. The temperature increase due to laser heating (Figure 7.14(b)) followed the Gaussian spatial profile of the applied laser beam and extended into the lower grains, with much less disruption than the aggregate containing small crystals.

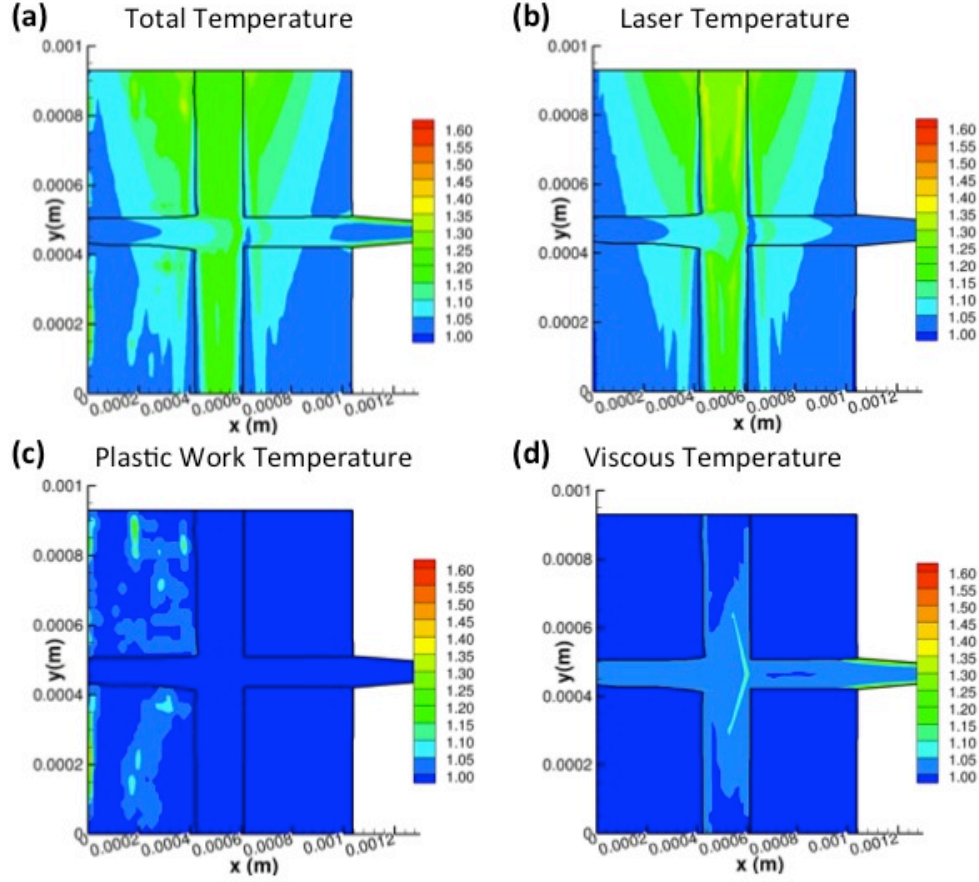


**Figure 7.14:** Temperature accumulation (normalized by initial temperature of 293 K) in aggregate without small crystals after 7  $\mu\text{s}$  for dynamic compression at strain rate of  $10^3 \text{ s}^{-1}$ . (a) Total temperature increase, (b) Temperature increase due to laser heating, (c) Temperature increase due to plastic work, (d) Temperature increase due to viscous sliding.

The laser-induced temperature increases were higher in magnitude than the aggregate with small crystals because this aggregate was exposed to the laser heating for a longer time of 7  $\mu\text{s}$  (compared to 3.5  $\mu\text{s}$ ). The temperature increase due to plastic work heating (Figure 7.14(c)) occurred in localized areas with crystalline plastic shear strain accumulation, but was lower in magnitude compared to the aggregate containing small crystals. By contrast, the temperature increase due to viscous heating (Figure 7.14(d)) was much higher than the aggregate containing small crystals due to the greater amount of sliding in the binder.



#### 7.2.4 Comparison of Global Response With and Without Small Crystals

The nominal stress-strain curves for coupled high strain rate loading and laser irradiation for both aggregates are shown in Figure 7.15. The normal stress distributions at the times discussed previously are shown as insets at the corresponding nominal strain.

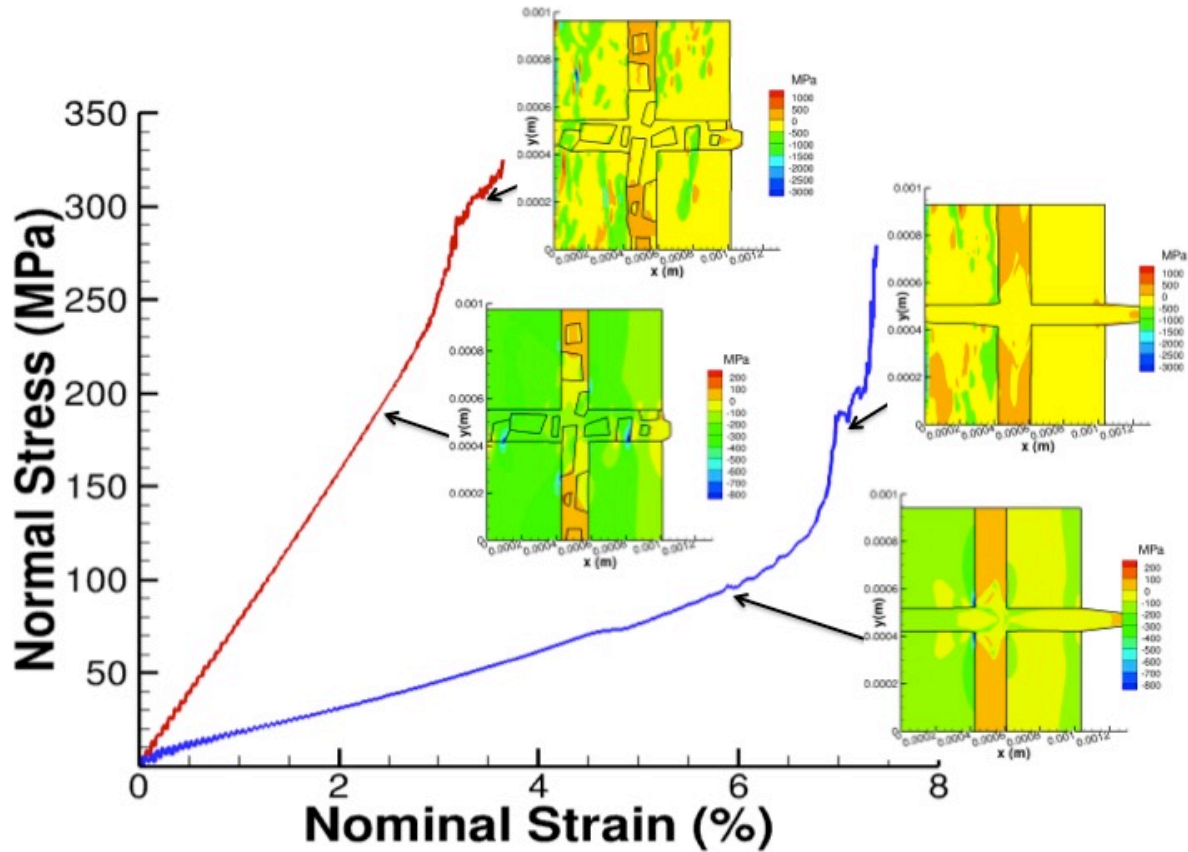


**Figure 7.15: Nominal stress-strain curves for aggregates with and without small crystalline inclusions in the binder ligaments under coupled high strain rate loading and laser irradiation.**

The aggregate containing small crystals in the binder had much higher stresses than the aggregate without small crystals. This resulted as the small crystals restricted viscous sliding deformation in the binder and resulted in high stress gradients and plasticity build-up in both large and small grains. Both aggregates reached a point where global stress began to rapidly increase as the large stress gradients built up at the interface between the large grains

and the polymer binder, which could be indicative of instability and defect nucleation. This rapid stress increase was delayed in the aggregate without small crystals, as there were fewer interfaces to initiate stress concentrations and gradients.

### **7.3 Summary**

The response of RDX-estane aggregates with various grain size distributions was investigated under both quasi-static loading and high strain rate loading coupled with laser irradiation. A non-linear finite-element formulation was used that couples laser EM wave propagation and heat generation with a dislocation-density based crystalline plasticity constitutive formulation for the RDX crystals and a finite viscoelastic constitutive formulations for the binder.

Quasi-static loading of the aggregate containing small crystals embedded in the binder ligaments produced a highly non-uniform stress state throughout the aggregate, with high normal, lateral, and shear stresses at the interfaces between small and large crystals. Crystalline plastic shear strain and statistically stored dislocation densities accumulated primarily within the small crystals and at the interfaces between small crystals, large crystals and the binder. Energy dissipated by viscous sliding in the binder was concentrated in the thin regions of binder between the embedded smaller crystals. Additionally, shear slip gradients led to geometrically necessary dislocation density accumulation at the crystal-crystal interfaces and large stress gradients at the interface regions could lead to defect nucleation.

For the aggregate containing small crystals embedded in the binder ligaments under high strain rate loading with laser irradiation, the small crystals embedded in the binder



scattered the EM wave as it passed through the binder ligaments and resulted in electric field concentrations within the vertical binder ligaments and reduction of the electric field in the large grains below the horizontal binder ligaments. High stresses and stress gradients built up at the crystal-crystal and crystal-binder interfaces, which spread into the large grains as loading continued. Crystalline plastic shear strain initiated at the crystal-crystal interfaces and developed at many locations in the large grains once large stress gradients had accumulated. Viscous sliding in the binder was an additional energy dissipation mechanism, but large deformations in the binder were restricted by the small crystals embedded within the binder ligaments. High temperatures accumulated throughout the aggregate, primarily from laser heat generation and localized adiabatic heat generation in areas with large shear slip accumulations.

For the aggregate without any small crystals embedded in the binder under high strain rate loading with laser irradiation, the electric fields produced by laser irradiation were more uniform throughout the large grains. The electric field was somewhat concentrated in the vertical binder ligaments, but there was no widespread scattering of the EM wave as seen when small crystals were present in the binder. The stresses throughout this aggregate were much lower than the aggregate with small crystals present, and the response was governed by viscous sliding in the binder and binder bulging at the free edge. Large stress gradients initiating at the crystal-binder interface eventually extended into the grain interiors and resulted in widespread crystalline shear slip accumulation, but this effect was significantly delayed when compared to the aggregate containing small crystals embedded in the binder.

Temperature increases resulted from laser heat generation mechanisms, viscous heating due to binder sliding, and adiabatic heating in localized areas with high shear slip accumulation.

For both quasi-static and high strain rate loading, the presence of embedded crystals in the binder ligaments restricted viscous binder sliding and resulted in global hardening of the aggregate, which led to large stress gradients, localized plasticity, and dislocation density accumulation. Under laser irradiation, the smaller crystals also increased scattering of the EM wave within the binder ligaments and increased the localization of EM energy and laser heat generation. High shear slip gradients at the crystal-crystal and crystal-binder interfaces led to geometrically necessary dislocation density build-up and hardening at the interface, but high stress gradients present at these interfaces can lead to instability and defect nucleation. Thus, a trade-off between strengthening and failure mechanisms at the crystal-crystal and crystal-binder interfaces was identified based on local stress gradients and geometrically necessary dislocation densities.

## SUMMARY and RECOMMENDATIONS FOR FUTURE RESEARCH

The coupled EM-thermo-mechanical response of RDX-polymer energetic aggregates under laser irradiation and high strain rate loads was investigated to characterize the coupling mechanisms between high frequency EM wave propagation, laser energy absorption, inelastic deformation, heat generation mechanisms and microstructural evolution, and to develop a fundamental understanding of the coupled response of energetic aggregates. The central findings of this work are summarized as follows:

- Localized electric field concentrations resulted as interaction with the heterogeneous aggregate microstructure caused geometrical scattering, internal reflections, and refractions of the propagating EM laser waves. These effects were enhanced by crystal-binder interfaces, crystal sizes, and defects such as voids.
- Material absorption properties, which are a function of EM wavelength, governed the penetration depth of laser energy into the aggregate and the laser heat generation rate. Dissimilar absorption properties of the RDX crystals and binder materials resulted in preferential absorption and heating. Thus, the laser heating within the aggregate can be tailored to achieve a variety of laser heat distributions, including preferential binder heating (low  $\alpha_{\text{RDX}}$ , high  $\alpha_{\text{binder}}$ ), surface heating of RDX and heating along crystal-binder interfaces (high  $\alpha_{\text{RDX}}$ , low  $\alpha_{\text{binder}}$ ), and uniform heating of the bulk aggregate (low  $\alpha_{\text{RDX}}$ , low  $\alpha_{\text{binder}}$ ).
- Localized crystalline plastic shear slip and immobile dislocation densities accumulated at void peripheries, narrow crystalline regions between two or more voids, and at the crystal-binder interfaces. High heat generation rates due to the

adiabatic plastic work heating mechanism were present in localized areas with large shear slip accumulation.

- For aggregates with estane binders, which were above the glass transition temperature during laser heating, viscous sliding in the binder was another energy dissipation mechanism that reduced stresses in aggregates with thicker binder ligaments and larger binder volume fractions.
- For aggregates with heterogeneous crystal sizes, the presence of embedded crystals in the binder ligaments restricted viscous sliding mechanisms and resulted in aggregate hardening and accumulation of geometrically necessary dislocations and high stress gradients at the interfaces between large and small crystals.
- Several hot spot formation mechanisms under laser irradiation and high strain rate loads have been identified and characterized, which are a complex function of electric field localization, laser energy absorption, crystalline shear strain localization, heat conduction, and thermal decomposition of the energetic crystals. In regions where plastic shear slip and laser heating occur simultaneously, hot spot formation is accelerated.

These predictions underscore the need to couple fundamental phenomena, such as electromagnetism and mechanical behavior for laser interactions with heterogeneous materials and provide insight to better understand applications such as laser machining, laser-induced ignition systems, and techniques for laser-based detection of energetic materials.

Based on the findings of this work, the following recommendations are made for future research on laser interaction with energetic materials:

- 1) Characterize dependence of RDX absorption coefficient on dislocation density accumulation and temperature and incorporate these relationships into the EM finite element formulation.
- 2) Develop a model for laser beam traveling through air to include effects at the material-air interface, such as reflection, plasma generation, and ablation, and to better understand laser energy transmission into the bulk material and laser-induced high strain rate loads.
- 3) Develop a formulation that accounts for thermal expansion due to confined areas of localized heating.
- 4) Expand the coupled EM-high strain rate approach to three dimensions to account for full-field EM and thermo-mechanical effects.
- 5) Develop model for dislocation density interaction at crystalline-crystalline and crystalline-amorphous interfaces and incorporate potential interface crack nucleation mechanisms.
- 6) Incorporate fracture model to investigate competition between laser-induced hot spot formation and laser-induced fracture.

## REFERENCES

- [1] Gottfried,J, Lucia,F,Jr, Munson,C, Miziolek,A, *Anal. Bioanal. Chem.* **395** (2009) 283-300.
- [2] Caygill,JS, Davis,F, Higson,SPJ, *Talanta.* **88** (2012) 14-29.
- [3] Leahy-Hoppa,M, Fitch,M, Osiander,R, *Anal. Bioanal. Chem.* **395** (2009) 247-57.
- [4] Wallin,S, Pettersson,A, Ostmark,H, Hobro,A, *Anal. Bioanal. Chem.* **395** (2009) 259-74.
- [5] Furstenberg,R, Kendziora,CA, Stepnowski,J, Stepnowski,SV, Rake,M, Papantonakis,MR, et al., *Appl.Phys.Lett.* **93** (2008) -.
- [6] Roos,EV, Benterou,JJ, Lee,RS, Roseke,F, Stuart,BC, (2002) 415-23.*Proc. SPIE 4760, High-Power Laser Ablation IV*Taos, NM.
- [7] Bourne,NK, *P. Roy. Soc. London A Mat.* **457** (2001) 1401-26.
- [8] McGrane,SD, Moore,DS, *Propell. Explos. Pyrot.* **36** (2011) 327-34.
- [9] Armstrong,RW, Elban,WL, *Mater. Sci. Tech.* **22** (2006) 381-95.
- [10] Gallagher,HG, Halfpenny,PJ, Miller,JC, Sherwood,JN, Tabor,D, *Philos. Trans. Roy. Soc. Lond. A.* **339** (1992) pp. 293-303.
- [11] Ramos,KJ, Hooks,DE, Bahr,DF, *Philos. Mag.* **89** (2009) 2381-402.
- [12] Rae,PJ, Hooks,DE, Liu,C, (2006) 293.*13th International Symposium on Detonation*Norfolk, Virginia, USA.
- [13] van der Heijden,AEDM, Bouma,RHB, *Crystal Growth & Design.* **4** (2004) 999-1007.
- [14] Barua,A, Zhou,M, *Modell. Simul. Mater. Sci. Eng.* **19** (2011) 055001.
- [15] Annapragada,SR, Sun,D, Garimella,SV, *Comp. Mater. Sci.* **40** (2007) 255-66.
- [16] Baer,MR, *Thermochimica Acta.* **384** (2002) 351-67.
- [17] Brown,EN, Rae,PJ, Orler,EB, *Polymer.* **47** (2006) 7506-18.
- [18] Cady,CM, Blumenthal,WR, Gray,GT, Idar,DJ, *Polym. Eng. Sci.* **46** (2006) 812-9.
- [19] Walley,SM, Field,JE, Greenaway,MW, *Mater. Sci. Tech.* **22** (2006) 402-13.
- [20] Bowden,FP, Yoffe,AD, *Initiation and Growth of Explosion in Liquids and Solids*, Cambridge University Press, New York 1985.

- [21] Tarver,CM, Chidester,SK, Nichols,AL, *J.Phys.Chem.* **100** (1996) 5794-9.
- [22] Borne,L, Mory,J, Schlessner,F, *Propell. Explos. Pyrot.* **33** (2008) 37-43.
- [23] Balzer,JE, Field,JE, Gifford,MJ, Proud,WG, Walley,SM, *Combust.Flame.* **130** (2002) 298-306.
- [24] Qiu,H, Stepanov,V, Di Stasio,AR, Chou,T, Lee,WY, *J.Hazard.Mater.* **185** (2011) 489-93.
- [25] Coffey,CS, In: Murray JS, Politzer P (Eds.), *Energetic Materials, Part 2: Detonation, Combustion*, 1st Edition ed., Elsevier, Boston, 2003, pp. 101-123.
- [26] Armstrong,RW, *Rev. Adv. Mater. Sci.* **19** (2009) 13-40.
- [27] Field,JE, *Acc.Chem.Res.* **25** (1992) 489-96.
- [28] Armstrong,RW, Coffey,CS, DeVost,VF, Elban,WL, *J.Appl.Phys.* **68** (1990) 979-84.
- [29] Ramaswamy,AL, Field,JE, *J.Appl.Phys.* **79** (1996) 3842-7.
- [30] Lee Perry,W, Gunderson,JA, Glover,BB, Dattelbaum,DM, *J.Appl.Phys.* **110** (2011) 034902-8.
- [31] Chen,M, You,S, Suslick,KS, Dlott,DD, *Appl.Phys.Lett.* **104** (2014) 061907-4.
- [32] Chen,M, You,S, Suslick,KS, Dlott,DD, *Rev.Sci.Instrum.* **85** (2014) 023705-8.
- [33] Zurk,LM, Orłowski,B, Winebrenner,DP, Thorsos,EI, Leahy-Hoppa,MR, Hayden,LM, *J. Opt. Soc. Am. B.* **24** (2007) 2238-43.
- [34] Abdulazeem,MS, Alhasan,AM, Abdulrahmann,S, *Int. J. Therm. Sci.* **50** (2011) 2117-21.
- [35] Khaneft,AV, Duginov,EV, *Combust. Explo. Shock Waves.* **48** (2012) 699-704.
- [36] Wood,MA, van Duin,ACT, Strachan,A, *J. Phys. Chem. A.* **118** (2014) 885-95.
- [37] Damm,D, Maiorov,M, (2010) 779502,779502-12.*Optical Technologies for Arming, Safing, Fuzing, and Firing VISan Diego, CA.*
- [38] Zikry,MA, *Comput.Struct.* **50** (1994) 337-50.
- [39] Ashmawi,WM, Zikry,MA, *J.Eng.Mater.Technol.* **124** (2002) 88-96.
- [40] Shanthraj,P, Zikry,MA, *Int.J.Plast.* **34** (2012) 154-63.
- [41] Franciosi,P, Berveiller,M, Zaoui,A, *Acta Metall. Mater.* **28** (1980) 273-83.
- [42] Devincre,B, Hoc,T, Kubin,L, *Science.* **320** (2008) 1745-8.

- [43] Shanthraj,P, Zikry,MA, *Acta Mater.* **59** (2011) 7695-702.
- [44] Kubin,L, Devincre,B, Hoc,T, *Acta Materialia.* **56** (2008) 6040-9.
- [45] Zikry,MA, Kao,M, *Scr.Mater.* **34** (1996) 1115-21.
- [46] Mas,EM, Clements,BE, Blumenthal,B, Cady,CM, Gray,GT, Liu,C, *AIP Conf.Proc.* (2002) 661-4.*AIP Conference Proceedings*Atlanta, GA.
- [47] Kaliske,M, Rothert,H, *Comput.Mech.* **19** (1997) 228-39.
- [48] Williams,ML, Landel,RF, Ferry,JD, *J.Am.Chem.Soc.* **77** (1955) 3701-7.
- [49] Cardao,PA, Gois,JC, Campos,JA, *AIP Conference Proceedings.* **505** (2000) 853-6.
- [50] Johnson,AR, Chen,T, *Comput.Methods Appl.Mech.Eng.* **194** (2005) 313-25.
- [51] Flanagan,DP, Belytschko,T, *Int J Numer Methods Eng.* **17** (1981) 679-706.
- [52] Miller,PJ, Block,S, Piermarini,GJ, *Combust.Flame.* **83** (1991) 174-84.
- [53] Czerski,H, Proud,WG, *J.Appl.Phys.* **102** (2007) 113515-8.
- [54] Kline,DE, Hansen,D, In: Slade PE, Jenkins LT (Eds.), *Techniques and Methods of Polymer Evaluation: Thermal characterization techniques*, Marcel Dekker, New York, 1970, pp. 248-292.
- [55] Baytos,JF, *Los Alamos Scientific Laboratory, Informal Report.* **LA-8034-MS** (1979).
- [56] Hummel,RE, *Electronic Properties of Materials*, 4th Edition ed., Springer, New York, 2011, pp. 215-226.
- [57] Isbell,RA, Brewster,MQ, *Propell. Explos. Pyrot.* **23** (1998) 218-24.
- [58] Bruckman Jr.,HJ, Guillet,JE, *Can. J. Chemistry.* **46** (1968) 3221-8.
- [59] LaBarbera,DA, Zikry,MA, *J.Appl.Phys.* **113** (2013) 243502-14.
- [60] Clayton,JD, Becker,R, *J.Appl.Phys.* **111** (2012) 063512-9.
- [61] Burnham,AK, Weese,RK, *Thermochimica Acta.* **426** (2005) 85-92.
- [62] Funk,DJ, Calgaro,F, Averitt,RD, Asaki,MLT, Taylor,AJ, *Appl.Spectrosc.* **58** (2004) 428-31.
- [63] Yeager,JD, Dubey,M, Wolverson,MJ, Jablin,MS, Majewski,J, Bahr,DF, et al., *Polymer.* **52** (2011) 3762-8.



- [64] Donohue,A, Spaepen,F, Hoagland,RG, Misra,A, *Appl.Phys.Lett.* **91** (2007) 241905-3.
- [65] Wang,Y, Li,J, Hamza,AV, Barbee,TW, *Proc. Natl. Acad. Sci.* **104** (2007) 11155-60.
- [66] Tan,H, Huang,Y, Liu,C, Geubelle,PH, *Int.J.Plast.* **21** (2005) 1890-918.
- [67] Elkhodary,KI, Zikry,MA, *J.Mech.Phys.Solids.* **59** (2011) 2007-22.
- [68] Rezvanian,O, Zikry,MA, Rajendran,AM, *Proceedings of the Royal Society of London A: Mathematical, Physical and Engineering Sciences.* **463** (2007) 2833-53.
- [69] Ashby,MF, *Philosophical Magazine.* **21** (1970) 399-424.